Experiments and simulations of the spectral phase of few-cycle fs-laser pulses during supercontinuum generation in a neon gas filled hollow core fiber

Doctoral Dissertation

Peter Bartz

Lehrstuhl für Molekül- und Oberflächenphysik
Fakultät für Physik
Universität Bielefeld

supervised by

Prof. Dr. DrSc. h.c. U. Heinzmann

Prof. Dr. W. Pfeiffer

March 2014

Contents

Introduction

Modern physics is making fast progress in measuring always smaller systems and always faster dynamics. Today it is possible to breach into the realm of single atoms and the dynamics of solid state electron transitions are probed with a resolution in the atomic scale. The time regime for electron movement in bound valence states or in free electron gases with a comparable length scale is in the region of 100 as [1, p. 165]. To investigate and eventually be able to control electron dynamics on that time scale pulses of light have been made shorter and shorter in the course of the last decades. The duration of a pulse of light, however, is related to the frequency bandwidth of its spectrum. Similar to the uncertainty between time and energy a pulse of light which is severely limited in time has by necessity a broad spread in energy.

Light with a very broad frequency bandwidth is sometimes referred to as white light, since it encompasses many 'colors' of light. When a narrow-band input pulse undergoes extreme nonlinear spectral broadening to yield a broadband spectrally continuous output, this spectrum is referred to as a supercontinuum [2, p. 1136]. A supercontinuum can spread over more than an octave bandwidth and hence has the potential to support a very short pulse of light. Another application of such a broad spectrum is the measurement and stabilization of a frequency comb, which can be used for absolute optical frequency measurements or the stabilization of the carrier-envelope phase [3].

Historically, the first supercontinuum was generated by Alfano and Shapiro in 1970 [4] after the effect was discovered in the laboratory by accident. Laser pulses at a wavelength of 530 nm, a pulse duration of about 6 ps and an energy of 5 mJ per pulse were sent through bulk glass and liquid samples to create filaments with a supercontinuum ranging from 2.7 to 4.7 PHz angular frequency, or 400 to 700 nm wavelength. In 1976 Lin and Stolen [5] presented fiber waveguides as a new and superior method to generate supercontinua. The advantage of the fiber waveguide is that the interaction length between the laser pulse and the nonlinear medium is greatly increased in comparison to a bulk medium, where the interaction length is limited by the length of the laser focus. Anomalous dispersion in fused silica for wavelengths longer than 1.3 µm led 1980 to the field of soliton generation, in which the cancellation of nonlinear and dispersive effects causes a pulse of light to propagate through a fiber without any further change in pulse shape [6]. Conventional optical fibers are made from solid dielectric material, usually fused silica. In 1996 photonic crystal fibers were introduced by Knight *et al.* [7], in which the refractive index in the

fiber is determined by an array of air holes surrounding the solid core. It is possible to finely control the properties of the fiber this way and a large supercontinuum community has evolved around the use of photonic crystal fibers [2].

However, due to the use of solid material the amount of laser power which can be transported in a conventional optical fiber or a photonic crystal fiber without the fiber being damaged is limited. Hollow-core fibers filled with a noble gas have higher attenuation losses than solid fibers, since the beam is not guided by total internal reflection anymore but rather by reflections under grazing incidence, but are capable of transporting high power light beams. High laser pulse powers are important for nonlinear applications, and in 1996 Nisoli *et al.* [8] adapted a gas-filled hollow-core fiber for supercontinuum generation and improved the method to create ultra short laser pulses with multigigawatt peak powers [9].

Such ultrashort high power laser pulses are required to achieve pulse durations in the attosecond regime and study the dynamics of electrons in an atomic scale, and Hentschel *et al.* isolated a single light pulse of attosecond duration from high harmonic radiation in 2001 [10]. In 2004 Kienberger *et al.* demonstrated the use of such pulses in streaking measurements to resolve atomic electron dynamics in gases at an attosecond time scale [11]. In 2007 this method was adapted in a groundbreaking experiment to measure the electron dynamics of single-crystalline tungsten by Cavalieri *et al.* [12], or more recently in similar investigations of single-crystalline magnesium [13].

This thesis concerns itself with the optimization of the supercontinuum generated by means of a gas-filled hollow-core fiber for the purpose of attosecond metrology in experiments which are very similar in their setup to the experiment of Cavalieri *et al.* [12]. The main objective of the optimization of the supercontinuum in this regard is the generation of laser pulses which have as short a duration as possible.

The introduction of the review paper of Zheltikov [14] from 2002 gives a good overview over the field of hollow-core fiber generated supercontinua. Since then there have been publications about innovative ways to improve the general setup for the employment of gas-filled hollow-core fibers, like utilization of a gas gradient in the fiber pressure chamber instead of a constant pressure [15], or a cascading arrangement of two hollow-core fibers in sequence [16]. However, there has been scarce investigation of the impact of the input laser pulses' properties, beyond energy per pulse and pulse duration, on the resulting supercontinuum.

In this work numerical simulations are used to investigate how the supercontinuum generated in the gas-filled hollow-core fiber is affected by the spectral phase of the laser pulses in front of the fiber. This is supported by measurements of the spectral phase with a SPIDER (**S**pectral **P**hase **I**nterferometry for **D**irect **E**lectric-field **R**econstruction) from *Venteon*, which is able to retrieve the spectral phase both in front and after the hollow-core fiber. It is found that the spectral phase of the pulses

in front of the fiber does indeed have a vast impact on the form and bandwidth of the resulting supercontinuum, and not only insofar that it determines the input pulses' duration and power. Because of that, control of the spectral phase of the input laser pulses opens up the possibility to optimize and tailor the supercontinuum in regard to specific properties and applications, and this is applied to optimize the pulse duration after compression behind the hollow-core fiber in simulations.

This thesis is organized as follows. In chapter 1 the concepts necessary to describe ultra short laser pulses are introduced and the groundwork for the numerical calculations is laid in form of the 1-dimensional pulse propagation equation. In chapter 2 the experimental setup is described and the model for the numerical calculations by means of the split-step method explained. In chapter 3 measurements of the supercontinuum and the pulses' spectral amplitude and phase in dependence on the gas pressure inside the hollow-core fiber are presented and discussed, and shown to be in qualitative agreement with the results of the numerical calculations. In chapter 4 the effect of the input pulses' spectral phase on the supercontinuum after the hollow-core fiber is investigated by means of numerical calculations, and the simulation is used to optimize the supercontinuum in regard to pulse duration. In chapter 5 a brief summary of the results presented in this thesis is delivered.

1. Theoretical Background

In this chapter the background for the rest of this work and especially the numerical calculations is laid out. Section 1.1 starts with the representation of short pulses of light. In section 1.2 the optical Kerr effect and its consequences on the refractive index are explained, which are the source of the nonlinear process studied throughout this work. In section 1.3 the pulse propagation equation (PPE) is derived from the Maxwell equations. The PPE describes what is happening to a pulse of light during propagation in a medium, including dispersion in that medium and nonlinear effects like the generation of new frequencies due to self-phase modulation (SPM) and self-steepening. It is the base of the numerical simulation presented in section 2.2. In section 1.4 SPM is discussed in more detail. In section 1.5 time-frequency representations are introduced as a tool for pulse analysis.

1.1. Representation of light pulses

In this section a by necessity brief introduction of concepts useful for the representation and description of short pulses of light is given. For a more detailed treatment the work of Wollenhaupt *et al.* [17, p. 1047-1069] is pointed out as a reference.

1.1.1. Representation in time and frequency domain

A pulse of light is represented by its electric field vector $\mathbf{E}(\mathbf{r}, t)$. Throughout this work only linearly polarized fields which maintain the direction of their polarization are considered, and hence the field vector can be treated as a scalar $E(\mathbf{r}, t)$. In this section it is also assumed for simplicity's sake that the pulse is stationary or rather that it is observed by a stationary detector, and as such the spatial components are ignored and the electric field is reduced to $E(t)$.

The electric field $E(t)$ of a wave can be separated into an amplitude function $A(t)$, which would be a constant in case of a monochromatic wave instead of a pulse of light, and a wave oscillation term with a phase $\phi(t)$ such that [17, p. 1048]

$$E(t) = A(t) \cos \phi(t). \tag{1.1}$$

The temporal phase $\phi(t)$ can be separated into different parts as [17, p. 1049]

$$\phi(t) = \phi_0 + \omega_0 t + \phi_a(t), \tag{1.2}$$

where the first term is a constant phase offset, the second term is linear in t with ω_0 being the carrier frequency, and the third term includes any remaining higher orders of t.

Eq. (1.2) can be treated as an expansion of $\phi(t)$ around $t_0 = 0$ in a Taylor series, and as such ω_0 is ${}^{\partial\phi(t)}/_{\partial t}\big|_{t_0}$. As will be discussed later the carrier frequency ω_0 is more commonly defined as [18, p. 6]

$$\omega_0 = \frac{\int_0^\infty |\tilde{E}(\omega)|^2 \omega \, \mathrm{d}\omega}{\int_0^\infty |\tilde{E}(\omega)|^2 \, \mathrm{d}\omega}, \tag{1.3}$$

where $\tilde{E}(\omega)$ is the complex field amplitude in dependency on the angular frequency ω. Here and throughout this work complex-valued quantities are denoted with a tilde. From now on the term angular will be dropped and frequency will refer to both the frequency $f = {}^1/_T$, with T being the period of an oscillation, and the angular frequency $\omega = 2\pi f$.

It is often very useful to represent the electric field $E(t)$ in the frequency domain as $\tilde{E}(\omega)$. Since time and frequency are a Fourier transform pair it is possible to do so with a Fourier transformation, and $E(t)$ can accordingly be expressed with an inverse Fourier transformation of $\tilde{E}(\omega)$ such that [17, p. 1049]

$$\begin{aligned} \tilde{E}(\omega) &= \mathcal{F}E(t) = \int_\infty E(t) e^{-i\omega t} \, \mathrm{d}t \\ E(t) &= \mathcal{F}^{-1}\tilde{E}(\omega) = \frac{1}{2\pi} \int_\infty \tilde{E}(\omega) e^{i\omega t} \, \mathrm{d}\omega. \end{aligned} \tag{1.4}$$

Because $E(t)$ as a physical observable is a real valued function $\tilde{E}(\omega) = \tilde{E}^*(-\omega)$ holds, where * denotes the conjugate-complex of the respective quantity. It follows that for a light field without DC component, meaning without a component at $\omega = 0$, it is sufficient to know $\tilde{E}(\omega)$ for positive frequencies to fully characterize the electric field [17, p. 1049]. An $\tilde{E}^+(\omega)$ can be defined, which is equal to $\tilde{E}(\omega)$ for $\omega > 0$ and equal to zero otherwise. The inverse Fourier-transform of $\tilde{E}^+(\omega)$ is the complex valued $\tilde{E}^+(t)$. This is used to avoid the treatment of negative frequencies where it is not necessary, and to allow for a complex representation of $E(t)$.

In the same way an $\tilde{E}^-(\omega)$ and $\tilde{E}^-(t)$ can be defined and it is obtained that [17, p. 1050]

$$\begin{aligned} \tilde{E}(\omega) &= \tilde{E}^+(\omega) + \tilde{E}^-(\omega) \\ E(t) &= \tilde{E}^+(t) + \tilde{E}^-(t) = 2\,\mathrm{Re}\{\tilde{E}^+(t)\}. \end{aligned} \tag{1.5}$$

1.1.2. The envelope function and the phase term

A pulse of light can be represented in a so called envelope function in conjunction with a phase term not unlike Eq. (1.1). This is a method to reduce the fast oscillating

electric field to a slower varying envelope function, which is generally easier to handle in calculations than the electric field itself.

Since $\tilde{E}^+(t)$ is complex valued it can be expressed as a product of a real amplitude function and a phase term such that

$$\tilde{E}^+(t) = |\tilde{E}^+(t)|e^{i\phi(t)} = \frac{1}{2}A(t)e^{i\phi(t)}, \tag{1.6}$$

where the factor 1/2 is chosen to make $A(t)$ conform with Eq. (1.1) and (1.5). Using Eq. (1.2), it is also possible to define a complex amplitude or envelope function $\tilde{A}(t)$ by separating the temporal phase $\phi(t)$ and including some of its terms in the envelope such that

$$\tilde{E}^+(t) = \frac{1}{2}\tilde{A}(t)e^{i\omega_0 t}. \tag{1.7}$$

In this representation the light pulse is separated into a fast carrier wave and an envelope function. This is especially useful if the envelope $\tilde{A}$ is varying only slowly in comparison to the carrier frequency ω_0, but Eq. (1.7) for itself does not impose any restrictions in that regard. The designation of the carrier frequency is not unique and it is chosen in such a way that the envelope function is as smooth as possible, usually by calculating ω_0 as in Eq. (1.3) [18, p. 6].

In analogy to $\tilde{E}^+(t)$ it is also possible to separate $\tilde{E}^+(\omega)$ into an envelope function and a phase term, and one obtains

$$\tilde{E}^+(\omega) = |\tilde{E}(\omega)^+|e^{-i\phi(\omega)} = \tilde{A}(\omega)e^{-i\omega_0 t}, \tag{1.8}$$

where $\phi(\omega)$ is the spectral phase. It can be expanded in a Taylor series around the carrier frequency ω_0 and is written as [17, p. 1052]

$$\begin{aligned}\phi(\omega) &= \sum_{j=0}^{\infty} \frac{1}{j!}\phi_j(\omega-\omega_0)^j \\ &= \phi_0 + \phi_1(\omega-\omega_0) + \frac{1}{2}\phi_2(\omega-\omega_0)^2 + \frac{1}{6}\phi_3(\omega-\omega_0)^3 + ...,\end{aligned} \tag{1.9}$$

where the ϕ_j are derivatives with respect to ω, with

$$\phi_j = \left.\frac{\partial^j \phi(\omega)}{\partial \omega^j}\right|_{\omega_0}. \tag{1.10}$$

The first term on the right-hand side of Eq. (1.9) describes the absolute phase or the carrier-envelope phase (CEP) in the time domain. That is the offset between the maximum of the envelope function and the nearest maximum of the carrier wave. A pulse with a CEP equal to zero has no offset between carrier and envelope and is often referred to as cosine pulse, while a pulse with maximal offset is called a sine pulse [17, p. 1048].

The ϕ_1 coefficient causes a temporal shift of the pulse in the time domain without changing the actual pulse shape. A positive ϕ_1 corresponds to a shift towards later times. In the absence of higher terms ϕ_j, $\phi_1 = {}^{\partial\phi}/_{\partial\omega}\big|_{\omega_0}$ is identical to the group delay $T_g(\omega)$, which is defined as $T_g(\omega) = {}^{\partial\phi}/_{\partial\omega}$ and describes the relative temporal delay of a given spectral component [17, p. 1051].

The ϕ_2 coefficient is called group delay dispersion (GDD) in a medium [17, p. 1058] and causes the pulse to be chirped, meaning the different frequencies are not uniformly distributed over the pulse in the time domain anymore. The sign in Eq. (1.8) is chosen so that a positive ϕ_2 corresponds to a linearly up-chirped laser pulse, meaning the high frequencies will be at the tail-end of the pulse in the time domain. This term broadens the pulse shape in the time domain symmetrically and has a strong impact on pulse duration.

The ϕ_3 coefficient is called third order dispersion (TOD) in a medium [17, p. 1058] and causes a nonlinear chirp and an asymmetrical deformation of the pulse shape, changing the gradient of the slopes and giving rise to prepulses for negative TOD or after-pulses in the case of positive TOD.

In Fig 1.4 on page 28 different laser pulses with exemplary phases are illustrated, including spectral amplitude, spectral phase, group delay, pulse shape and temporal phase. In the work of Wollenhaupt *at al.* [17, p. 1051-1053] further examples for the visualization of the effects of the spectral phase are provided.

When the temporal phase is presented in figures throughout this work, only the nonlinear part $\phi_a(t)$ of Eq. (1.2) is shown. This is done because the linear terms of $\phi(t)$ only contain information about the CEP offset and the choice of carrier frequency. Pulse properties like the chirp of the pulse are part of the nonlinear coefficient $\phi_a(t)$, and because of that it is presented without perturbance through the linear phase terms.

A short light pulse propagating in a linear medium experiences changes in both amplitude and phase, which are expressed in the complex optical transfer function $\tilde{M}(\omega)$. If the input electric field is $\tilde{E}_{\text{in}}(\omega)$, one obtains for the output field after the medium [17, p. 1057]

$$\tilde{E}_{\text{out}}(\omega) = \tilde{M}(\omega)\,\tilde{E}_{\text{in}}(\omega) = R(\omega)e^{-i\phi_d(\omega)}\tilde{E}_{\text{in}}(\omega), \tag{1.11}$$

where $R(\omega)$ is the real valued spectral amplitude response, which includes absorption effects, and $\phi_d(\omega)$ is the spectral phase transfer function. During propagation in a medium a light pulse accumulates the spectral phase transfer function [17, p. 1058]

$$\phi_d(\omega) = n(\omega)k(\omega)z, \tag{1.12}$$

where n is the refractive index of the medium, $k = {}^{\omega}/_{c}$ is the vacuum wavenumber, c is the vacuum speed of light, and z is the propagation distance. The spectral phase transfer function is expanded in a Taylor series like the spectral phase in Eq. (1.9),

and if $n(\omega)$ of the medium is known, the coefficients ϕ_{d_j} can be calculated with Eq. (1.10).

Here $n(\omega)$ is real valued in accord to the cited reference. In section 1.2.2 the refractive index n is treated as complex valued and includes absorption effects. In that case $\phi_d(\omega)$ also becomes complex and the real valued spectral amplitude response $R(\omega)$ can be dispensed with.

In the spectral region considered in this work all materials have a spectral phase transfer function with positive coefficients for GDD and TOD. A material commonly used in optics due to its low dispersion is fused silica, whereas a material like Schott SF-10 glass is chosen when a high dispersion is desired. In the table below the GDD and TOD of materials and gases employed in our beamline are listed. The values for the gases are given for room temperature and a pressure of 1 bar. For higher pressures, like $p = 3\,\text{bar}$ for neon in the hollow-core fiber, the value is multiplied with $^{p}/_{1\,\text{bar}}$ as explained in section 1.2.2. The values for Schott SF-10 glass are taken from [17, p. 1056], and for air from [19]. The other materials are calculated from the refraction index $n(\lambda)$ gained from the Sellmayer equation, which is taken from [20] for fused silica and [21] for neon. The dependence on the wavelength for the dispersion coefficients of neon gas is shown in the left-hand side of Fig. 2.4 on page 41.

material	GDD [fs^2/mm]	TOD [fs^3/mm]
Fused Silica	36.1	27.4
Schott SF-10	143.4	97.3
Neon gas	0.0026	0.0012
Air	0.02	0.012

1.1.3. Pulse duration

The pulse duration τ is an important property for an ultra short pulse which consists of only few optical cycles. It is common practice in ultrashort optics [18, p. 9] to calculate the pulse duration τ as the full width at half maximum (FWHM) of the temporal envelope $|E(t)|^2$. This approach is justified since the pulses examined nearly always consist of a single main peak and any side peaks are of negligible intensity. For nonlinear applications in particular it is mainly the peak with the highest intensity which is of interest for the experiment.

However, in cases where the pulse shape notably deviates from a single peak form, like for the asymmetric side peaks generated by large amounts of third order dispersion (TOD), the FWHM pulse duration τ is not meaningful anymore as a description of the pulse. Instead the statistical definition of a width in time t as standard deviation can be used as a measure of the pulse duration [17, p. 1055-1056]. The standard deviation or mean square deviation σ of a variable x is defined as

$$\sigma = \langle \Delta x \rangle = \sqrt{\langle (x - \langle x \rangle)^2 \rangle} = \sqrt{\langle x^2 \rangle - \langle x \rangle^2}, \tag{1.13}$$

with $\langle x \rangle$ being the expected value of the variable x. In the time domain one obtains [18, p. 16]

$$\langle \Delta t \rangle = \sqrt{\frac{1}{W} \int_{\infty} t^2 P(t) dt - \frac{1}{W^2} \left(\int_{\infty} t P(t) dt \right)^2}, \tag{1.14}$$

with W being the energy per pulse and $P(t)$ the instantaneous power. The standard deviation $\langle \Delta t \rangle$ is only a half width, and similar to the FWHM pulse duration τ a pulse duration τ_σ can be defined as $\tau_\sigma = 2\sigma$. For a Gaussian pulse with $G(t) = \exp\left(-\frac{1}{2}\frac{t^2}{\sigma^2}\right)$ one obtains

$$\tau_\sigma = 2\langle \Delta t \rangle = \frac{1}{\sqrt{2\ln 2}} \tau \simeq 0.85\,\tau, \tag{1.15}$$

where τ is the FWHM pulse duration. For a pulse with a single Gaussian peak τ_σ is smaller than τ. For a pulse with side peaks τ_σ increases very fast though and is usually larger than τ, until the FWHM-based τ loses any significance once a second peak grows so high that it reaches half of the height of the main peak.

Most works about ultra short pulse phenomena are treating light pulses with negligible side peaks though, which makes consideration of the time standard deviation unnecessary, and hence the FWHM pulse duration τ is used by default. Furthermore, for nonlinear applications like high harmonic generation only peaks of high intensity are of importance, providing another reason to ignore low intensity side peaks. Because of this the FWHM duration τ is used in all discussions of the pulse duration in this thesis. However, in section 4.3.2 laser pulses with very high amounts of TOD are investigated, and in those cases τ_σ is considered in comparison.

Since time t and frequency ω are Fourier transforms of one another, it is obvious that a pulse cannot be sharply localized in both domains at once. Similar to the uncertainty principle a time-bandwidth product can be retrieved, which for Gaussian pulse shapes can be written as [18, p. 17]

$$\langle \Delta t \rangle \langle \Delta \omega \rangle = \frac{1}{2}, \tag{1.16}$$

or in FWHM designation [17, p. 1053]

$$\tau \Delta \omega = 4 \ln 2. \tag{1.17}$$

Here τ and $\Delta\omega$ are the FWHM widths of the pulse in the time and frequency domains respectively, while $\langle \Delta t \rangle$ and $\langle \Delta \omega \rangle$ are the corresponding standard deviations. For non-Gaussian pulse forms the time-bandwidth product assumes slightly different values [18, p. 10].

The equality in Eq. (1.16) and (1.17) only holds for pulses which are Gaussian in both domains, or which have only a linear spectral phase $\phi(\omega)$. As soon as a nonlinear spectral phase is present, the equality has to be replaced with a greater-than sign.

It follows that for a given spectrum a pulse has the shortest possible duration in the time domain if it has a nonlinear spectral phase equal to zero. This is defined as the bandwidth-limited or Fourier-transform limited (FTL) duration τ_0. For a Gaussian spectrum τ_0 can be determined with Eq. (1.17), but otherwise it has to be calculated by Fourier-transforming the spectral amplitude and determining the FWHM width of the result in the t domain.

1.2. The nonlinear refractive index

In the previous section pulse propagation in a linear medium has been addressed. When the intensity of the propagating light pulse is high enough, nonlinear effects start to play a role and change the value of the refractive index of the medium. The optical Kerr effect is such a nonlinear process and scales with the cubic of the electric field. It is the source of self-phase modulation and the generation of new frequencies in a light pulse propagating through a hollow-core fiber filled with a rare gas. While there are also nonlinear effects scaling with the square of the electric field instead of the cubic, these do not occur in a medium with an inversion symmetry at the molecular level [22, p. 14] like a rare gas.

The optical Kerr effect is presented in section 1.2.1, and in section 1.2.2 the consequences of the nonlinear refractive index in regard to some properties of the medium are discussed.

1.2.1. The optical Kerr effect

The Kerr effect in general is a change in the refractive index of a material in response to an applied electric field. This applies both to direct (DC) and alternating currents (AC). The optical Kerr effect in particular handles the electric fields of light and is hence an AC effect.

The interaction of light with a medium is governed by the medium's polarization $\mathbf{P}$. As in section 1.1 it is assumed that the light is linearly polarized and maintains its polarization direction during propagation, which allows to treat the vector $\mathbf{P}$ as a scalar P.

If the nonlinearity is small enough to be handled as a perturbation of the linear process, P is defined as [18, p. 167]

$$\begin{aligned} P = \epsilon_0 \chi E &= \epsilon_0 \left(\chi^{(1)} E + \chi^{(2)} E^2 + \chi^{(3)} E^3 + ... \right) \\ &= P^{(1)} + P^{(2)} + P^{(3)} + ... \end{aligned} \tag{1.18}$$

where E is the electric field, ϵ_0 is the vacuum permittivity, and χ is the electric susceptibility of the medium which consists of a linear part $\chi^{(1)}$ and higher nonlinear terms, with

$$\chi = \chi^{(1)} + (\chi^{(2)} E + \chi^{(3)} E^2 + ...). \tag{1.19}$$

Here the coefficients $\chi^{(j)}$ are scalars, but if E and P are vector quantities the coefficients $\chi^{(j)}$ are generally tensors.

Eq. (1.18) holds both in the time and in the frequency domain. However, in the frequency domain E, P and χ have complex values.

In Eq. (1.18) it is also assumed that the polarization acts nearly instantaneously with changes of the field. In general, both electrons and nuclei respond to the electric field, with the nuclei response being inherently slower than the electronic response. The assumption of a nearly instantaneous response amounts to neglecting the contribution of molecular vibrations [22, p. 32]. However, this work concerns itself with noble gases as interaction medium and hence does not need to consider molecular vibrations.

Any $P^{(j)}$ with an even j can be neglected in a noble gas medium due to symmetry considerations [22, p. 14]. The terms with $j \geq 5$ can also be neglected at the pulse powers $P < 20\,\mathrm{GW}$ employed in this work. A recent study in argon demonstrates that even for a pulse power sufficient to cause filamentation, equivalent to roughly five times the pulse power used in our experiments, the inclusion of higher order nonlinearities only has notable consequences for input pulses with a central wavelength of 400 nm or less [23]. For input pulses with a central wavelength of 800 nm, as they are used in the scope of this work, nearly no influence of high order ($j \geq 5$) nonlinearities was observed even at high laser powers.

With all even order and higher order terms of the nonlinear polarization dropped, P is reduced to $P = P^{(1)} + P^{(3)}$.

In the case of a single input pulse with a linear polarized electric field, which can be expressed with a complex envelope $\tilde{A}(t)$ and a carrier wave as in Eq. (1.7)), $E(t)^3$ can be written as

$$\begin{aligned} E(t)^3 &= \left(\tilde{A}(t)e^{i\omega_0 t} + \tilde{A}^*(t)e^{-i\omega_0 t}\right)^3 \\ &= \tilde{A}(t)^3 e^{i3\omega_0 t} + 3|\tilde{A}(t)|^2\tilde{A}(t)e^{i\omega_0 t} + \text{c.c.}, \end{aligned} \tag{1.20}$$

where c.c. denotes the conjugate-complex of the previous terms. Accordingly $P^{(3)} = \chi^{(3)}E^3$ can be separated into two terms oscillating with different frequencies. One term has a frequency of $\omega = 3\omega_0$ and represents third harmonic generation. This term is dropped since it requires phase matching [22, p. 32]. What is left is the part oscillating with ω_0, which corresponds to $3/4$ of the original $P^{(3)}$.

From this it is obtained that

$$P^{(3)} = \epsilon_0 \chi^{(\mathrm{nl})} E \tag{1.21}$$

$$\chi^{(\mathrm{nl})} = \frac{3}{4}\chi^{(3)}|\tilde{A}(t)|^2, \tag{1.22}$$

with $\chi^{(\mathrm{nl})}$ being the sole remaining nonlinear part of the electric susceptibility χ.

The refractive index n of a medium can be derived from the electric susceptibility χ as [24, p. 6]

$$n^2 = 1 + \chi. \tag{1.23}$$

Since χ has a nonlinear component $\chi^{(\mathrm{nl})}$, it follows that the refractive index also acquires a nonlinear component, which is denoted as n_2. With the approximations made above it follows from Eq. (1.18) to (1.23) that

$$\begin{aligned} n &= \sqrt{1+\chi} \\ &= \sqrt{1+\chi^{(1)}+\chi^{(\mathrm{nl})}} \\ &= \sqrt{n_0^2\left(1+\frac{\chi^{(\mathrm{nl})}}{n_0^2}\right)} \\ &= n_0\left(1+\frac{\chi^{(\mathrm{nl})}}{2n_0^2}\right) \\ &= n_0 + \frac{3\chi^{(3)}}{8n_0}|\tilde{A}(t)|^2 \\ &= n_0 + \hat{n}_2|\tilde{A}(t)|^2 \\ &= n_0 + n_2 I(t) \end{aligned} \tag{1.24}$$

The linear refractive index is defined as $n_0 = \sqrt{1+\chi^{(1)}}$, and because $\chi^{(3)}$ is small in comparison to $\chi^{(1)}$, the approximation $\sqrt{1+x} \simeq (1 + x/2)$ is used. The nonlinear refractive index $\hat{n}_2$ is used for $|\tilde{A}(t)|^2$, while n_2 without the hat is used for $I(t)$, which is the light intensity with [17, p. 1048]

$$I(t) = \frac{nc\epsilon_0}{2}|\tilde{A}(t)|^2. \tag{1.25}$$

In obtaining Eq. (1.24) only real valued quantities have been used. However, the equation also holds for complex values of the refractive index and the electric susceptibility if in the last step, in addition to the real valued n_2, also a term $i\alpha_2$ is introduced to account for the intensity dependency of the absorption.

The dependency of the refractive index on light intensity is the optical Kerr effect, and it has been discovered 1875 by John Kerr [25]. It is governed by the $\chi^{(3)}$ coefficient of the medium and is hence classified as a nonlinear $\chi^{(3)}$ process.

1.2.2. Complex refractive index, propagation constant and nonlinear parameter

Before the propagation of pulses in a nonlinear medium can be discussed in the next section, it is necessary to introduce the complex refractive index and some derived quantities, and the consequences of a nonlinear refractive index for these. The obtained relations are used later in this work.

The complex refractive index $\tilde{n}(\omega)$

The complex refractive index $\tilde{n}(\omega)$ of a medium interacting with light is defined like in Eq. (1.23) as [22, p. 27]

$$\tilde{n}(\omega) = \sqrt{1 + \tilde{\chi}(\omega)} = \sqrt{\tilde{\epsilon}_r(\omega)}, \tag{1.26}$$

where $\tilde{\epsilon}_r$ is the complex relative permittivity of the medium. There is some potential ambiguity since many authors use $\tilde{\epsilon}$ instead of $\tilde{\epsilon}_r$ for the relative permittivity. A clear notation is $\tilde{\epsilon}_r = {}^{\tilde{\epsilon}}/_{\epsilon_0}$ [24, p. 6], where $\tilde{\epsilon}$ is the absolute permittivity and ϵ_0 the vacuum permittivity of the medium. Other sources, including the book *Nonlinear Fiber Optics* by Govind P. Agrawal [22, p. 27], from which many of the mathematical procedures described in this work are taken, prefer to drop the index r and just use $\tilde{\epsilon}$ for the relative permittivity. The relative permittivity is a dimensionless quantity, therefore an examination of the dimension of $\tilde{\epsilon}$ clarifies whether it is meant as the relative or the absolute permittivity.

As a complex quantity $\tilde{n}$ can be expressed in its real and imaginary parts $\tilde{n} = n + i\kappa$ [26, p. 258], where n determines the speed of light c_m in the medium with $c_m = {}^{c}/_{n}$, and κ is responsible for absorption losses. In terms of notation the attenuation constant α will be used instead of κ hereafter, with [22, p. 27]

$$\tilde{n} = n + \frac{i\alpha}{2k}, \tag{1.27}$$

where k is the wavenumber. Because of the Kerr effect both n and α have additional nonlinear parts caused by high light intensities and n is replaced with $n \to n + n_2 I$ in accord with Eq. (1.24). The nonlinear part of the attenuation constant α_2 is so small that it can be neglected [22, p. 33]. By introducing the complex envelope $\tilde{A}(t)$ from Eq. (1.7) and normalizing it so that $|\tilde{A}(t)|^2$ is equal to the instantaneous power $P(t)$, Eq. (1.27) can be written as [22, p. 34]

$$\tilde{n} = n + n_2 \frac{|A|^2}{A_{\text{eff}}} + i\frac{\alpha}{2k} = n + \Delta\tilde{n}, \tag{1.28}$$

where A_{eff} is the effective mode area of the beam cross-section. In $\Delta\tilde{n}$ the nonlinear refractive index n_2 and the attenuation α are combined.

The propagation constant $\beta(\omega)$

The propagation constant $\beta(\omega)$ is commonly used in fiber optics in lieu of the spectral phase transfer function $\phi_d(\omega)$ defined in Eq. (1.12). It is the product of the real refractive index n with the vacuum wavenumber k, or the spectral phase transfer function $\phi_d(\omega)$ divided by the length z. Like $\phi(\omega)$ in equation (1.9) it can be expanded in a Taylor series as

$$\beta(\omega) = \beta_0 + \beta_1(\omega - \omega_0) + \frac{1}{2}\beta_2(\omega - \omega_0)^2 + \frac{1}{6}\beta_3(\omega - \omega_0)^3 + ..., \tag{1.29}$$

with

$$\beta_j = \left.\frac{\partial^j \beta(\omega)}{\partial \omega^j}\right|_{\omega_0}. \tag{1.30}$$

According to the complex refractive index $\tilde{n}$ a complex $\tilde{\beta}$ can be defined as

$$\tilde{\beta} = \tilde{n}k = \beta + \Delta\tilde{\beta} \tag{1.31}$$

and

$$\Delta\tilde{\beta} = \Delta\tilde{n}k. \tag{1.32}$$

It is possible to expand $\tilde{\beta}(\omega)$ and $\Delta\tilde{\beta}(\omega)$ in their own respective Taylor series, as is done for $\beta(\omega)$ in Eq. (1.29) and (1.30).

Because $\Delta\tilde{\beta}$ is small in comparison to β, and the higher order terms β_R in the Taylor series expansion of β are small in comparison with β_0, the following approximation can be adopted [22, p. 34]

$$\begin{aligned}\tilde{\beta}^2 - \beta_0^2 &= \beta^2 + \Delta\tilde{\beta}^2 + 2\beta\Delta\tilde{\beta} - \beta_0^2 \\ &= (\beta_0 + \beta_R)^2 + \Delta\tilde{\beta}^2 + 2(\beta_0 + \beta_R)\Delta\tilde{\beta} - \beta_0^2 \\ &\simeq 2\beta_0(\beta_R + \Delta\tilde{\beta}) \\ &\simeq 2\beta_0(\tilde{\beta} - \beta_0).\end{aligned} \tag{1.33}$$

The nonlinear parameter $\gamma(\omega)$

The nonlinear parameter $\gamma(\omega)$ and γ_0, the first coefficient of its Taylor series expansion, are used in fiber optics to calculate the effects of the nonlinear processes during pulse propagation [22, p. 35, 37]. It is defined as

$$\gamma(\omega) = \frac{n_2\omega}{cA_{\text{eff}}}. \tag{1.34}$$

The quantities n_2 and A_{eff} usually depend on the frequency ω in fiber optics [27]. From Eq. (1.28), (1.32) and (1.34) follows that

$$\Delta\tilde{\beta} = \gamma|A|^2 + i\frac{\alpha}{2}. \tag{1.35}$$

$\gamma(\omega)$ can be expanded in a Taylor series same as $\beta(\omega)$.

The propagation constant in a gas medium

The refractive index of a gas medium depends on the pressure p. The starting point for this is the Lorentz-Lorenz equation which states that for a gas at constant temperature [28, p. 88]

$$n^2 - 1 \propto p. \tag{1.36}$$

By replacing $n^2 - 1$ with $(n+1)(n-1)$ and approximating $n + 1 \simeq 2$ for a gas around $p \simeq 1\,\text{bar}$ and $n \simeq 1$, this is reduced to $n - 1 \propto p$ or

$$n = (n_0 - 1)\frac{p}{p_0} + 1, \tag{1.37}$$

where the index 0 denotes a reference pressure, for example $p_0 = 1\,\text{bar}$. From this it is obtained that

$$\frac{\partial^j n(\omega, p)}{\partial \omega^j} = \frac{p}{p_0}\frac{\partial^j n(\omega, p_0)}{\partial \omega^j}. \tag{1.38}$$

It follows from Eq. (1.30) and (1.38) that β_2 and higher coefficients of the dispersion scale directly with pressure p, or that

$$\beta_j(p) = \frac{p}{p_0}\beta_j(p_0) \quad \text{for } j \geq 2. \tag{1.39}$$

For β_0 and β_1 the case is more complicated since these coefficients also include instances of n and not only derivatives of n, and because of that they are not directly proportional to p.

1.3. The pulse propagation equation

The aim of the pulse propagation equation (PPE) is to describe the changes a pulse of light experiences as it propagates through a medium, based on an envelope function representation of the pulse. This includes dispersion and any nonlinear effects which occur in the medium, depending on the intensity of the electric field. In this work the PPE will mostly be attained as by the procedure described in *Nonlinear Fiber Optics* by Govind P. Agrawal [22, p. 25-40].

In a solid-core optical fiber consideration of a delayed response for the nonlinear effects in form of the response function $R(t)$ would result in a slightly more complicated PPE and the addition of an intrapulse Raman scattering term [22, p. 37-40]. However, since this work is concerned with the propagation through a noble gas inside a hollow-core fiber, the PPE derived in this section adopts the approximations already described in section 1.2 and assumes an instantaneous nonlinear response.

This section starts with the Maxwell equations and will move over the wave equation to the Helmholtz equation. Since the Helmholtz equation cannot be solved with analytical methods, the problem will be reduced in complexity by considering it for only one dimension and by applying the slowly varying envelope approximation. The obtained equation will be solved in regard to different terms of the Taylor series expansion of the nonlinear parameter $\gamma(\omega)$, with the first coefficient of the expansion leading to self-phase modulation and the second coefficient leading to self-steepening.

1.3.1. The Hemholtz equation

This work is concerned with problems in the field of classical optics and hence the Maxwell equations are chosen as a starting point. These can be written in a differential form as [22, p. 25]

$$\nabla \mathbf{D} = \rho \tag{1.40}$$

$$\nabla \mathbf{B} = 0 \tag{1.41}$$

$$\nabla \times \mathbf{E} = -\frac{\partial \mathbf{B}}{\partial t} \tag{1.42}$$

$$\nabla \times \mathbf{H} = \mathbf{J} + \frac{\partial \mathbf{D}}{\partial t}, \tag{1.43}$$

where $\mathbf{E}$ is the electric field, $\mathbf{D}$ is the electric flux density, $\mathbf{H}$ is the magnetic field, and $\mathbf{B}$ is the magnetic flux density. The other quantities are the electric charge density ρ and the electric current density $\mathbf{J}$. Bold symbols represent vector quantities.

The relations between the fields and their respective flux densities are given by [22, p. 26]

$$\mathbf{D} = \epsilon_0 \mathbf{E} + \mathbf{P} \tag{1.44}$$

$$\mathbf{B} = \mu_0 \mathbf{H} + \mathbf{M} \tag{1.45}$$

where $\mathbf{P}$ is the polarization, $\mathbf{M}$ is the magnetization, ϵ_0 is the vacuum permittivity, and μ_0 the vacuum permeability. The interaction medium treated in this work is a noble gas inside a hollow-core fiber, which is a non-magnetic medium and hence $\mathbf{M} = 0$. The peak power of the laser pulses used in our experiments is below the critical power for ionization and hence there are no free charges in the interaction medium, or $\mathbf{J} = 0$ and $\rho = 0$.

From equations (1.42) to (1.45) the wave equation can be directly obtained in the form

$$\nabla \times \nabla \times \mathbf{E} = -\frac{1}{c^2}\frac{\partial^2 \mathbf{E}}{\partial t^2} - \mu_0 \frac{\partial^2 \mathbf{P}}{\partial t^2}, \tag{1.46}$$

where c is the speed of light with [24, p. 7]

$$c^2 = 1/\epsilon_0 \mu_0. \tag{1.47}$$

In the noble gas are no free charges as long as the laser power stays below the ionization threshold, and the identity $\nabla \times \nabla \times \mathbf{E} = \nabla(\nabla \mathbf{E}) - \nabla^2 \mathbf{E}$ [22, p. 27] is reduced to

$$\nabla \times \nabla \times \mathbf{E} = -\nabla^2 \mathbf{E}. \tag{1.48}$$

Under the assumption that the electric field $\mathbf{E}$ and the polarization $\mathbf{P}$ are linear polarized, Eq. (1.18) remains valid and in the frequency domain

$$\tilde{\mathbf{P}}(\omega) = \epsilon_0 \tilde{\chi}(\omega) \tilde{\mathbf{E}}(\omega). \tag{1.49}$$

If Eq. (1.46) is Fourier-transformed the operator $\partial/\partial t$ is replaced with $-i\omega$. Together with Eq. (1.48) and (1.49), Eq. (1.46) can then be written as

$$\nabla^2 \tilde{\mathbf{E}}(\mathbf{r}, \omega) = \frac{(-i\omega)^2}{c^2} \tilde{\mathbf{E}}(\mathbf{r}, \omega) + \mu_0 (-i\omega)^2 \epsilon_0 \tilde{\chi} \tilde{\mathbf{E}}(\mathbf{r}, \omega). \tag{1.50}$$

With Eq. (1.26), Eq. (1.47) and the identity $k = \omega/c$, Eq. (1.50) can be written as

$$\nabla^2 \tilde{\mathbf{E}}(\mathbf{r}, \omega) + k^2 \tilde{\epsilon}_r \tilde{\mathbf{E}}(\mathbf{r}, \omega) = 0. \tag{1.51}$$

This is the Helmholtz equation.

1.3.2. 1-dimensional approach

The easiest way to solve the Helmholtz equation (1.51) is to ignore the transversal distribution of $\tilde{\mathbf{E}}(\mathbf{r}, \omega)$ and to consider only one dimension, the propagation direction. Since we are mainly interested in the dynamics and properties of the E field while the beam propagates along the length z of the fiber this is a justified simplification, and it is commonly applied in works about this topic [2, 22, 29]. A comparison between the results of the 1-dimensional model and the 3-dimensional model for a hollow-core fiber by Nurhuda *et al.*, which is also discussed in section 2.2.2, shows that the results for the two models are nearly identical as long as the incident laser power is below a critical value P_{crit} [30]. Beyond that self-focusing leads to a critical deformation of the pulse profile. For propagation inside a waveguide this critical power is given as [31]

$$P_{\text{crit,hcf}} = 0.3 \frac{\lambda^2}{n_2}. \tag{1.52}$$

In our setup, with a central wavelength $\lambda = 800\,\text{nm}$, a nonlinear refractive index $n_2(p) = \frac{p}{1\,\text{bar}}\ 9.4 \cdot 10^{-25}\,\text{m}^2/\text{W}$ [32] and pressure $p = 3\,\text{bar}$, this critical power is $P_{\text{crit,hcf}} = 68\,\text{GW}$. As shown in Fig. 3.4 on page 62, the peak power of the input pulse stays below $P \leq 18\,\text{GW}$ and hence it is justified to apply the 1-dimensional model here.

It is assumed that the light is linear polarized in x direction parallel to the table and perpendicular to the propagation direction, and that this polarization is maintained along the length of the fiber. Measurements with a polarizing cube and a power meter in front and after the hollow-core fiber in our setup have verified this assumption. This allows to treat the electric field vector $\tilde{\mathbf{E}}(\mathbf{r}, \omega)$ as a scalar $\tilde{E}(\mathbf{r}, \omega)$ in x direction.

As is done in section 1.1.2, the scalar electric field is now expressed in an envelope form in both time and frequency domain [22, p. 33-34]

$$\begin{aligned} \tilde{E}(\mathbf{r},\omega) &= F(x,y)\tilde{A}(z,\omega)e^{i\beta_0 z} \\ E(\mathbf{r},t) &= \frac{1}{2}F(x,y)\tilde{A}(z,t)e^{i(\beta_0 z-\omega_0 t)} + \text{c.c.} \end{aligned} \tag{1.53}$$

with a complex envelope $\tilde{A}$ and a carrier frequency ω_0. $F(x,y)$ is the transverse modal distribution.

Eq. (1.53) is now inserted into Eq. (1.51) and solved either by separation of variables [22, p. 34] or by directly letting $F(x,y)$ drop, which leads to identical results since $F(x,y)$ does not contribute to a 1-dimensional solution. Following the latter procedure, Eq. (1.51) can be written as

$$\begin{aligned} 0 &= \frac{\partial^2}{\partial z^2}\left(\tilde{A}e^{i\beta_0 z}\right) + k^2\tilde{\epsilon}_r\tilde{A}e^{i\beta_0 z} \\ &= \frac{\partial}{\partial z}\left(\tilde{A}'e^{i\beta_0 z} + i\beta_0\tilde{A}e^{i\beta_0 z}\right) + k^2\tilde{n}^2\tilde{A}e^{i\beta_0 z} \\ &= \tilde{A}'' + 2i\beta_0\tilde{A}' - \beta_0^2\tilde{A} + \tilde{\beta}^2\tilde{A}, \end{aligned} \tag{1.54}$$

where $\tilde{A}'$ denotes a derivative with respect to z and $\tilde{\beta}$ is defined as in Eq. (1.31).

Now the slowly varying envelope approximation (SVEA) is introduced. The SVEA assumes that the envelope of the light pulse is only slowly varying in either t or z in comparison to the carrier frequency. Originally it has been expected that the SVEA loses physical validity as the duration of the pulse envelope approaches the carrier oscillation period, or equivalently when the bandwidth of the propagating field approaches the carrier frequency [2, p. 1134]. It has been shown in various studies, e.g. [33], that the SVEA or very similar concepts can be extended down to pulses in the single cycle regime. Since this work is treating pulses with a duration of 30 fs it is justified to apply the SVEA to the calculations done here.

The benefit of the SVEA in this case is that it permits to neglect the $\tilde{A}''$ term in Eq. (1.54). Then the approximation of Eq. (1.33) is used to obtain

$$i\frac{\partial\tilde{A}}{\partial z} + (\tilde{\beta} - \beta_0)\tilde{A} = 0. \tag{1.55}$$

1.3.3. Self-phase modulation

The nonlinear parameter $\gamma(\omega)$ has already been introduced in Eq. (1.34). It can be expanded in a Taylor series and if the expansion is stopped after the first term, which amounts to neglecting the frequency-dependency of γ, one obtains

$$\gamma(\omega) \simeq \gamma_0 = \frac{n_2(\omega_0)\omega_0}{cA_{\text{eff}}(\omega_0)}. \tag{1.56}$$

If Eq. (1.31), (1.35) and (1.56) are inserted in the bracket of Eq. (1.55), it can be written as

$$\begin{aligned}(\tilde{\beta} - \beta_0) &= (\beta - \beta_0 + \Delta\tilde{\beta}) \\ &= (\beta - \beta_0 + \gamma_0|A|^2 + i\frac{\alpha}{2}).\end{aligned} \tag{1.57}$$

The propagation constant $\beta(\omega)$ is expanded to its 3rd order term, and Eq. (1.55) can be written as

$$\frac{\partial\tilde{A}}{\partial z} = i\left(\beta_1(\omega-\omega_0) + \frac{1}{2}\beta_2(\omega-\omega_0)^2 + \frac{1}{6}\beta_3(\omega-\omega_0)^3 + i\frac{\alpha}{2} + \gamma_0|A|^2\right)\tilde{A}, \tag{1.58}$$

which is inverse Fourier-transformed, using the replacement $(\omega - \omega_0) \to i\partial/\partial t$, to obtain

$$\frac{\partial A}{\partial z} = -\beta_1\frac{\partial A}{\partial t} - i\frac{1}{2}\beta_2\frac{\partial^2 A}{\partial t^2} + \frac{1}{6}\beta_3\frac{\partial^3 A}{\partial t^3} - \frac{\alpha}{2}A + i\gamma_0|A|^2A. \tag{1.59}$$

Then the time t is substituted with the retarded time $T = t - z/v_{gr} = t - \beta_1 z$ and the length z with $\xi = z$. That introduces a frame of reference moving along with the pulse at the group velocity $v_{gr} = 1/\beta_1$, and it follows that $\partial/\partial t = \partial/\partial T$ and $\partial/\partial z = \partial/\partial\xi - \beta_1\partial/\partial t$. The result is

$$\frac{\partial A}{\partial z} = -i\frac{1}{2}\beta_2\frac{\partial^2 A}{\partial T^2} + \frac{1}{6}\beta_3\frac{\partial^3 A}{\partial T^3} - \frac{\alpha}{2}A + i\gamma_0|A|^2A. \tag{1.60}$$

The terms with β_j describe the dispersion occurring in the medium, respectively the group delay dispersion (GDD) and third order dispersion (TOD). Higher order coefficients can be added at need. The α term describes absorption losses in the gas-filled hollow-core fiber, and the γ_0 term finally is responsible for self phase modulation (SPM) in its basic form and hence the generation of new frequencies in the pulse spectrum.

Eq. (1.60) and its variants like Eq. (1.62) are referred to as the nonlinear Schroedinger equation (NLSE).

1.3.4. Self-steepening

In obtaining Eq. (1.60) $\gamma(\omega)$ has been expanded only to the zero order coefficient of its Taylor series and the dependency of the nonlinear process on the frequency has been neglected. If a linear dependency on the frequency is included and the expansion of $\gamma(\omega)$ is done to the first order term instead, the respective coefficient is

$$\begin{aligned}\gamma_1 &= \left.\frac{\partial\gamma}{\partial\omega}\right|_{\omega_0} = \left.\frac{\partial}{\partial\omega}\frac{n_2(\omega)\omega}{cA_{\text{eff}}(\omega)}\right|_{\omega_0} = \frac{\gamma_0}{\omega_0} + \frac{\gamma_0}{n_2}\left.\frac{\partial n_2}{\partial\omega}\right|_{\omega_0} - \frac{\gamma_0}{A_{\text{eff}}}\left.\frac{\partial A_{\text{eff}}}{\partial\omega}\right|_{\omega_0} \\ &\simeq \frac{\gamma_0}{\omega_0},\end{aligned} \tag{1.61}$$

where $\partial n_2/\partial\omega$ and $\partial A_{\text{eff}}/\partial\omega$ have both been dropped. In the case of an optical fiber with a solid fused silica core $A_{\text{eff}}(\omega)$ can be calculated [27], but for a hollow-core fiber A_{eff} is approximated as constant with no dependency on the frequency [8, 16]. The dependency on frequency for n_2 is usually discarded as being negligible far from the ultraviolet resonances [27], and that is even more true for neon ($\lambda_{\text{res}} \simeq 74\,\text{nm}$) than for fused silica($\lambda_{\text{res}} \simeq 116\,\text{nm}$) [21, 20].

The expansion term $\gamma_1(\omega - \omega_0)$ is added to Eq. (1.57), and instead of Eq. (1.60) one finally obtains

$$\frac{\partial A}{\partial z} = -i\frac{1}{2}\beta_2\frac{\partial^2 A}{\partial T^2} + \frac{1}{6}\beta_3\frac{\partial^3 A}{\partial T^3} - \frac{\alpha}{2}A + i\gamma_0|A|^2A - \frac{\gamma_0}{\omega_0}\frac{\partial}{\partial T}(|A|^2A). \tag{1.62}$$

The last term on the right-hand side is responsible for self-steepening, and its effects on the nonlinear process and the generation of new frequencies will be discussed in detail in section 2.2.3. It is inclusion of this term in the NLSE which allows to expand SVEA methods into the regime of single-cycle pulses [33].

Eq. (1.62) is the propagation equation as it is used for the numerical calculations throughout this thesis.

1.4. Self-phase modulation

This work concerns itself predominantly with the generation of new frequencies in a hollow-core fiber, and because of that the effects of self-phase modulation (SPM) merit some further discussion. SPM is the driving mechanism behind the generation of new frequencies and has been introduced as a mathematical term of the PPE in section 1.3.3. The aim of this section is to convey a more intuitive and practical view of SPM and its consequences.

1.4.1. SPM in the time domain

To establish a better understanding of SPM it is helpful to visualize its effect on the pulse's instantaneous frequency. The instantaneous frequency $\omega(t)$ is the derivative of the temporal phase, as introduced in Eq. (1.2), with respect to time t and can be understood as the average frequency of the pulse at any given time.

If the electric field of a bandwidth-limited pulse is defined similar to Eq. (1.53) as

$$E(z,t) = \frac{1}{2}\tilde{A}(z,t)e^{-i(\omega_0 t - \beta_0 z)} + \text{c.c.}, \tag{1.63}$$

then the instantaneous frequency $\omega(t)$ is, under consideration of Eq. (1.24),

$$\begin{aligned}\omega(t) &= \frac{\partial}{\partial t}(\omega_0 t - nk(\omega_0)z) \\ &= \omega_0 - n_2 k(\omega_0) z\frac{\partial}{\partial t}I.\end{aligned} \tag{1.64}$$

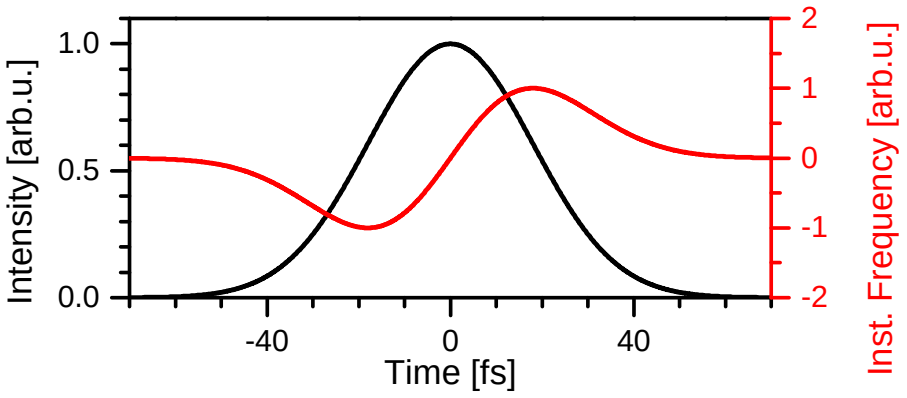

Figure 1.1.: Instantaneous frequency of a short pulse which has experienced SPM. The input pulse is bandwidth-limited and its instantaneous frequency (not shown) is constant at ω_0. The temporal pulse shape (black) remains unchanged by SPM. The instantaneous frequency after SPM (red) is given in arbitrary units centered on ω_0 and is normalized on the maximum frequency shift.

From this follows that at each moment the instantaneous frequency $\omega(t)$ is changed to a new frequency which depends on $\partial/\partial t I$, as illustrated in Fig. 1.1. Due to the minus sign in Eq. (1.64) new frequencies generated at the rising slope of a short pulse are below the carrier frequency ω_0, and at the trailing edge new frequencies higher than ω_0 are generated.

1.4.2. SPM in the frequency domain

In Fig. 1.2 a) the spectrum of a pulse which has experienced SPM is illustrated. It consists of two high sidewings and several lesser oscillations between them, which is a characteristic appearance for a SPM spectrum neglecting self-steepening and it can be explained with the help of Fig. 1.1. The two side wings correspond to the frequencies generated by the maximum shift of the instantaneous frequency. The frequencies between these peaks are generated at two different moments in time respectively, and the oscillations belong to the interference pattern of these two contributions. As the pulse propagates through a nonlinear medium new peaks arise at the central frequency, split in two and drift apart.

The spectral phase of the pulse is depicted in green and the group delay, the derivative of the spectral phase with respect to frequency, is depicted in red in Fig. 1.2 a). With the exception of the carrier-envelope phase the group delay carries the same information as the spectral phase, but presents it in a way in which some characteristic features become more readily apparent, as for example the position of the group delay peaks at minima of the spectrum. For that reason the group

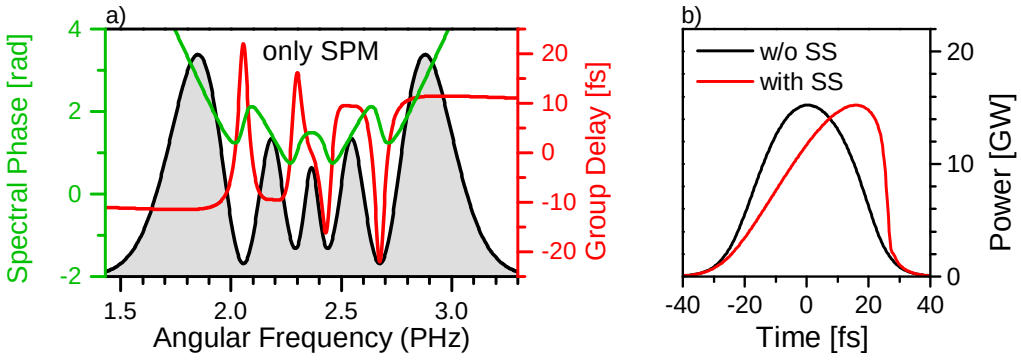

Figure 1.2.: a) Spectral amplitude (black), phase (green) and group delay (red) of an example pulse which has experienced SPM. The effects of dispersion and self-steepening have been omitted. The linear scale for the spectrum is not shown. In b) the temporal pulse shape once without self-steepening (but including SPM and dispersion), and once with self-steepening. The ordinate of b) depicts the temporal power, the intensity is obtained by division by $A_{\text{eff}} \simeq 0.48\pi a^2$ [8].
(Parameters: input Gaussian pulse $\tau_0 = 28\,\text{fs}$, $\phi(\omega) = 0$, $\omega_0 = 2.36\,\text{PHz}$, $E = 830\,\mu\text{J}$ per pulse; HCF length $z = 1\,\text{m}$, bore radius $a = 125\,\mu\text{m}$, neon gas $p = 2\,\text{bar}$)

delay will often be illustrated in addition to or instead of the actual spectral phase throughout this work.

1.4.3. Self-steepening

As can be seen in Eq. (1.62), the self-steepening term is a real quantity and as such acts directly on the temporal pulse envelope and not on the phase. It is hence a less abstract concept than self-phase modulation and its basic effect is simple to visualize. The effect of self-steepening on the temporal pulse shape is illustrated in Fig. 1.2 b).

Because of the Kerr effect, the nonlinear increase of the refraction index caused by the light intensity, different parts of the pulse in the time domain will have slightly different group velocities. Since the refraction index is higher at the points of higher intensity, the pulse peak actually moves slower than the peak slopes. In consequence the rising slope moves away from the main pulse and becomes broader, while the trailing slope moves towards the main peak and hence becomes steeper. This self-steepening of the pulse's trailing edge is what gives this effect its name.

Since a steeper edge has a higher gradient, SPM will be enhanced for the pulse's trailing slope. The interplay between these two effects and the consequences for the pulse will be discussed in section 2.2.3.

1.5. Time-frequency representations

In the previous sections various properties of short pulses are discussed, and how they behave in either the time or the frequency domain. However, a representation in either domain fails to visualize the behavior of the pulse in the other domain. When depicting a pulse of light in the frequency domain, for example, all the information about its behavior in the time domain is encoded in its phase, which is not always intuitive to read. There are several approaches to represent transient signals in both time and frequency domain at the same time, to visualize properties in a light pulse which are difficult to discern just from the envelope and phase plots in either domain. The purpose of any time-frequency representation is to estimate the strength of the frequency ω at time t. It is only possible to do this in approximation though, since the uncertainty principle precludes a perfect simultaneous description of both time and frequency [34, p. 8], and every time-frequency representation comes with limitations.

For a thorough account of different time-frequency representations I refer to the doctoral thesis of S. C. Bradford from the California Institute of Technology [34].

In this section two methods of time-frequency representation are introduced. The first is the short-time Fourier-transform (STFT) spectrogram, a very basic method. It is limited in its resolution and can present detailed information in one domain only at a loss of accuracy in the other. The other method is the Wigner-Ville distribution, which is able to depict a detailed view in both domains at once, but comes with complications like interference patterns and negative values. Nonetheless the Wigner-Ville distribution is used to illustrate particular pulse properties of both measured and calculated pulses throughout this work.

1.5.1. The STFT spectrogram

For a given signal $x(t)$ in the time domain it is possible to use the Fourier-transform of Eq. (1.4) to look at the spectrum of this signal at any time t. A sliding time window can then be employed this way to generate a time-frequency representation. This is done with the short-time Fourier-transform (STFT), which is defined as [34, p. 18]

$$\mathrm{STFT}(t,\omega) = \int_{\infty} x(\tau)h^*(\tau - t)e^{-i\omega\tau}\,\mathrm{d}\tau, \tag{1.65}$$

where $h(t)$ is the function of the time window and can have different forms. The spectrogram is the squared amplitude of the STFT. In Fig. 1.3 three spectrograms with different lengths of a Gaussian time window are presented, which demonstrate the fundamental issue with STFT spectrograms. As example a short pulse which has experienced self-phase modulation, but not dispersion or self-steepening, is chosen. A short time window as in Fig. 1.3 a) provides good detail in the time domain properties of the presented pulse, as observable in Fig. 1.3 e). The spectrum is reduced to a double peak though and does not resolve the central oscillations of the

original spectrum, as observable in Fig. 1.3 d). Accordingly a long time window resolves these central peaks in the spectrum, but the features of the pulse shape are smeared broadly in time. A time window which has a length in between the two previously chosen, as a compromise, results in a spectrogram which is unsatisfactory in both domains.

However, it is not possible to resolve the features in both the time and the frequency domain at once in detail. Nonetheless the STFT spectrogram is used for the representation of ultra short laser pulses at occassion, as for example in [35].

1.5.2. The Wigner-Ville distribution

Wigner proposed this method 1932 for a joint representation of position and momentum in quantum mechanics [36], and Ville adapted it 1948 to the equally related pair of time and frequency in the area of signal processing [37]. The Wigner-Ville distribution permits a time-frequency representation with more detail in both the time and frequency domain at once than a STFT spectrogram. Mathematically it is defined as [38, p. 3]

$$\mathcal{W}(t,\omega) = \int_{\infty} z(t+\frac{\tau}{2}) z^*(t-\frac{\tau}{2}) e^{-i\omega\tau}\,\mathrm{d}\tau, \tag{1.66}$$

where $z(t)$ is the analytic signal of a real-valued signal $x(t)$. The analytic signal serves as a complex representation of a real signal and is also called the analytic associate or analytic representation of a signal. It is defined as [38, p. 3]

$$z(t) = x(t) + i\mathcal{H}(x(t)). \tag{1.67}$$

$\mathcal{H}(x(t))$ is the Hilbert-transformation of the signal $x(t)$. It follows that the analytic signal for $E(t)$ is $\tilde{E}^+(t)$, the quantity already introduced in section 1.1.1.

From Eq. (1.66) can be obtained that [18, p. 13]

$$\begin{aligned} \int_{\infty} \mathcal{W}(t,\omega)\mathrm{d}t &= |\tilde{E}(\omega)|^2 \\ \int_{\infty} \mathcal{W}(t,\omega)\mathrm{d}\omega &= 2\pi|\tilde{E}(t)|^2. \end{aligned} \tag{1.68}$$

From this follows that the integral of $\mathcal{W}(t,\omega)$ along the time axis is equal to the spectrum $P(\omega)$ of the signal $E(t)$, and that the integral along the frequency axis is equal to the instantaneous power $P(t)$ of the signal. This provides an intuitive relationship between the Wigner-Ville distribution and the spectrum and pulse shape of a signal which is lacking in the STFT spectrogram, as demonstrated in Fig. 1.3.

However, while $\mathcal{W}(t,\omega)$ is always real-valued it can assume negative values, which precludes a straight interpretation of $\mathcal{W}(t,\omega)$ as the energy of the signal at a specific time and frequency. These negative values occur because of cross-term interference between $z(t)$ and $z^*(t)$, or $\tilde{E}^+(t)$ and $\tilde{E}^{+^*}(t)$, when multiple frequency components are present in the signal [34, p. 24].

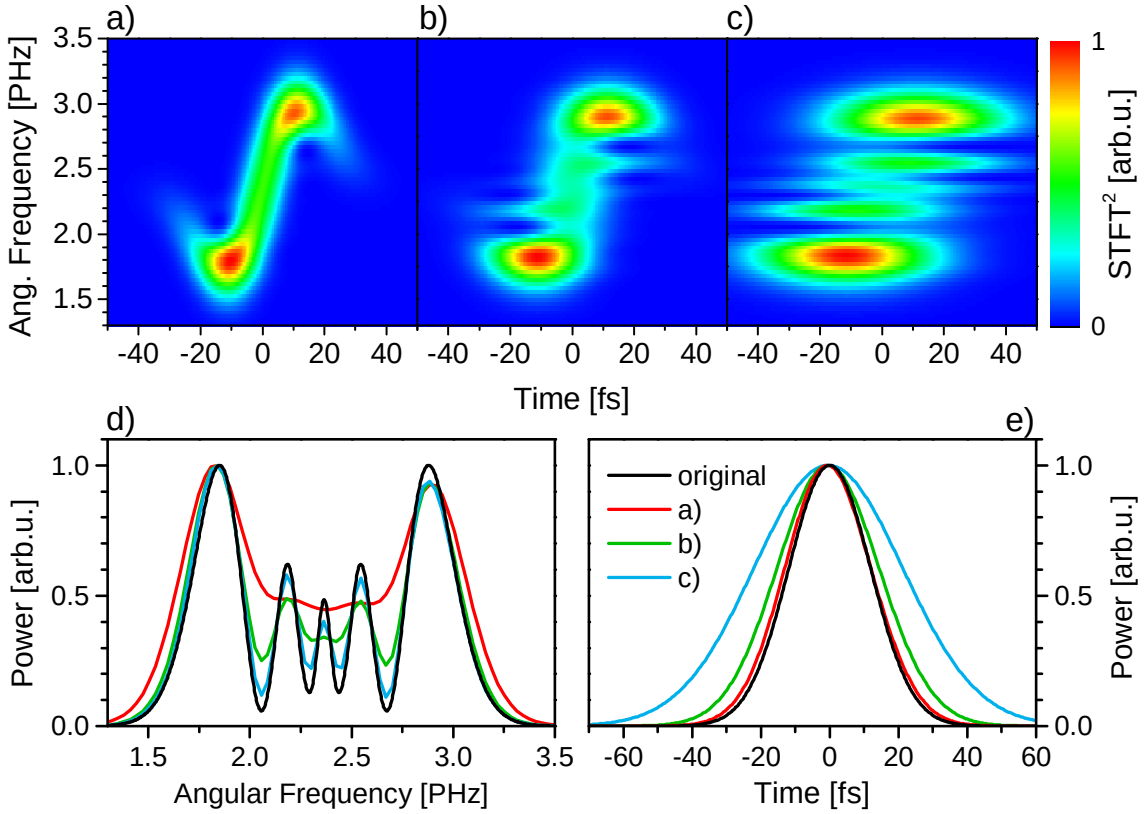

Figure 1.3.: a)-c) STFT spectrograms of a pulse which has experienced SPM with a Gaussian time window of three different lengths. The time window in a) has a length of 50 fs, in b) 100 fs, and in c) 200 fs. d) Calculated spectral amplitude (black) and the integral $\int \mathrm{STFT}^2\, dt$ for each time window (color). e) Calculated temporal power (black) and the integral $\int \mathrm{STFT}^2\, d\omega$ for each time window (color).
(Parameters: input Gaussian pulse $\tau_0 = 28\,\mathrm{fs}$, $\phi(\omega) = 0$, $\omega_0 = 2.36\,\mathrm{PHz}$, $E = 830\,\mu\mathrm{J}$ per pulse; HCF length $z = 1\,\mathrm{m}$, bore radius $a = 125\,\mu\mathrm{m}$, neon gas $p = 2\,\mathrm{bar}$)

It is possible to reduce this cross-term interference with the application of different smoothing windows in both time and frequency domain [34, p. 28-29], but this is beyond the scope of this thesis. Where it is considered helpful for visualization, the Wigner-Ville distribution as defined above is used for time-frequency representations throughout this work.

Fig. 1.4 shows exemplary Wigner plots for four different short pulses to demonstrate the usefullness of this method for pulse visualization. In b) a pulse with a linear upchirp is depicted and the continuous shift in the spectrum to higher frequencies with an increase in time is clearly visible in the Wigner plot.

In c) a pulse with negative TOD is depicted and its temporal pulse shape demonstrates the characteristic prepulses. In the respective Wigner plot the presence of negative values for $\mathcal{W}(t, \omega)$ is visible.

The pulse in d) has experienced SPM and is the same pulse as depicted in Fig. 1.2 a), since dispersion and self-steepening have not been considered. The patterns of cross-term interference are apparent. This Wigner plot can be directly compared to the STFT spectrograms in Fig. 1.3 since these were calculated by using the same exemplary pulse. The high intensity parts of this Wigner plot convey the same basic behavior as Fig. 1.3 a), but with a better resolution, and correspond to a nearly linear shift of frequency with time similar to Fig. 1.4 b). It follows that the dispersion of the pulse is mostly GDD. This is the explanation why a SPM-modified pulse can be compressed to short pulse durations just by application of negative GDD with, for example, a chirped mirror compressor.

Because of the cross-term interference the Wigner-Ville distribution is not commonly used in ultra short pulse analysis. However, while the value of $\mathcal{W}(t, \omega)$ does not strictly represent pulse energy it still holds true that the pulse energy will be high at high values of $\mathcal{W}(t, \omega)$ and low for low or negative values of $\mathcal{W}(t, \omega)$ [34, p. 8]. In *Ultrashort Laser Pulse Phenomena* Diels and Rudolph [18, p. 12-18] comment on the Wigner-Ville distribution and use it to define the instantaneous frequency $\omega(t)$, and in [39] the Wigner-Ville distribution is used as a tool for analyzing nonlinear pulse propagation in optical fibers. In this thesis the Wigner-Ville distribution is used to visualize particular properties of the discussed pulses when it is helpful to do so, but always with the caveat that it can not be read as simply representing the pulse energy at a specific time and frequency. Which would be a physical impossibility due to the uncertainty between time and frequency.

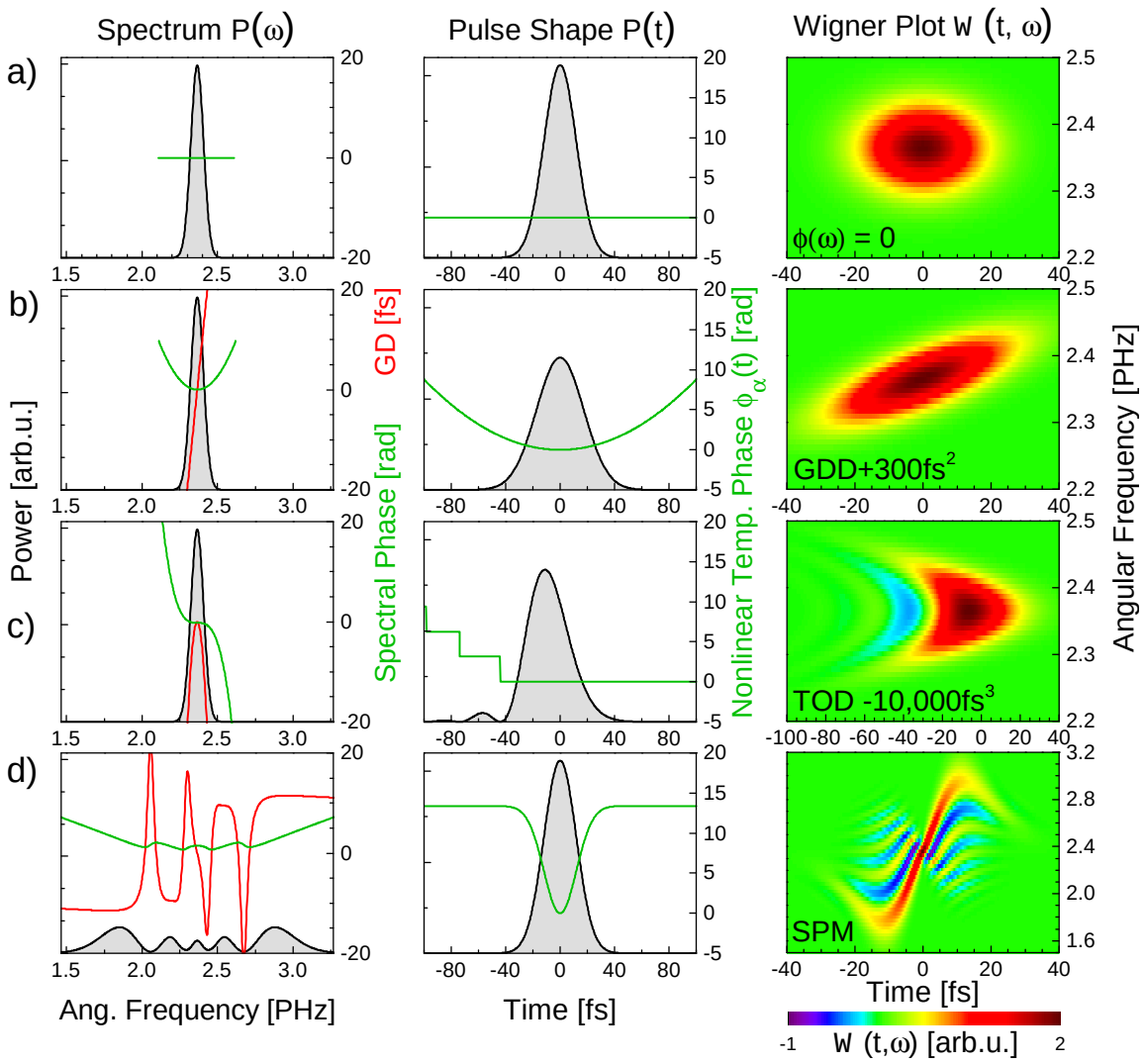

Figure 1.4.: Spectral amplitude $P(\omega)$, spectral phase $\phi(\omega)$, group delay, pulse shape $P(t)$, the nonlinear part of the temporal phase $\phi_a(t)$ (from Eq. (1.2)) and Wigner plot $\mathcal{W}(t,\omega)$ for four different exemplary pulses. In a) a Gaussian pulse with $\tau_0 = 28\,\mathrm{fs}$ and a spectral phase of zero is depicted, in b) the same pulse with GDD $+300\,\mathrm{fs}^2$, in c) the same pulse with TOD $-10.000\,\mathrm{fs}^3$, and in d) the pulse from a) after experiencing SPM (no dispersion, no self-steepening). The plots for the spectral phase and group delay use a scale with the same numbers but different units respectively. The intensities for the Wigner plots are normalized and can not be compared in their absolute intensity values. Note that the Wigner plot for c) has a different time scale and the plot for d) has a different frequency scale than the other Wigner plots.
(Parameters for SPM simulation as in Fig. 1.2)

2. Methods

Supercontinuum generation is a subject which has been extensively studied since the first broadly successful experiment of Alfano and Shapiro in 1970 [4]. The medium of choice for these studies are usually optical fibers or photonic crystal fibers with a solid core, and a comprehensive review of this field was done in 2006 by Dudley *et al.* [2].

In 1997 Nisoli *et al.* [9] demonstrated the first use of a gas-filled hollow-core fiber to generate a supercontinuum with few-cycle pulses in the gigawatt regime. High power pulses like these were consequently used for high harmonic generation (HHG) as a table top source for coherent extreme ultraviolet (XUV) radiation [40], and in 2001 these methods were expanded to generate single light pulses with a duration of attoseconds [10]. In 2007 Cavalieri *et al.* [12] studied inner shell states in single-crystalline tungsten with such attosecond pulses, generated by application of a hollow-core fiber supercontinuum. The beamline in the attosecond laboratory at University Bielefeld follows the same basic setup as the beamline used by Cavalieri *et al.* in Munich.

Several different gating schemes are researched to extract isolated light pulses of attosecond duration out of the attosecond pulse trains created by high harmonic generation. A discussion of these gating techniques is given in the recent review paper from Sansone *et al.* [41]. To date the most successful of these schemes all require the application of intense ultrashort laser pulses in the few-cycle regime with a duration of about 5 fs or less. As has been discussed in section 1.1.3 the duration of a pulse of light is related to its spectral bandwidth, and only the very broad spectral bandwidth of a supercontinuum makes it possible to provide the ultrashort pulses necessary to generate isolated attosecond pulses. Because of that the control and optimization of the created supercontinuum are important parts of any time-resolved experiment advancing beyond the femtosecond regime.

In this chapter the different methods used to study supercontinuum generation in this thesis are presented and discussed, starting with a description of the experiment in section 2.1 and covering the numerical simulation in section 2.2.

2.1. Experiment

The attosecond beamline of Universitaet Bielefeld uses a commercial system, consisting of the *FemtoSource Rainbow*, the *FemtoPower compact PRO* and the *Kaleido-*

scope from *FemtoLasers*, to generate ultrashort high power laser pulses with a pulse duration of two periods of the carrier frequency. Section 2.1.1 provides a detailed description of the light source and the experimental setup as far as it is of concern for this work. For a description of the attosecond-resolved photoelectron spectroscopy experiment I refer to section 3.1 and the master theses of Sergej Neb and Christian Sander [42, 43]. Since all the experiments presented in this thesis resolve around supercontinuum generation in a gas-filled hollow-core fiber, section 2.1.2 describes the adjustment procedure of the hollow-core fiber. In section 2.1.3 the operating principle of a SPIDER is explained, an instrument capable of characterizing the spectral phase of a laser pulse.

2.1.1. Experimental setup

The light source in the attosecond laboratory is the Ti:sapphire oscillator *FemtoSource Rainbow* from *FemtoLasers*. It is pumped with 4.9 W by a *Verdi V5*, a diode-pumped solid-state (DPSS) laser from *Coherent*. This system provides a seed pulse of 3 nJ at a central wavelength of 800 nm, with a pulse duration specified as less than 7 fs and a repetition rate of about 80 MHz. The carrier-envelope phase (CEP) of the laser pulses is stabilized such that every fourth pulse has the same CEP. This is accomplished with an acousto-optic modulator (AOM) inside the *Rainbow*. The fast CEP fluctuations are measured by a f-to-2f interferometer and the AOM is then used to modulate pump power to minimize these fluctuations and hence stabilize the CEP.

Fig. 2.1 shows an overview of the experiment setup as far as it is of concern to this work. A setup of the experiment for attosecond-resolved photoelectron spectroscopy is shown in section 3.1.

The oscillator pulses serve as seed light for a chirped pulse amplifier (CPA) *FemtoPower compact PRO* from *FemtoLasers*. As a CPA system the amplifier consists basically of three parts. In the stretcher the incident pulses pass twice through a 5 cm long slab of SF-57 Schott glass to increase pulse duration by several orders of magnitude. This makes it possible to further increase the pulses' energy while staying below the damage threshold of the optical components and without inducing undue self-phase modulation because of high intensities. The actual amplification is done in a multipass arrangement. The laser medium is a Ti:sapphire crystal, which is cooled with a Peltier element and pumped at 1 kHz with 10.4 W by an *Etna* DPSS laser from *Thales*. After half of the passes a Pockels cell is used to select a seed pulse with appropriate energy and pulse-to-pulse stability, setting the system to a repetition rate of the *Etna's* 1 kHz. Then the pulses pass through a prism compressor to decrease pulse duration down to about 30 fs. Since the pulses' spectrum suffers a decrease in bandwidth during amplification, it is not possible to reach the same pulse duration as the pulses have before the CPA.

After the pulses have left the CPA a small part of the beam is branched off with a beam splitter to another f-to-2f interferometer. Here the CEP is checked again and

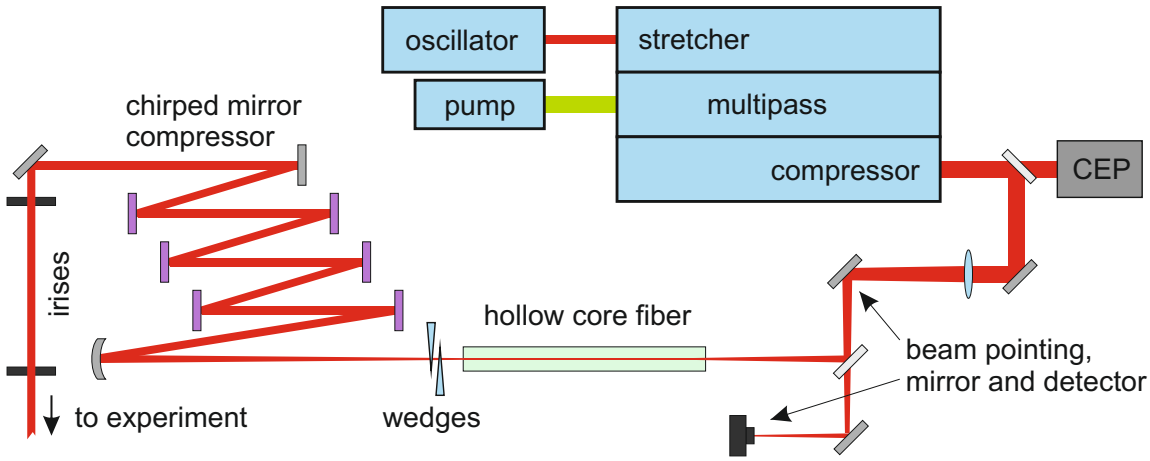

Figure 2.1.: Beamline setup. Ultra short laser pulses are generated in an oscillator and amplified in a CPA amplifier consisting of a stretcher, a multipass amplifier and a prism compressor. A f-to-2f interferometer checks the carrier-envelope phase and sends feedback to the oscillator to ensure stabilization of the CEP. Beam position is controlled by a beam pointing system consisting of one steerable mirror and a detector. The light pulses are focused with a lense into a hollow-core fiber filled with neon gas. Wedges positioned after the fiber allow for fine tuning of the dispersion. The beam is collimated with a spherical mirror and the pulses are compressed in a chirped mirror compressor. Afterwards the pulses are sent towards the photoelectron experiment.

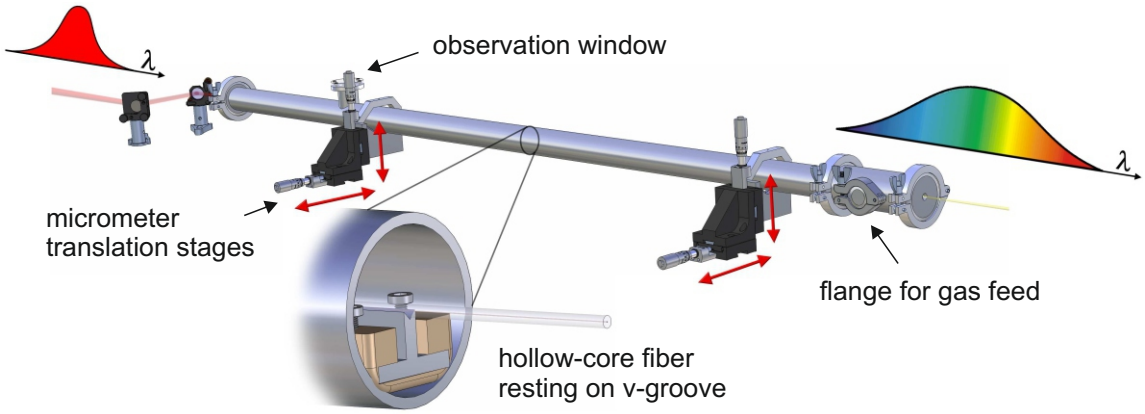

Figure 2.2.: The gas-filled hollow-core fiber (HCF). It has a length of 1 m, an inner diameter of 250 µm, and is filled with neon at a gas pressure between 0.05 and 3 bar.

feedback sent back to the oscillator's AOM, to ensure that the 1 kHz pulses are still CEP-stabilized after the optical path length inside the CPA. This is an imperative requirement for the experiments described in section 3.1, but will be of no relevance for the contend of this work.

To reduce the pulse duration down into the few-cycle regime it is necessary to increase the bandwidth of the pulses' spectrum considerably. This generation of new frequencies is only possible in a nonlinear process, and the resulting spectrum is often described as a supercontinuum. The driving mechanism responsible for this is self-phase modulation (SPM) of a high-intensity laser beam in a nonlinear medium. While it is possible to do this in a bulk medium, the process is much more efficient if the beam is lead inside a waveguide. Optical fibers made of fused silica are suited well to this, but do not allow the high throughput of energy required for our experiments. Hence we are using a hollow-core fiber filled with noble gas, as it is illustrated in Fig. 2.2.

The *Kaleidoscope* hollow-core fiber compressor from *FemtoLasers* is a commercial system complete with a chirped mirror compressor. The hollow-core fiber is made of fused silica and is 1 m long, has a diameter of 3 mm and an inner bore diameter of 250 µm. It has to lie straight and rests without application of force on an aluminum v-groove. The fiber is placed inside a pressure chamber which allows for gas pressures between 0.05 and 3 bar. The beam enters and leaves the chamber through windows of 1 mm fused silica, which are aligned in Brewster angle in respect to the beam's linear polarization to enable maximum transmission. It is possible to look at the fiber's front end through a window. The whole pressure chamber rests on two micrometer XY translation stages to provide for an exact control of the fiber's alignment in regard to the beam, and the support point of the front end stage has been put exactly under

the fiber's front end. This way the fiber's back end can be moved with minimal changes to front end position.

This is a static setup, with the same gas pressure applying to the whole length of the hollow-core fiber. It is also a common setup to provide for a steady gas flow and pressure gradient by setting different gas pressures at each end of the hollow-core fiber. This is especially useful to prevent ionization at the fiber's entrance while still maintaining high gas pressure and high laser power [44]. A similar if more complicated way to set this up is a steep temperature gradient along the fiber [45]. In this work the dependency of the white light generation process on the gas pressure in the hollow-core fiber is studied, and hence a static pressure setup is preferable.

Neon with a purity of 4.5 or 4.0, which is equal to a purity of 0.99995 or 0.9999 respectively, is used as noble gas inside the hollow-core fiber. Other setups often use argon instead of neon due to its greater nonlinear refraction index n_2, which is about an order of magnitude higher than for neon [32]. However, the critical power at which self-focusing and ionization leads to deformation of the pulse scales inversely to n_2 [31], so neon allows for the application of higher laser power. In experiments where the focus lies on the process of frequency generation argon is usually chosen as medium [15, 46], while for applications which require high power, like high harmonic generation for the photoelectron spectroscopy experiment down the line, neon is usually chosen as gas medium in the hollow-core fiber [8, 12].

In front of the pressure chamber of the hollow-core fiber is a beam steering system installed to ensure a stabilized position of the laser beam, since the frequency generation process is extremely sensitive to any change of alignment between beam and fiber. A setup with only one steerable mirror already achieves good results in beam stability. Details about this non-commercial beam stabilization system can be looked up in the master thesis of Emanuel Marschewski [47].

The power of the laser beam is measured in front of and after the pressure chamber of the hollow-core fiber with a thermal sensor from *Ophir Photonics*. The incident power is about $P = 830\,\mathrm{mW}$, which corresponds to an energy of $830\,\mu\mathrm{J}$ per pulse in a $1\,\mathrm{kHz}$ system. After the hollow-core fiber, but without the wedges, the pulses have an energy of about $550\,\mu\mathrm{J}$ per pulse, resulting in an overall transmission of 66% through the fiber. Measurements performed in the amplifier before compression of the pulses in the prism compressor demonstrate a pulse-to-pulse energy stability of better than 1%.

To couple the laser beam into the hollow-core fiber it is focused with a plano-convex lens made of fused silica with a focal length of 1.5 m, which has an anti reflex coating on both sides. Measurements with a beam profiler, a *WinCamD* CCD camera from *Data Ray*, have shown that the $1/e^2$ beam waist in focus, at entry into the hollow fiber, is around $200\,\mu\mathrm{m}$ in diameter. Upon exit from the fiber the beam is divergent and is collimated by a spherical mirror with a focal length of 1 m. Shortly after the hollow-core fiber, before the beam radius is getting too wide, a pair of thin fused silica wedges is placed to fine tune the pulses' dispersion for optimal compression. They have no anti reflex coating. The wedges can be aligned in Brewster angle in

regard to the beam to allow for minimal reflection losses, but in practice this causes an undesirable displacement of the beam when the wedges are moved in or out more than a small amount. For this reason the wedges are put nearly perpendicular into the beam for most applications. The wedges are not inserted exactly perpendicular though, since we have found that the back reflex from the front wedge will find its way back through the fiber, the compressor, the multipass and the stretcher, to be detected in the 2-to-2f interferometer of the oscillator.

After the beam has been collimated it enters a compressor consisting of six chirped mirrors. These compensate for the dispersion which is added to the pulses inside the gas-filled hollow-core fiber, the propagation distance in air and by passing through dispersive optical components like the wedges or the glass windows of the pressure chamber. The exact amount of dispersion compensated by the chirped mirror compressor is estimated from measurements later in section 3.4.

Finally the beam passes through two irises to fix its position, and is directed towards experiment and beam analysis.

2.1.2. Adjustment of the hollow-core fiber

The adjustment of the hollow-core fiber and its alignment in regard to the input laser beam is a critical parameter in the experiment. Even a slight misalignment or a shift of the fiber's input end for as little as 5 µm has a notable impact on the beam properties after the hollow-core fiber, including beam power, beam profile and the bandwidth of the resulting supercontinuum. Because of that an automated beam steering system is necessary in front of the hollow-core fiber to ensure a stabilized laser beam position once the adjustment of the hollow-core fiber is finished.

The actual adjustment procedure is rather tricky and mostly determined by experience about what works best in the laboratory for the respective system. The results presented in chapter 3 demonstrate that the numerical simulation is in qualitative agreement with the measurements of the experiment. Because of that it is concluded that the adjustment of the hollow-core fiber for the experiment has not introduced any perturbances in the results and is reasonable exact.

Here follows a description of the adjustment procedure as applied in the experiments presented in this work.

1. Both translation stages of the hollow-core fiber (HCF) are set to their default values to keep beam position after the HCF.

2. The power of the input laser beam is reduced to prevent damage to the HCF. Two adjustment mirrors in front of the HCF are used to shift the beam in a beam walk until transmission through the HCF is at its maximum.

3. Beam power is increased to operation value. Beam stabilization system is activated.

4. HCF is adjusted by beamwalk of front and end translation stage until transmission through the HCF is at its maximum (with round beam profile). The front stage will be moved for micrometers only, but the position of the end stage can vary about ±2 mm.

5. HCF front stage is moved to make beam profile after the HCF round and symmetric.

6. IR beam profiler camera is put into beam. HCF front stage is moved until an as good as possible compromise between a) roundness and color of visible beam profile, b) roundness of IR beam profile and c) small size of IR beam profile is achieved.

7. Two adjustment mirrors after the chirped mirror compressor are used to shift the beam in a beamwalk, to compensate for changes in HCF position and to ensure beam is in standard position defined by two irises.

8. Check quality of beam (pulse duration and shape) with SPIDER.

Step 1 and 4 are only done rarely, for example after an exchange of the hollow-core fiber or a reset of the iris apertures which are part of the prism compressor. The day to day adjustment of the hollow-core fiber starts with step 5.

However, before engaging in a thorough adjustment of the hollow-core fiber it is worthwhile to check the adjustment of the prism compressor which is part of the CPA laser amplifier. A precise alignment is important for the prism compressor to work correctly, and it has to be checked occasionally whether the beam is still located in the center of the iris apertures. It is also recommended to verify the beam path inside the compressor now and then, to ensure that the outgoing beam takes the same path as the incoming beam. A difference in paths is a strong indicator that the prism compressor is not doing its job anymore and that the compressed beam will exhibit spatial chirp, meaning the different wavelengths which are part of the pulse spectrum are not distributed homogeneously across the beam cross-section.

2.1.3. SPIDER

The main tool for pulse analysis used in the experiments for this work is a *Pulse: Four SPIDER* from *Venteon*. The abbreviation stands for **S**pectral **P**hase **I**nterferometry for **D**irect **E**lectric-field **R**econstruction. This measurement technique is based on spectral shearing interferometry and allows the retrieval of the spectral phase $\phi(\omega)$ of an ultra short laser pulse. It was first demonstrated in 1998 by the work of Iaconis and Walmsley [48].

The *Venteon* SPIDER implements spectral shearing interferometry by sending it through an ultra thin glass etalon and creating three copies of the original laser pulse. The reflections at the front and back side of the glass constitute one arm of the spider,

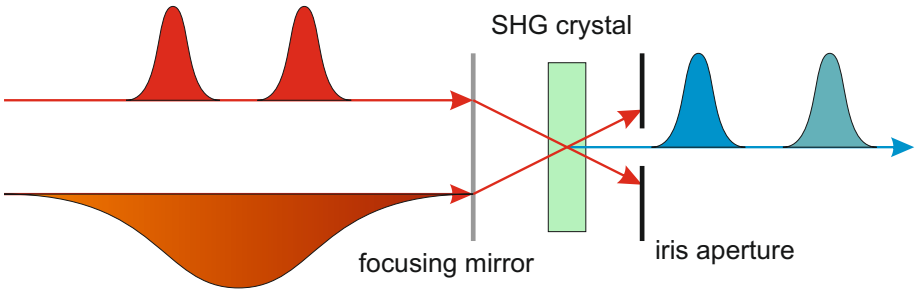

Figure 2.3.: Schematic SPIDER setup. Two pulse copies with a time delay τ are superimposed with a stretched pulse copy in an SHG crystal. The resulting up-converted pulses have a slight frequency shear due to the chirp of the stretched pulse.

with two pulse copies parted by the time delay τ determined by the thickness and material of the etalon. The other arm is the pulse transmitted through the etalon, which is then temporally stretched by about three orders of magnitude in a glass block. As illustrated in Fig. 2.3 the two SPIDER arms meet again when focused at cross direction into a type II SHG crystal. When the two short pulse copies are in superposition with the stretched pulse, two new pulses are generated with a frequency equal to the sum of the two superimposed frequency constituents. Due to the linear upchirp of the stretched pulse, the two resulting pulses will have slightly different central frequencies. This is the spectral shear Ω. Then the interference pattern between these two short pulses is measured by a spectrometer. With knowledge of the spectral shear Ω and the time delay τ the spectral phase $\phi(\omega)$ can be retrieved out of this interference pattern. The algorithm for this fast procedure was first introduced by Takeda *et al.* in 1982 [49].

The spectral interference pattern $S(\omega)$ of the two frequency-sheared pulse versions is Fourier-transformed into the time domain where it has three components, around $t = 0$ and the time delay $t = \pm\tau$. The component around $t = 0$ only contains information about the pulse's spectral amplitude, while the two sidebands also contain (identical) information about the spectral phase $\phi(\omega)$. One sideband is selected by application of a filter, and then inverse Fourier-transformed back into the frequency domain as $\phi(\omega-\Omega)-\phi(\omega)+\omega\tau$. The so called spider phase is obtained by subtracting the $\omega\tau$ term from this. The actual spectral phase is then retrieved out of the spider phase by concatenation [50].

Unfortunately this procedure fails if the interference pattern, which is modulated by the spectral amplitude of the original pulse, is too close to zero at points. At these points the extracted phase difference is undefined and the relative phase between adjacent spectral points is lost. This is generally a problem when using a SPIDER to characterize pulses which have underwent frequency generation in a hollow-core fiber. The spectrum of such pulses commonly shows strong oscillations and is prone

to have points of extreme low intensity, see Fig. 3.5 on page 64 for an example of a spectrum. This will in turn cause the existence of points of near zero intensity in the interference pattern, and at these points the retrieval algorithm might fail and the reconstructed phase will not be continuous.

The SPIDER is not able to measure the carrier-envelope phase (CEP) of the incident laser pulse. In the Taylor series expansion of the spectral phase $\phi(\omega)$ the expansion coefficients ϕ_0 and ϕ_1, respectively the CEP and the time delay of the pulse, are set equal to zero by the *Venteon* SPIDER in measurements. Because of this an arbitrary offset and an arbitrary gradient can be added to each measurement of the spectral phase $\phi(\omega)$. The actual pulse shape in the time domain or the envelope of the field $E(t)$ is not affected by this though, since it is only determined by the higher order coefficients of the Taylor expansion of the spectral phase $\phi(\omega)$. It can be reconstructed from the measured spectral phase and the spectral amplitude $|E(\omega)|$, which is measured by a spectrometer as part of the SPIDER.

2.2. Numerical simulation

One method to calculate the propagation of a light pulse through a nonlinear medium is solving the Maxwell equations according to appropriate boundary conditions. For this a second order differential equation must be solved, which is not possible to do analytically but can be done numerically with, for example, finite difference time domain (FDTD) methods [51, 52]. In 1987 Kodama and Hasegawa [53] proposed the use of a simpler version of the wave equation, based on an approach which separates an electric field into an envelope function and a fast oscillating carrier wave. This makes it possible to convert the second order differential equation into a first order equation, and solve the problem with much less computational effort than with FDTD methods. In the work of Blow and Wood [54] self-steepening was included into this approach, and Brabec and Krausz [33] extended the method 1997 to laser pulses of durations down to a single cycle of the carrier wave.

Since then this method has become standard and it has been used in many publications to study the propagation of few-cycle pulses in a nonlinear medium, as for example for the effects of self-phase modulation and induced-phase modulation in optical fibers [29], for effects close to the zero dispersion wavelength in optical fibers [55], for self-focusing and critical power in hollow waveguides [56], for a cascading hollow-core fiber arrangement [16], for a frequency-dependent effective mode area in a photonic crystal fiber [27], for modelling sub-cycle dynamics [57], or for hollow-core fibers with a temperature gradient [58] to name some applications.

In this section the method and the model used for numerical calculations of the nonlinear process in a hollow-core fiber in this work is presented. First the split-step method is introduced in section 2.2.1. The two operators which are implemented by this method, the nonlinear operator $\hat{N}$ and the dispersion operator $\hat{D}$, are discussed

in that section, as well as any approximations and assumptions made in the model. In section 2.2.2 the results of the calculations are compared with those of previous works to inspect the validity of the model. Finally in section 2.2.3 the two driving forces of the nonlinear process, self-phase modulation and self-steepening, are studied with the help of numerical calculations.

All calculations have been programmed in LabVIEW 8.6, see appendix A.

Throughout this work simulation parameters are listed in the figure captions. The default parameters are those used in the experiment: input spectral amplitude and phase as in experiment (Fig. 3.4, PrismComp0), $\omega_0 = 2.365\,\mathrm{PHz}$, $E = 830\,\mu\mathrm{J}$ per pulse; hollow-core fiber length $z = 1\,\mathrm{m}$, bore radius $a = 125\,\mu\mathrm{m}$, filled with neon gas at $p = 3\,\mathrm{bar}$. Parameters which are consistently not changed, like central frequency ω_0, pulse energy E, fiber length z, fiber bore radius a or gas type, are usually omitted.

The carrier or central frequency of the input pulses measured in the experiment is also used for pulses with a Gaussian spectrum. It corresponds to a central wavelength of 797 nm.

2.2.1. Split-step method

The split-step method is a numerical method especially used to calculate the solution of nonlinear partial differential equations like the nonlinear Schroedinger equation [22, p. 41-45]. Its name stems from the fact that it splits the calculation into small steps in which the linear and nonlinear parts of the equation are computed independent of each other.

In section 1.3.4 the 1-dimensional pulse propagation equation was obtained in the form of Eq. (1.62)

$$\frac{\partial A}{\partial z} = -i\frac{1}{2}\beta_2\frac{\partial^2 A}{\partial T^2} + \frac{1}{6}\beta_3\frac{\partial^3 A}{\partial T^3} - \frac{\alpha}{2}A + i\gamma_0|A|^2A - \frac{\gamma_0}{\omega_0}\frac{\partial}{\partial T}(|A|^2A).$$

If a dispersion operator $\hat{D}$ and a nonlinear operator $\hat{N}$ are defined as

$$\hat{D} = -i\frac{1}{2}\beta_2\frac{\partial^2}{\partial T^2} + \frac{1}{6}\beta_3\frac{\partial^3}{\partial T^3} - \frac{\alpha}{2} \tag{2.1}$$

$$\hat{N} = i\gamma_0\left(|A|^2 + i\frac{1}{\omega_0 A}\frac{\partial}{\partial T}(|A|^2A)\right) \tag{2.2}$$

Eq. (1.62) from above can be written as

$$\frac{\partial A}{\partial z} = (\hat{D} + \hat{N})A, \tag{2.3}$$

which can be solved with $A(z) = A_0 e^{(\hat{D}+\hat{N})z}$.

In the split-step Fourier method it is assumed that the operators $\hat{D}$ and $\hat{N}$ can be handled as acting on the pulse independent of each other for small distances h, which results in [22, p. 42]

$$A(z+h,T) \simeq A(z,T)e^{\hat{D}h}e^{\hat{N}h}. \tag{2.4}$$

First, the dispersion $\hat{D}$ acts on the pulse along the length of h, and then the nonlinearity $\hat{N}$ acts on the modified pulse for the same length, or the other way round. Then the dispersion $\hat{D}$ acts again during the next small step h, followed by $\hat{N}$, and this is repeated until the end of the fiber is reached.

The main benefit of this procedure is that it allows for a simple calculation of $e^{\hat{D}h}A$ by Fourier-transforming this expression and replacing $\partial/\partial T$ with $-i\omega$. This way $\hat{D}$ is just a number in the frequency domain and the product is resolved by multiplying A with a spectral phase. The result is then transformed back into the time domain with an inverse Fourier-transformation to obtain the new $A(z+h,T)$.

The same trick is not useful for $\hat{N}$. The nonlinear operator still has to be applied in the time and not the frequency domain since the term $|A|^2$ contains the temporal envelope $A(T)$, normalized such that the square of its absolute value is equal to the instantaneous power $P(T)$, a quantity which cannot be obtained in the frequency domain. As a consequence the two operators $\hat{D}$ and $\hat{N}$ have to be applied in their respective domains in two separate steps, which is the reason for the name of the method.

However, the operators $\hat{D}$ and $\hat{N}$ do not commutate [22, p. 42] and hence $e^{\hat{D}+\hat{N}} \neq e^{\hat{D}}e^{\hat{N}}$. Eq. (2.4) is only valid as approximation for small step sizes h. To estimate the error which is caused by this, the order in which the operators $\hat{D}$ and $\hat{N}$ act on A at each step h can be reversed, and the result compared to the result of the calculation without reversal of the order in which the operators act. For $h = 5\,\mathrm{mm}$ it is found that the results are in very good agreement. The difference in frequency bandwidth between two calculations with a different order of operators is equivalent to a difference in the Fourier-transform limited pulse duration of $\Delta\tau_0 = 0.002\,\mathrm{fs}$, which is more accurate than the listed decimal of any result presented in this work. At $h = 5\,\mathrm{mm}$ the step size is chosen sufficiently small to allow treating $\hat{N}$ and $\hat{D}$ as if they would indeed commutate.

Nonlinear operator $\hat{N}$

The Nonlinear operator $\hat{N}$ of Eq. (2.2)

$$\hat{N} = i\gamma_0 \left(|A|^2 + i\frac{1}{\omega_0 A}\frac{\partial}{\partial T}(|A|^2 A) \right)$$

consists of the term for SPM, which is the first term on the right-hand side and the source of the new frequencies created in the hollow-core fiber, and the term for self-steepening, which is the second term on the right-hand side and results in a

modification of the pulse shape. The self-steepening term is obtained by considering the dependency of the nonlinear parameter γ on the frequency ω in first order and neglecting the derivatives $\partial n_2/\partial\omega$ and $\partial A_{\text{eff}}/\partial\omega$, as seen in Eq. (1.61). Both terms scale with γ_0, which is defined in Eq. (1.34) as

$$\gamma_0 = \gamma(\omega_0) = \frac{n_2(\omega_0)\omega_0}{cA_{\text{eff}}(\omega_0)}. \tag{2.5}$$

The quantities which need to be determined are $n_2(\omega_0)$ and $A_{\text{eff}}(\omega_0)$.

The nonlinear refractive index of neon is $n_2(p) = \frac{p}{1\,\text{bar}}\, 9.4 \cdot 10^{-25}\,\text{m}^2/\text{W}$ at a wavelength of 800 nm [32].

The effective mode area of a hollow-core fiber is $A_{\text{eff}} \simeq 0.48\pi a^2$, where a is the radius of the fiber bore [8, 16].

Dispersion operator $\hat{D}$

The dispersion operator $\hat{D}$ of Eq. (2.1)

$$\hat{D} = -i\frac{1}{2}\beta_2\frac{\partial^2}{\partial T^2} + \frac{1}{6}\beta_3\frac{\partial^3}{\partial T^3} - \frac{\alpha}{2}$$

consists of terms for the dispersion parameters GDD and TOD and a term for attenuation. Unlike the $\hat{N}$ operator, the dispersion operator $\hat{D}$ is not applied directly to $A(z,t)$ in the calculation. Instead it is Fourier-transformed along with $A(z,t)$ and then applied in the frequency domain, before the result is inverse Fourier-transformed back into the time domain. In the frequency domain Eq. (2.1) looks like

$$\hat{D} = i\frac{\omega^2}{2}\beta_2 + i\frac{\omega^3}{6}\beta_3 - \frac{\alpha}{2}. \tag{2.6}$$

Terms for higher orders of dispersion can be added to Eq. (2.6) at leisure, however it is not necessary to do so in the case of a hollow-core fiber filled with neon. This can be shown by calculating the coefficients β_i, for which it is first necessary to know the dependency on the wavelength of the refractive index of neon. This can be obtained from [21]

$$n - 1 = 0.012055\left(\frac{0.1063\,\lambda^2}{184.661\,\lambda^2 - 1\cdot 10^{12}\,\text{m}^2} + \frac{1.829\,\lambda^2}{376.84\,\lambda^2 - 1\cdot 10^{12}\,\text{m}^2}\right), \tag{2.7}$$

for a temperature $T = 273\,\text{K}$ and a pressure $p = 1\,\text{bar}$. The coefficients β_i of the propagation constant can be calculated with Eq. (1.30) as $\beta_j = \partial^j\beta/\partial\omega^j\big|_{\omega_0}$. The results for β_2, β_3 and β_4 are illustrated in the left-hand side of Fig. 2.4. The 4th order coefficient β_4 and its gradient are nearly equal to zero, so β_4 and all higher dispersion coefficients can be neglected for neon.

The same can be determined by applying the different terms of dispersion to the numerical calculation. For an input pulse as measured in the experiment and shown

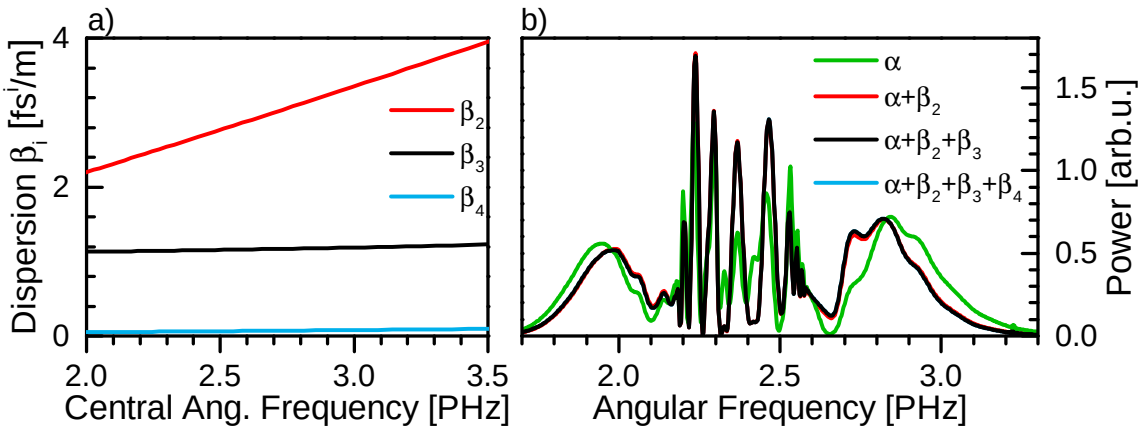

Figure 2.4.: In a) Phase constants β_2 to β_4 of neon gas at temperature $T = 273\,\mathrm{K}$ and pressure $p = 1\,\mathrm{bar}$ are shown, calculated according to [21]. In b) numerically calculated spectra after the HCF are shown, considering dispersion terms up to the given order. The spectrum including a β_4 term is already indistinguishable from the spectrum including only up to a β_3 term - it lies beneath it and is invisible.
(Parameters: input spectral amplitude and phase as in experiment (Fig. 3.4, PrismComp0); HCF $p = 3\,\mathrm{bar}$)

in section 3.2 the results are illustrated in the right-hand side of Fig. 2.4. It is apparent that inclusion of the GDD term has a notable effect on the calculated spectral amplitude. The additional inclusion of the TOD term changes the calculated spectrum only in minor details, while the calculated spectrum including the 4th order term is not even visible anymore - at the resolution of the figure it is identical with the spectrum lacking a 4th order term. Calculations show that inclusion of the 4th order term changes the Fourier-transform limited pulse duration τ_0 of the spectrum only by $2 \cdot 10^{-4}\,\mathrm{fs}$, and it can hence be disregarded.

The pressure-dependency of the coefficients β_j can easily be accounted for with Eq. (1.39) on page 16, by calculating $\beta_j(p_0)$ with the help of Eq. (2.7) and multiplying the result with $\frac{p}{1bar}$.

Attenuation and input coupling

The dispersion operator $\hat{D}$ does not only consist of the respective dispersion terms and includes also the absorption loss coefficient α. Since beam power is measured in front of the hollow-core fiber, α consists in practice of two different parts, respectively the attenuation losses occurring while the beam is propagating along the length of the fiber, and the coupling losses occurring at input coupling at the start of the fiber. The beam also passes two thin fused silica windows on its way in and out of the

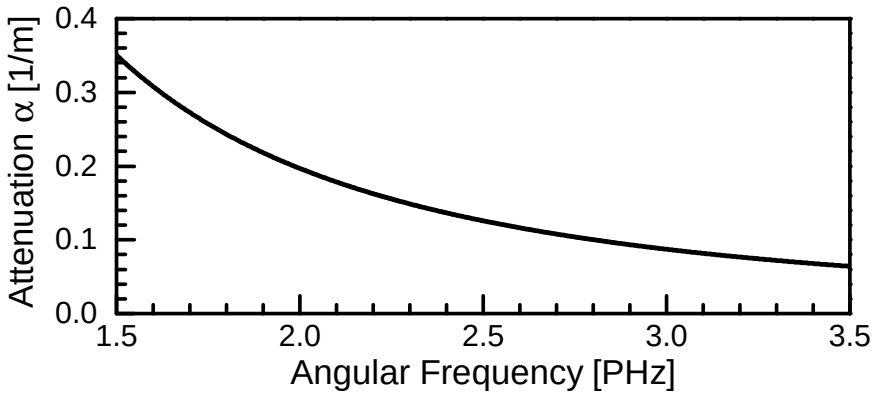

Figure 2.5.: The attenuation coefficient α for a fused silica HCF with bore radius $a = 125\,\mu\text{m}$, calculated according to Eq. (2.8). Attenuation is notable higher for low frequencies.

pressure chamber which contains the hollow-core fiber and the neon gas, but these are aligned in the Brewster angle in regard to the beam's linear polarization and hence can be ignored. Measurements in front of and behind the hollow-core fiber show that the total loss to power is usually very close to 34%. This does not account for any additional loss incurred by a pair of fused silica wedges often positioned shortly after the hollow fiber for dispersion control, which in our setup cause another 12 to 13% loss of power.

In a common solid optical fiber the refractive index of the cladding is lower than in the core and the beam stays inside the core due to total internal reflection, incurring a minimum of absorption losses along the length of the fiber. For a gas-filled hollow-core fiber this is obviously not the case and the beam will suffer reflection losses along its way through the fiber. The angle of incidence is very small though, so losses are expected to be low. This has already been studied in the 1960's by Marcatili and Schmeltzer [59, p. 14] and the so called attenuation loss depends on the wavelength, the bore radius a and the refractive index n_{cl} of the fiber cladding, fused silica in our case, as follows

$$\alpha = \frac{(2.405)^2 c^2}{\omega^2 a^3} \frac{n_{\text{cl}}^2(\omega) + 1}{\sqrt{n_{\text{cl}}^2(\omega) - 1}}. \tag{2.8}$$

The attenuation loss coefficient α is plotted in Fig. 2.5.

Light propagating in a fiber will do so in specific states called fiber modes, which describe the transversal distribution of the electric field. Since this work is based on a 1-dimensional solution of the wave propagation equation I will not go into detail concerning fiber modes, and instead refer to the existing literature as for example [22, 59]. The factor 2.405 in Eq. (2.8) is a constant depending on the fiber mode, for example, and the particular value given here belongs to the fundamental mode HE_{11}.

When a beam with a $1/e^2$ waist radius of more than 60% of the bore radius is coupled into a hollow waveguide, nearly all of the the beam's energy is deposited in the fundamental mode HE_{11} [60] and remains there during propagation [31]. Coupling into the fundamental mode is optimal ($\simeq$ 98% of the total power) when the beam waist radius is 64% of the bore radius a, but remains high ($> 80\%$) for values greater than that until the beam waist is larger than the bore. In our setup the beam waist radius is at 80% of the bore radius, which results in a coupling of about 90% into the fundamental mode [60]. While this might be less than optimal, it causes the undesirable higher fiber modes to be suppressed even stronger. Since it is energy deposited in those higher fiber modes which causes self-focusing and the ensuing deterioration of the beam profile at critical powers [61, p. 557], an increase of power in the higher fiber modes is to be avoided.

The loss occurring by coupling the beam into the fiber is experimentally estimated by taking the measured total loss of 34% of the beam's power and subtracting the loss caused by attenuation in the fiber. This results in an input coupling loss of 24%. This is high considering that input coupling losses are expected to be only about 10%. Either the properties of the fiber front make for a less than ideal input coupling, or additional losses occur inside the hollow fiber. For example, a fiber which is not perfectly straight can induce considerable additonal losses [59, p. 24].

When using beam powers which approach the critical power for self-focusing of Eq. (1.52), the attenuation coefficient also needs to account for ionization effects. Since we stay safely below this threshold, see section 1.3.2, ionization effects are not considered in this work.

General remarks

The calculations were done using a positive ω axis of 4096 points ranging from 0 Hz to slightly over $1 \cdot 10^{16}$ Hz or 10 PHz, with a step size of $\Delta\omega = 2.5 \cdot 10^{12}$ Hz. The time axis accordingly has 8192 points with a step size of $\Delta t \simeq 0.307$ fs, ranging across ± 1.25 ps. At a period of 2.67 fs this translates into slightly less than nine points per oscillation. A further decrease of $\Delta\omega$ or Δt with an according increase in the number of points brought no change in the calculation results.

The interaction step length h for the split-step method is chosen as $h = 5$ mm. While very similar results can already be obtained with step lengths as large as $h = 5$ cm, the simulation proves to be unstable at this length, showing critical effects and apparent beam collapse due to self-steepening when in fact it did not show this behavior under otherwise identical settings except for a shorter length of h. To avoid such artifacts in the simulation, the step size was reduced until the simulation ran stable.

At a length of $h = 5$ mm a single run of the LabVIEW calculation takes about seven seconds, and a run with 60 different values for pressure ($\Delta p = 0.05$ bar) takes slightly over six minutes.

2.2.2. Comparison with literature

In this section the results of two publications which treat numerical simulations of pulse propagation in a hollow-core fiber are compared with the results of the numerical calculation presented in this work. This is done to ensure that the model has been adapted correctly and performs well in comparison to other models. First a publication from 2010 is presented, which investigates an interesting observation about self-steepening which is in agreement with results of the numerical calculations presented in section 2.2.3. Further a comparison with the results of a publication from 2003 is done, which studies the differences between a 1-dimensional and a 3-dimensional model.

Bejot *et al.* - Mechanism of hollow-core-fiber infrared-supercontinuum compression with bulk material

In their paper from 2010 Bejot *et al.* [46] investigate, both by numerical calculation and experiment, a supercontinuum created in the infrared around 1.8 µm instead of the more commonly used central wavelength of 800 nm provided by a Ti:sapphire laser amplifier. One of the advantages of this spectral regime is that fused silica exhibits anomalous dispersion at these wavelengths and induces negative GDD in light pulses propagating through it. By utilizing a simple fused silica plate of 3 mm thickness after the hollow-core fiber as a compressor instead of a chirped mirror setup, Bejot *et al.* demonstrate the compression of infrared light pulses to less than 12 fs, which is below two cycles of the carrier frequency. They also comment on the presence of unexpected negative third-order-dispersion (TOD) in the pulses, which has to be generated during propagation through the hollow-core fiber, and identify self-steepening as the cause of this TOD.

Fig. 2.6 shows simulations done by Bejot *et al.* in which the spectral amplitude is calculated in dependence on the distance z propagated in the hollow-core fiber, with an input beam which is assumed to have a spectral phase $\phi(\omega)$ equal to zero. On the left-hand side is a symmetric spectrum without inclusion of the self-steepening term in the calculation, and on the right-hand side a spectrum including the self-steepening term and demonstrating the corresponding asymmetry. In the bottom row simulations done with the numerical calculation presented in this chapter are shown, after adapting the calculation to the set of parameters used by Bejot *et al.*. This includes an input beam with a pulse duration of 73 fs instead of 32 fs, with a spectral phase $\phi(\omega)$ equal to zero, a carrier frequency of $\omega_0 = 1.03\,\mathrm{PHz}$, and an energy of $E = 930\,\mu\mathrm{J}$ per pulse. The hollow-core fiber has an inner bore radius of $a = 200\,\mu\mathrm{m}$ instead of $a = 125\,\mu\mathrm{m}$ and the same length $z = 1\,\mathrm{m}$. It is filled with argon instead of neon, at a pressure $p = 1.4\,\mathrm{bar}$.

Bejot *et al.* use a 1-dimensional pulse propagation equation nearly identical to Eq. (1.62). However, the optical Kerr effect is not only considered as a $\chi^{(3)}$ effect, but includes the contribution of higher nonlinear terms up to $\chi^{(11)}$. This is made possible

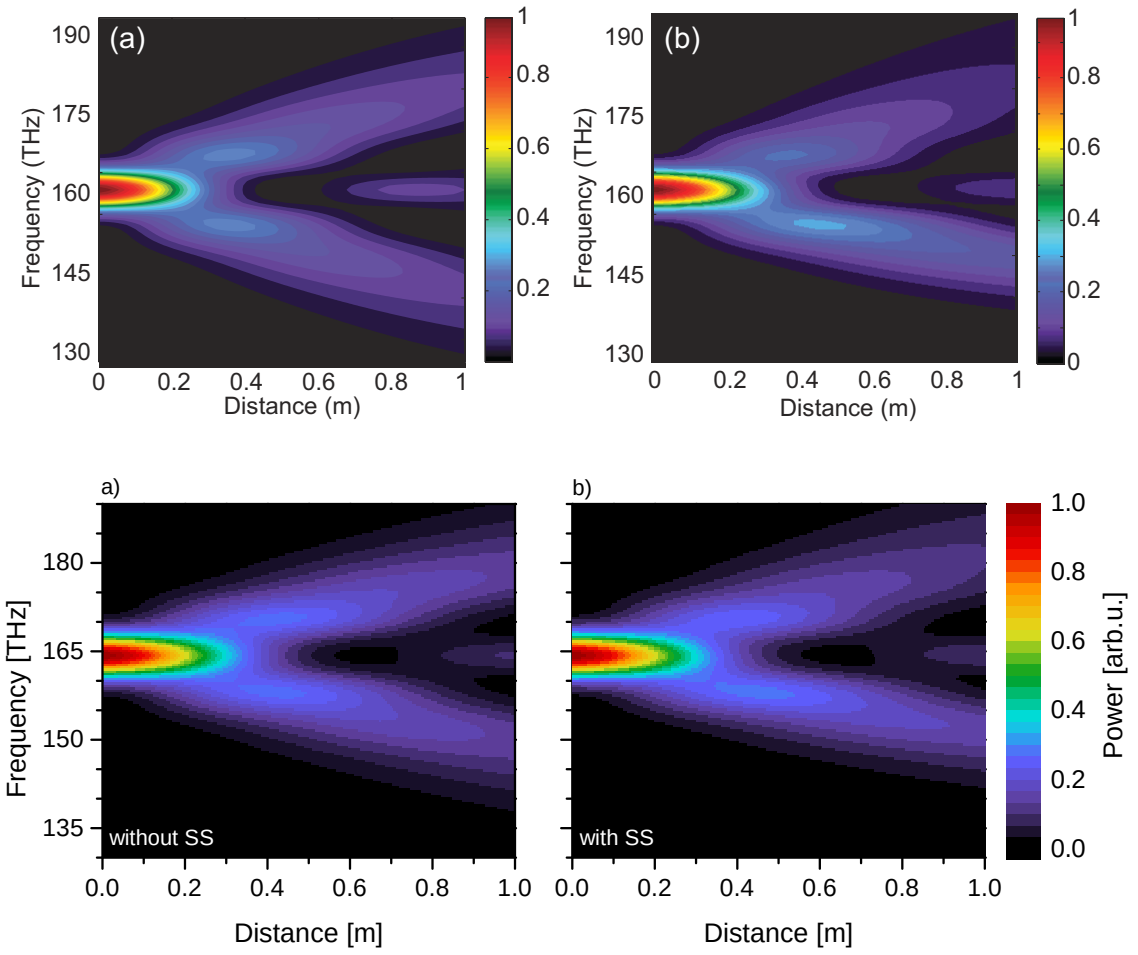

Figure 2.6.: Calculated spectra after the HCF in dependence on the distance z propagated in the hollow-core fiber. On the left-hand side without and on the right-hand side with the self-steepening term. The top row shows simulations done by Bejot *et al.* [46], while the bottom row shows simulation results calculated in this work but with identical parameters as used by Bejot *et al.*.
(Parameters: input Gaussian pulse $\tau_0 = 73\,\mathrm{fs}$, $\omega_0 = 1.03\,\mathrm{PHz}$, $E = 930\,\mu\mathrm{J}$ per pulse; hollow-core fiber argon gas, $p = 1.4\,\mathrm{bar}$, $a = 200\,\mu\mathrm{m}$.)

by publications investigating the higher order refraction indices n_{2m} for argon and other constitutents of air [62], but not for neon. For a central wavelength of 800 nm the contribution of higher order terms for the optical Kerr effect is reported to have only a negligible effect on simulations though [23], gaining importance only in the blue and UV regimes.

The absorption coefficient α used by Bejot *et al.* is determined differently than in section 2.2.1, where it is handled by separation into two parts, losses occuring at input coupling into the hollow-core fiber and losses due to attenuation caused by grazing incidence reflections inside the hollow fiber bore. Unfortunately Bejot *et al.* do not state exactly how they determine the absorption coefficient α.

They also do not comment on the effective mode area A_{eff} and how it is obtained.

Despite these differences it is observable in Fig. 2.6 that the two sets of simulations are in good agreement with each other. The features in the simulation from Bejot *et al.* are slightly shifted to shorter propagation distances in the hollow-core fiber, which implies that the nonlinear process is handled as working a bit more efficient than in this thesis. A likely explanation for this is a small decrease of either the attenuation coefficient α or the effective mode area A_{eff}.

Nurhuda *et al.* - Propagation dynamics of femtosecond laser pulses in a hollow fiber filled with argon: constant gas pressure versus differential gas pressure

In their paper from 2003 Nurhuda *et al.* [30] investigate the advantages of a differential gas pressure inside the hollow-core fiber instead of a constant pressure setup like it is used in this work. For this they adapt a 3-dimensional model for the numerical calculations and compare it to the results of a 1-dimensional model, and demonstrate that the two different approaches arrive at the same results as long as the laser power stays below the critical value for self-focusing (see the start of section 1.3.2). Above the critical value self-focusing leads to critical deformation of the transversal electric field or the modal distribution of the pulse, and the assumption of the 1-dimensional model that the transverse modal distribution $F(x, y)$ remains unchanged does not hold anymore.

Fig. 2.7 shows on the left-hand side calculations taken from [30] with low pulse powers in which the 1-dimensional and 3-dimensional models are compared to each other, and it is demonstrated that they arrive at the same results with the chosen parameters. On the right-hand side a simulation performed with the numerical calculation presented in this work is shown, using the same parameters as the simulation of Nurhuda *et al.*. The spectral phase and the bandwidth and general form of the calculated spectral amplitude is comparable to that on the left-hand side, even if the peak ratio is reversed. This might be due to different transformations from the frequency into the wavelength domain. To visualize this the change of domain in the right hand side graph is performed both with and without the required Jacobi transformation of the spectral amplitude, and it is observable that the spectrum attained without Jacobi transformation looks very similar to that presented by Nurhuda *et al.*.

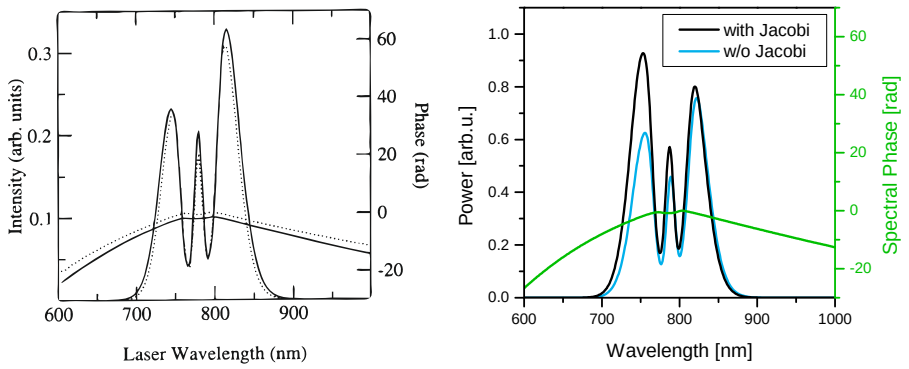

Figure 2.7.: Left-hand side: Comparison between calculated spectrum and phase after the HCF with a 1-dimensional (dotted line) and a 3-dimensional model (solid line) for a laser power below the critical power for ionization, taken from Nurhuda *et al.* [30]. Right-hand side: results of calculations performed for this thesis with identical parameters as used by Nurhuda *et al.*, once with Jacobi-transformation into the wavelength domain (black) and once without (blue).
(Parameters: input Gaussian pulse $\tau_0 = 60\,\mathrm{fs}$, $\omega_0 = 2.39\,\mathrm{PHz}$, $E = 100\,\mu\mathrm{J}$ per pulse; HCF argon gas, $p = 2\,\mathrm{bar}$, $a = 125\,\mu\mathrm{m}$.)

Nurhuda *et al.* apply a laser peak power in their calculations for low pulse powers which is equal to 0.32 $P_{\mathrm{crit,hcf}}$ for argon. In the experiments described in the next chapter we remain below 0.25 $P_{\mathrm{crit,hcf}}$ for neon. Hence it can be safely assumed that the result of Nurhuda *et al.*, that the 1-dimensional model is equivalent to a full 3-dimensional model for low laser powers, also holds true for the calculations done in this thesis. This means that the laser power is so low that self-focusing is not strong enough yet to lead to critical deformations of the beam profile and that the form of the transverse modal distribution $F(x, y)$ can be considered as constant during beam propagation in the hollow-core fiber.

2.2.3. Self-phase modulation and self-steepening

In this section numerical calculations are used to examine the effect of the self-phase modulation and self-steepening terms in Eq. (1.62). This establishes a better understanding of the features of spectral amplitude and phase in more depth than in the introduction presented in section 1.4, and will also demonstrate that self-steepening is responsible for the generation of negative third order dispersion (TOD) during propagation through the hollow-core fiber.

Fig. 2.8 illustrates how the spectral amplitude, group delay and instantaneous power, or temporal shape, of an unchirped input pulse change after propagation

through the gas-filled hollow-core fiber in dependence on the terms for self-phase modulation (SPM), dispersion and self-steepening in Eq. (1.62).

For the case considering only SPM, Fig. 2.8 shows the same graphs as Fig. 1.2 on page 23. It is already discussed in section 1.4 that SPM is responsible for the symmetric peaks in the spectral amplitude. The temporal pulse shape is not changed by SPM, which acts only on the temporal phase of the pulse in the time domain and not on the envelope. The group delay, the first derivative of the spectral phase $\phi(\omega)$, shows sharp peaks located in the minima of the spectral amplitude. Upward peaks or maxima for frequencies below the carrier frequency ω_0 and downward peaks or minima for frequencies greater than ω_0. The linear distribution of $\mathcal{W}(t, \omega)$ in the Wigner plot suggests that the pulse exhibits mostly group delay dispersion (GDD), see Fig. 1.4 on page 28.

If absorption and dispersion are added to the calculation an obvious decrease in the instantaneous power $P(t)$ occurs, which is mainly due to the losses of about 24% at coupling into the hollow-core fiber. The temporal shape also becomes broader because of dispersion and a slight frequency-dependence of the absorption during propagation through the hollow-core fiber. Due to the decrease in power the generation of new frequencies works less efficiently and in the spectral amplitude is one peak less than without dispersion and absorption, and the bandwidth is slightly reduced. Dispersion causes an additional gradient in the group delay, which is also observable in the Wigner plot as an increase of GDD.

In contrast to SPM self-steepening only acts on the envelope and not on the temporal phase in the time domain. It is caused by the frequency-dependency of the nonlinear process and expresses itself in the last term of Eq. (1.62). Since the self-steepening term scales with the derivative of the intensity its effect is strongest at times t when the pulse intensity rises or falls. Due to the term's minus sign it will decrease intensity and broaden the pulse slope when the pulse is rising, and increase intensity and steepen the pulse slope when intensity is falling. The result is the shifting of the pulse's centrum back towards the trailing edge of the pulse, which is already discussed in section 1.4.3 and is also visible in Fig. 2.8 b).

Self-steepening causes an increase of the intensity gradient at the pulse's trailing edge where, as has been shown in section 1.4.1, SPM generates the new frequencies which are higher than the carrier frequency ω_0. Since the efficiency of SPM scales with the gradient of intensity, the high frequencies originating at the pulse's trailing edge are generated with a greater bandwidth $\Delta\omega$ than the low frequencies originating at the pulse's rising edge. The peak areas remain the same though since low frequency peaks in the spectral amplitude are high and have a small bandwidth, while high frequency peaks are low and have a great bandwidth. This effect is illustrated in Fig. 2.8 a). The central frequency of the spectral amplitude shifts to higher frequencies during propagation in the hollow-core fiber under influence of self-steepening.

It is discernable in the Wigner plot that $\mathcal{W}(t, \omega)$ has acquired a slight bend to the left with the inclusion of self-steepening in the calculations. This is an indication of

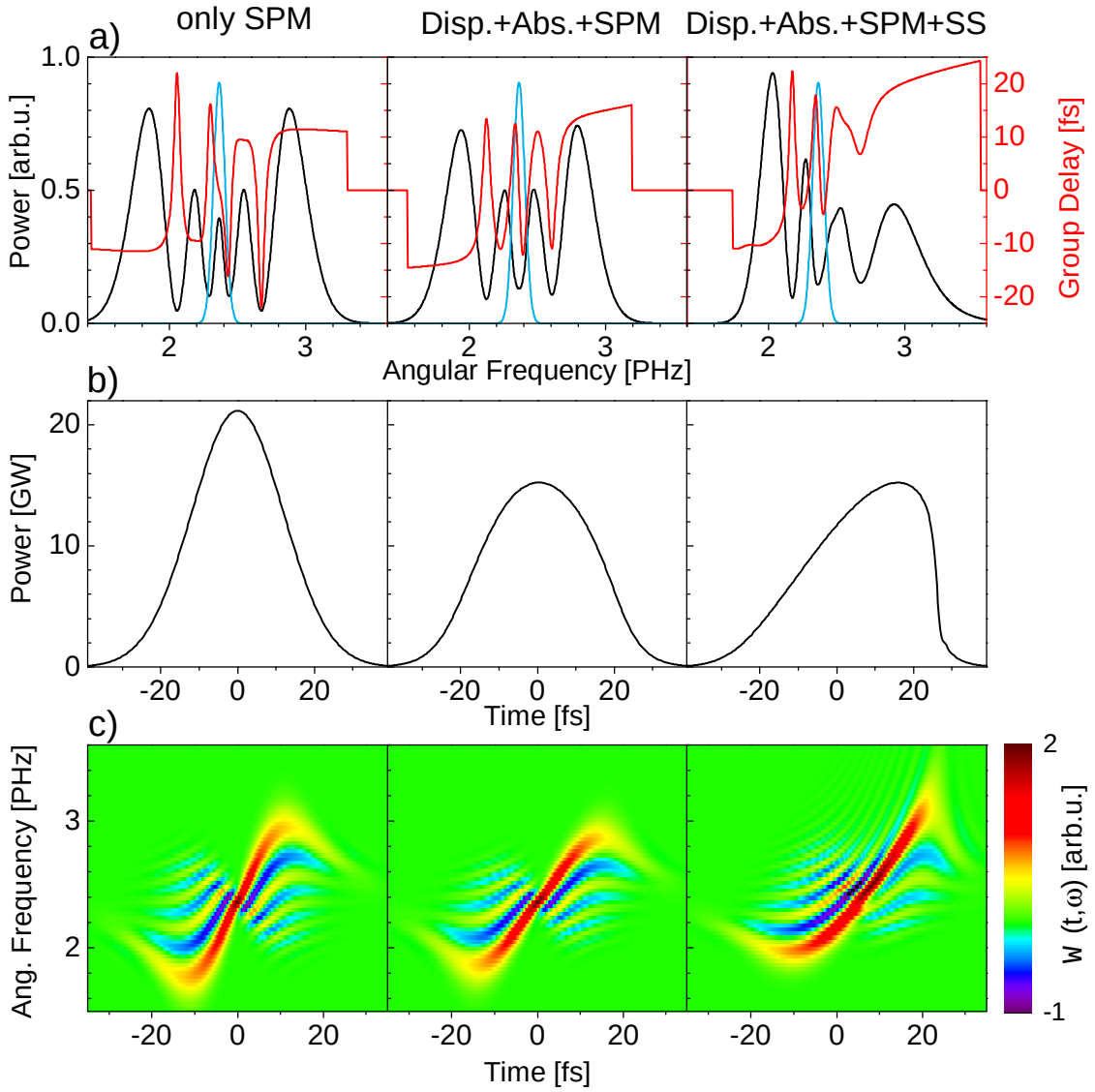

Figure 2.8.: Calculations for a Gaussian beam with SPM only, with dispersion and SPM (but no SS), and with dispersion, SPM and SS. In a) spectrum $P(\omega)$ (black) and group delay (red) after HCF, and spectrum $P(\omega)$ in front of HCF (blue) divided by 5. In b) the instantaneous power $P(t)$ after the HCF, and in c) the Wigner plots.
(Parameters: input Gaussian pulse $\tau_0 = 28\,\mathrm{fs}$, $\phi(\omega) = 0$; HCF $p = 2\,\mathrm{bar}$)

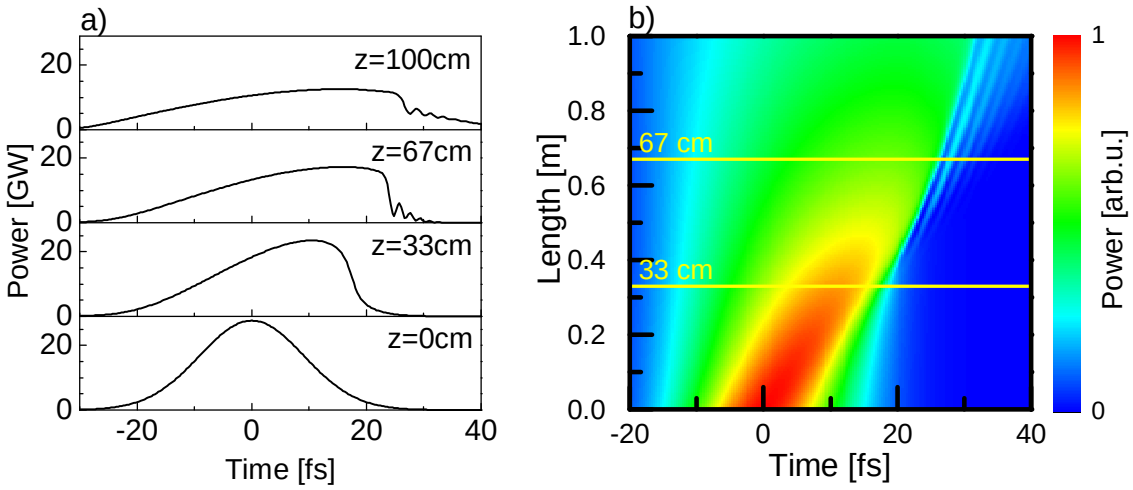

Figure 2.9.: Example of pulse collapse induced by the self-steepening term. Right-hand side is the evolution of the temporal pulse shape $|A(z,t)|^2$ along the fiber length z. The yellow lines mark the positions of line scans depicted on the left-hand side. The pulse's trailing edge starts to break up at about $z = 40\,\mathrm{cm}$.
(Parameters: input Gaussian pulse $\tau_0 = 21.2\,\mathrm{fs}$, $\phi(\omega) = 0$; HCF $p = 3\,\mathrm{bar}$)

the presence of negative third order dispersion (TOD) in the pulse, a result that is discussed in more detail in the section after the next, at the end of this chapter.

Pulse collapse

Ultrashort pulse propagation models can exhibit two distinct types of singularities, self-focusing collapse and self-steepening induced shock [63]. In the case of self-focusing collapse the Kerr lens induced by the nonlinear change of the refractive index continues to focus the beam until it eventually approaches a singularity and collapse occurs, at least in simulations. Physically this process is arrested by mechanisms like multiphoton ionization or pulse splitting [64]. But even without collapse this effect will lead to deformation of the pulse's transversal field and modal distribution if the input laser pulse exceeds a critical power [31]. This threshold is adressed by the critical power $P_{\mathrm{crit,hcf}}$ introduced in Eq. 1.52 on page 18.

Another kind of pulse collapse is caused by self-steepening shock. Self-steepening causes an increase and steepening of intensity in the pulse's trailing edge, which can ultimately lead to shock creation when the gradient of the temporal envelope becomes infinte [65]. Physically this process is slowed down or even arrested by a decrease of intensity through absorption or by broadening of the pulse by dispersion. In the simulations in this thesis, which include both absorption and dispersion, this

kind of collapse can still be observed as the trailing edge of the pulse becomes nearly vertical and then intensity 'spills over' and generates afterpulses. This is exemplary depicted in Fig. 2.9. In calculations done with parameters similar to those of the experiment this self-steepening shock usually sets in when the Fourier-transform limited duration τ_0 of the pulse falls below 3 fs and approaches the duration of just one oscillation. We have not yet investigated how a laser pulse behaves in the experiment when the calculation yields that the pulse is at the onset of self-steepening collapse, and currently it is assumed that visible onset of collapse means that the numerical calculations cease to be an accurate description of the experiment.

Prepulses

The purpose of the supercontinuum generated in our setup is to provide sufficient frequency bandwidth for the pulse to enable compression down into the few-cycle regime. In the experiment an arrangement of chirped mirrors and a pair of fused silica wedges are used for the actual pulse compression. In the simulation an arbitrary amount of dispersion can be added to the pulse after the numerical calculation of the nonlinear processes in the hollow-core fiber to make the pulse as short as possible in the time domain. To stay inside the parameters which are possible to control in the experiment with standard commercial chirped mirrors, only group delay dispersion (GDD) and third order dispersion (TOD) are considered for this adjustment of the spectral phase.

When only GDD is applied to the pulse in the simulation for compression, it becomes obvious that also a notable component of TOD is generated during pulse propagation in the hollow-core fiber. This is not the case for calculations which only consider self-phase modulation (SPM). As soon as the self-steepening term is included however, the indications of TOD are observable both in the temporal pulse shape and the respective Wigner plots, as is illustrated in Fig. 2.10.

SPM causes strong oscillations in the spectral phase and the group delay. Because of that it is not straightforward to calculate the exact amount of GDD and TOD necessary to compensate that dispersion and make the pulse as short as possible. Hence it is easiest to not calculate the required amounts of GDD and TOD, but to vary them as parameters in the simulation until the pulse is as short as possible in the time domain. This can be done with an uncertainty of $\pm 1\,\mathrm{fs}^2$ for GDD and $\pm 1\,\mathrm{fs}^3$ for TOD.

For a bandwidth-limited Gaussian input pulse with a duration of 28 fs, a neon gas pressure in the hollow-core fiber of 2 bar and otherwise using standard experiment settings ($E = 830\,\mu\mathrm{J}$ per pulse, HCF $z = 1\,\mathrm{m}$, $a = 125\,\mu\mathrm{m}$), this results in adding $-21\,\mathrm{fs}^2$ GDD and $+15\,\mathrm{fs}^3$ TOD to make the pulse as short as possible. If the pulse would be measured directly after exit from the hollow-core fiber, without any additional dispersion from propagation through neon, air, the fused silica of the pressure chamber window, or any other medium.

In Fig. 2.10 the presence of TOD in the pulse after propagation through the hollow-core fiber and its connection to the self-steepening term is demonstrated. It is apparent that in simulations only considering SPM and not self-steepening, the pulse after the hollow-core fiber can be compressed nearly down to its Fourier-transform limited (FTL) duration just by application of negative GDD. While in simulations including both SPM and self-steepening also the application of additional positive TOD is required, and sufficient, to compress the pulse nearly down to its FTL duration. The influence of higher coefficients of the Taylor series of the spectral phase is negligible for pulse compression in the simulations.

In graph a) the temporal pulse shapes for three different cases are illustrated. The black plot represents a calculation done without the self-steepening term, with $-21\,\mathrm{fs}^2$ GDD added for compression after the hollow-core fiber. The pulse shape is strictly symmetric with only minor side peaks. The corresponding Wigner plot in graph b) shows that $\mathcal{W}(t,\omega)$ is concentrated in a vertical line around $t = 0$, an indication that its spectral phase is about zero and its pulse duration is nearly bandwidth-limited.

The red plot in Fig. 2.10 a) represents a calculation including the self-steepening term, which otherwise has the same parameters as the black plot. The series of prepulses signify notable negative TOD. The same information can be gathered from the corresponding Wigner plot in graph c). $\mathcal{W}(t,\omega)$ shows a curvature to the left-hand side which is characteristic for negative TOD, as can be seen in Fig. 1.4 on page 28.

The green plot demonstrates that this negative TOD can be compensated with the application of $+15\,\mathrm{fs}^3$ TOD. Now the temporal pulse shape is nearly symmetric again and its peak is even narrower than before for the black plot. That illustrates that self-steepening makes the process for generating new frequencies more efficient, causing the spectral amplitude to be broader and hence the compressed pulse to be shorter.

Many textbooks and works about frequency generation consider only SPM in their predictions, because this way the pulse propagation equation can be solved analytically when dispersion is also neglected . The observation that self-steepening causes the generation of negative TOD during propagation through a hollow-core fiber in addition to the anticipated positive GDD generated by SPM is somewhat unexpected. It is in agreement with the results of the work of Bejot *et al.* [46] discussed in section 2.2.2, where also the presence of unexpected negative TOD is detected after frequency generation in a hollow-core fiber, even with a completly different set of parameters.

At the parameters chosen for the simulation, with an input Gaussian pulse with $\tau_0 = 28\,\mathrm{fs}$, $\phi(\omega) = 0$ and $E = 830\,\mu\mathrm{J}$ per pulse, and a hollow-core fiber with length $z = 1\,\mathrm{m}$, bore radius $a = 125\,\mu\mathrm{m}$ and filled with neon at $p = 2\,\mathrm{bar}$, the induced negative TOD can be compensated with $+15\,\mathrm{fs}^3$ TOD. That is equivalent to the amount of TOD introduced by 0.5 mm fused silica.

Since the pressure chamber of the gas-filled hollow-core fiber has a fused silica exit

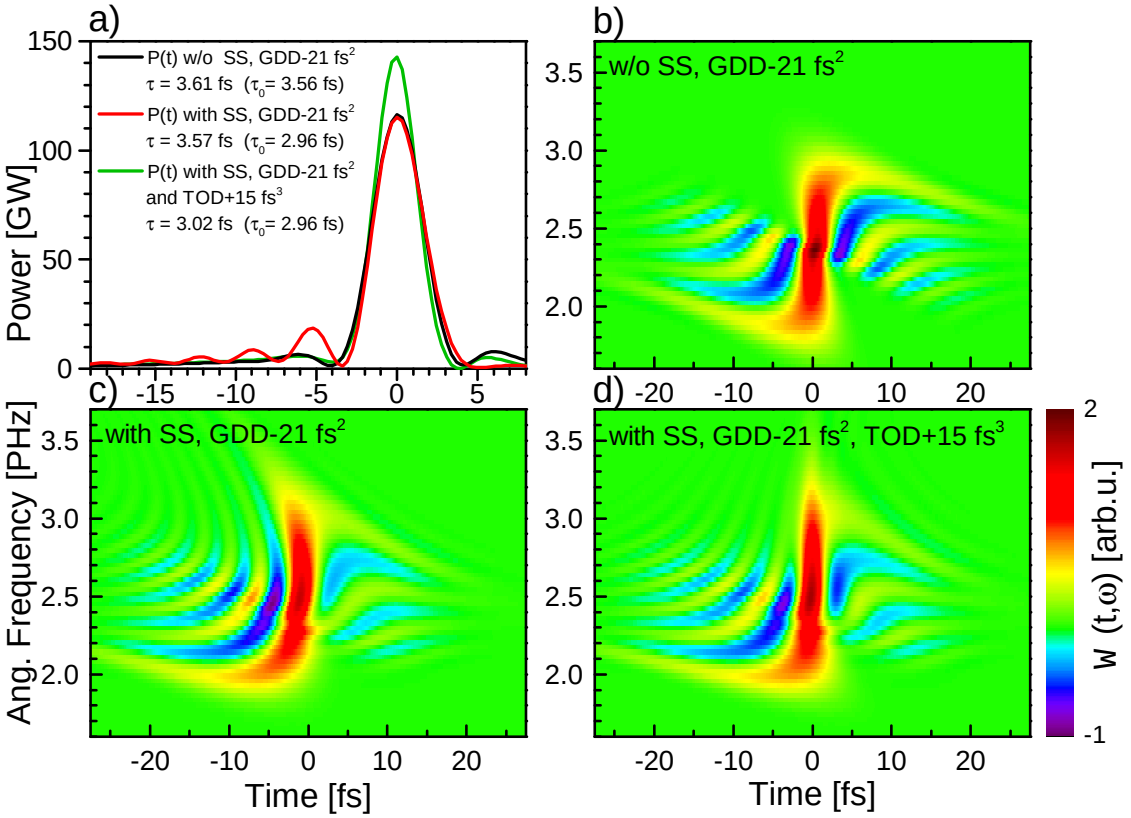

Figure 2.10.: Calculated pulse shape $P(t)$ of a Gaussian beam after HCF and compression in a), without (black) and with (red and green) self-steepening. GDD $-21\,\mathrm{fs}^2$ has been applied after the HCF to compress the pulse, and in one case (green) also $+15\,\mathrm{fs}^3$ TOD. An inset shows the respective FWHM pulse durations and Fourier-limited pulse durations. The pulse shapes of the uncompressed pulses are presented in Fig. 2.8 b).
In b) to d) the respective Wigner plots are presented. These are the same plots as in Fig. 2.8 c), just with additional dispersion for pulse compression.
(Parameters: input Gaussian pulse $\tau_0 = 28\,\mathrm{fs}$, $\phi(\omega) = 0$; HCF $p = 2\,\mathrm{bar}$)

window of about 1 mm thickness, the negative TOD generated in the hollow-core fiber will probably never pose a problem. For someone designing a beamline intended for generating few-cycle pulses this negative TOD is of interest though, to help deciding on the exact dispersion values for the compressor.

3. Results of the Experiment

In this chapter measurements performed in the attosecond laboratory of Universitaet Bielefeld in regard to supercontinuum generation in a gas-filled hollow-core fiber are presented. The interaction of high intensity few-cycle laser pulses with a gas medium is already discussed in the literature [64], but mostly these studies were concerned with a free volume of gas and the formation and the properties of filaments of light. This phenomenon describes the diffractionless propagation of a focused laser beam through a medium over long distances, and it requires high laser pulse powers to maintain a balance between self-focusing due to the Kerr effect and defocusing due to multiphoton ionization [66].

Propagation of a pulse of light inside a gas-filled hollow-core fiber has been less thoroughly studied and there are many open questions about this process yet.

In section 3.1 the experiment for which the supercontinuum studied in this work is generated in the first place is introduced, both to provide a motivation for the investigation and optimization of the supercontinuum, and to present independent confirmation that the *Venteon* SPIDER which is used in our measurements delivers trustworthy results.

As a base for the presented experiments and numerical simulations the input laser pulses are characterized with the SPIDER, in front of the hollow-core fiber in section 3.2 and after the hollow-core fiber in section 3.3.

In section 3.4 the chirped mirror compressor used to compensate the dispersion introduced by the hollow-core fiber and the considerable propagation distance through air and several glass windows is characterized with the SPIDER.

In section 3.5 finally the dependence of the supercontinuum and its spectral amplitude and phase on the gas pressure inside the hollow-core fiber is investigated and compared with the results of the numerical simulation, and it is found that the simulation is in qualitative agreement with the experiment.

3.1. The time-resolved photoelectron spectroscopy experiment

The time-resolved photoelectron spectroscopy experiment is performed to measure the dynamics of electrons with a time scale of attoseconds. The optimization of the single attosecond pulses which are employed in that experiment is ultimately the reason why few-cycles pulses and the supercontinuum necessary to generate them are

studied in this thesis. The time-resolved photoelectron spectroscopy experiment also provides a means to measure the temporal pulse shape and hence the spectral phase $\phi(\omega)$ of the few-cycle infrared laser pulses generated by the laser system discussed so far. This method of measuring the spectral phase is disproportionate more involved and complex than using the SPIDER for the same end, but it provides an important independent source for validation of the SPIDER results.

In section 3.1.1 the experimental setup is described and the process with which single pulses of attosecond duration are generated is explained. In section 3.1.2 the results of the experiment are presented and it is shown that they are in qualitative agreement with the results of the SPIDER.

For a more detailed presentation of the experiment and its results I refer to the two master theses of Sergej Neb [42] and Christian Sander [43] and the intended doctoral thesis of Fabian Merschjohann [67].

3.1.1. Setup

The setup of the attosecond beamline of Universitaet Bielefeld is based on the setup used in the experiment of Cavalieri *et al.* [12].

The source of the laser pulses is the beamline as described in section 2.1.1. After propagation through the hollow-core fiber and compression in the chirped mirror compressor the infrared (IR) laser pulses are directed to the experiment. The setup of the experiment is illustrated in Fig. 3.1. The beam is focused by a spherical mirror with a focal length of $f = 50\,\mathrm{cm}$ and enters a vacuum chamber through a window of 1 mm fused silica with an anti-reflection coating. A gas cell with 2 mm diameter is put shortly behind the focus and the laser beam drills its own entry and exit holes into the thin nickel walls of the cell. The cell is filled with neon gas at ca. 250 mbar.

The dispersion control with the chirped mirror compressor and the fused silica wedges is tuned such that the laser pulses have the shortest possible pulse duration of about $\tau = 5.3\,\mathrm{fs}$, or two optical cycles, when they interact with the gas medium. In a nonlinear process odd order high harmonics of the fundamental beam are generated in the extreme ultraviolet regime (EUV).

The high harmonic radiation consists of pulse trains in which each pulse has attosecond duration. To separate a single attosecond pulse in our setup the carrier-envelope phase (CEP) of the fundamental beam has to be stabilized such that the maximum of the pulse's envelope coincides with a single maximum of the carrier wave, a so called cosine pulse. In addition the incoming pulse has to have a short pulse duration, so that the whole pulse consists of only a few oscillations. These two conditions together provide that the highest energies at the cutoff of the EUV spectrum are only generated at the central maximum of the pulse, and that only a single pulse in the train of attosecond pulses possesses these high energies. If those two conditions are met and the fundamental IR laser pulse is both very short and

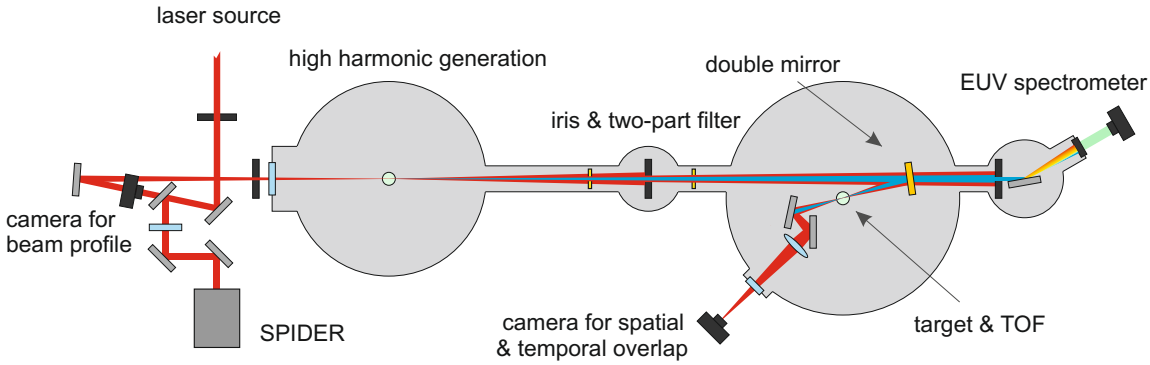

Figure 3.1.: Setup of the experiment for attosecond-resolved photoelectron spectroscopy. The few-cycle IR pulses are focused with a spherical mirror into a gas target for high harmonic generation. Then the IR beam and the generated EUV beam are spatially separated with a two-part filter which consists of a pellicle (blocks EUV, IR can pass) with a zirconium foil in the center (blocks IR, EUV can pass). Both beams are focused on a target with a spherical double mirror which selects the energy of the EUV pulses and controls the time delay between the IR and EUV pulses. Above the target is a TOF which measures the kinetic energy of the photoelectrons emitted from the target. Removal of the target and the two-part filter allows to check for the spatial and temporal overlap of the two beams. Removal of the double mirror allows to characterize beam profile and spectrum of the EUV beam with a spectrometer.

CEP stabilized at a cosine phase, then a single attosecond pulse can be extracted by focusing the beam with an EUV mirror and by filtering out all attosecond pulses with lower energies.

EUV radiation is in an energy regime where light has a high absorption coefficient and a low reflectivity for all materials. For this reason multilayer mirrors, which are tailored to a specific energy and energy bandwidth, have to be employed as mirrors for EUV radiation. This means that it is possible both to focus the beam and to select the required pulse energy with a spherical mirror specifically made for this particular energy and bandwidth [68]. It is a crucial tool in selecting a single attosecond pulse.

In our beamline a multilayer mirror for a central energy of 91 eV is employed, which is equivalent to a wavelength of 13.6 nm or an angular frequency of $1.38 \cdot 10^{17}$ Hz, and a FWHM energy bandwidth of 6 eV, which is enough to support a pulse with a duration of 300 as. With a different choice of mirror it is possible to select another bandwidth, but an increase in bandwidth and hence temporal resolution is balanced with a loss of energy resolution and vice versa, and the mirror has to be chosen in accord with the experiment.

After high harmonic generation in the gas cell the EUV beam is still superimposed with the fundamental IR beam. The two beams are spatially separated with a filter which has two parts. The central diameter is a thin zirconium foil which stops the IR light and lets the EUV pass, while the outer ring is a pellicle which stops the EUV and lets the IR light pass. The amount of transmitted IR light is controlled with an iris aperture. The focussing mirror likewise consists out of two parts. The central part is an EUV multilayer mirror while the outer part is a metal mirror suited for IR light. Both parts of the double mirror have the same focal length of $f = 12.5$ cm and they are moved in regard to each other by means of a piezo translation stage to finely control the time delay between and the spatial overlap of the IR and EUV pulses [42, p. 63].

Both beams are focused on a target, which can be a gas stream or the surface of a solid target. The single EUV attosecond pulse causes the emission of photoelectrons which have a discrete energy depending on the energy of the photon, 91 ± 3 eV, the binding energy of the electron and the work function of the material in question. The kinetic energy of the photoelectrons is measured with a time-of-flight spectrometer (TOF). The photoelectrons are also accelerated by the electric field of the femtosecond IR pulse though, and their kinetic energy is modified by the vector potential of the IR field. The exact amount by which the electron's kinetic energy is shifted depends on the time at which the electron enters the IR field, which in turn is determined by the delay between the EUV and IR pulses.

If photoelectrons are emitted from two different states at different energies, a difference in the energy shift between these photoelectrons can be utilized to determine the moment at which the photoelectrons start interacting with the IR field. This method of determining a difference in time by measuring a difference in another quantity is referred to as streaking.

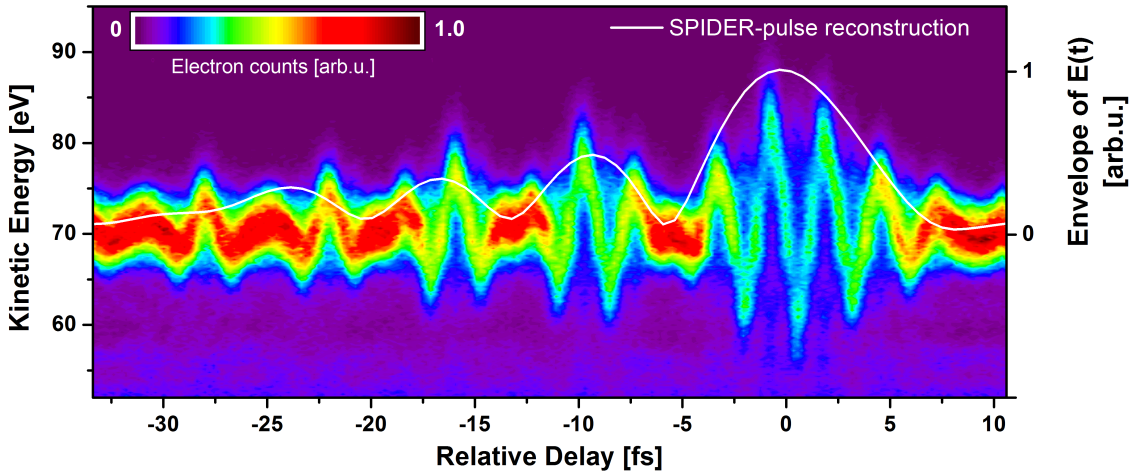

Figure 3.2.: Measurement of the time-resolved streaking of the neon 2p photoelectrons. The white curve marks the square root of the pulse shape as reconstructed by the SPIDER. Figure is taken from [42].

Cavalieri *et al.* reported with an experiment like this that the photoelectrons emitted from the tungsten conduction band and the 4f core state emerge from the tungsten surface with a time difference of 110 ± 70 as.

3.1.2. Results with a gas target

The time-resolved experiment has also been performed with a neon gas target. Neon gas has only one dominant state from which photoelectrons are emitted with an excitation energy of 91 eV. It is the neon 2p state with a binding energy of 21.65 eV [69, p. 2]. While no time difference between different states can be determined this way, the neon 2p peak is easy to observe and it is a common choice to test the functionality of the beamline.

In Fig. 3.2, which is taken from the master thesis of Sergej Neb [42], a measurement of the streaking of the photoelectrons emitted from the neon 2p state is illustrated. The feature which is of interest for this work is the envelope of the streaking oscillations, from which the temporal envelope of the IR pulse can be determined. In this regard the streaking experiment can be used to measure the spectral phase $\phi(\omega)$ of the IR pulse.

This is a method to verify the SPIDER measurement of the IR pulse. As discussed previously in section 2.1.3, the SPIDER can have problems retrieving the spectral phase of a pulse which shows deep minima in its spectral amplitude. Since this is the case for supercontinua generated by propagation through a gas-filled hollow-core fiber, the validity of the SPIDER measurements could conceivably be called

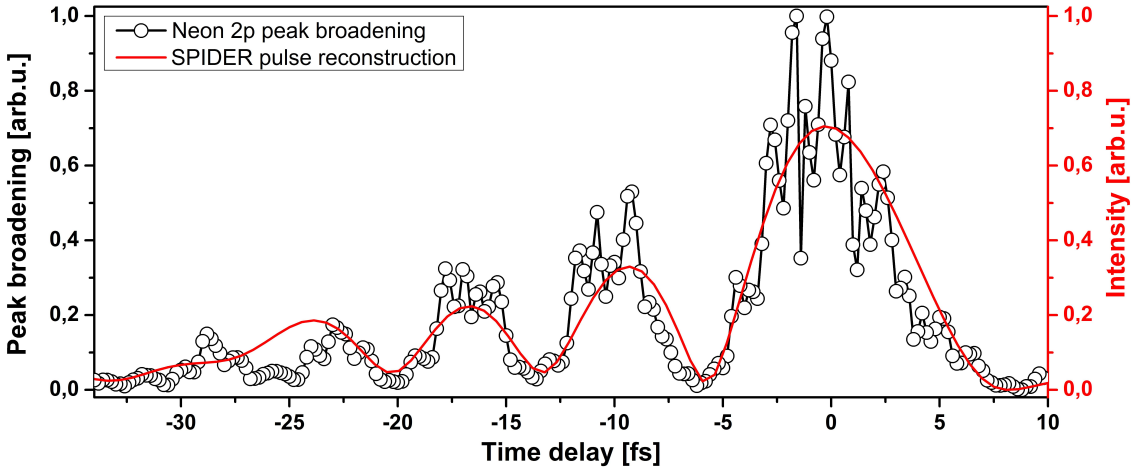

Figure 3.3.: Comparison between the IR pulse shape as retrieved from the streaking experiment and as reconstructed by the SPIDER. Figure is taken from [42].

into question. However, Fig. 3.2 also includes the pulse shape as reconstructed by the SPIDER, which is in qualitative agreement with the measured amplitude of the streaking. Note that the square root of the reconstructed SPIDER pulse shape is depicted, to allow comparison with the envelope of the electric field and instead of its intensity.

A more detailed comparison is provided in Fig. 3.3, which is also taken from [42]. Here the SPIDER results are compared with the broadening of the photoelectron spectrum. The connection between the pulse shape of the IR light and the broadening of the electron spectrum is explained in [42, p. 19]. The latter occurs when the vector potential of the IR light changes signs and the rising edge of the electron peak is affected by a vector potential with a different sign than the back slope of the electron peak. This causes the electron spectrum to broaden, and the envelope of this effect scales with the electric field of the IR pulse.

Fig. 3.3 demonstrates that the pulse shape reconstructed by the SPIDER is in very good agreement with the temporal pulse form contrived from the streaking measurement. This is an important result which confirms that the *Venteon* SPIDER is well suited for the characterization of our few-cycle IR pulses. It is also obvious from Fig. 3.3 that the laser pulses used in the experiment exhibit strong prepulses and possess an excess of negative third order dispersion (TOD). The main source of this TOD is the chirped mirror compressor, an effect which is discussed in section 3.4.

3.2. Pulse properties in front of the hollow-core fiber

In this section we return to the study of the few-cycle infrared pulses and the supercontinuum generated in the gas-filled hollow-core fiber.

In Fig. 3.4 the spectral amplitude, the spectral phase, the group delay and the pulse shape of a typical laser pulse before entry into the hollow-core fiber as measured with the SPIDER are illustrated. This is done for three different settings of the prism compressor that is part of the chirped pulse amplifier. The denomination +0.4 mm means that the prisms are moved 0.4 mm further into the beam and that dispersion is added accordingly.

The spectral amplitude is not smooth and exhibits several small peaks, but follows roughly a Gaussian distribution. The position and ratio of the respective peaks shift slightly with the setting of the prism compressor.

It has been discussed in section 2.1.3 that the SPIDER sets the spectral phase and its first derivative with respect to frequency equal to zero at the central frequency ω_0. In terms of the Taylor series expansion of the spectral phase this means that $\phi_0 = \phi_1 = 0$. The central frequency was set to 2.368 PHz for the measurements, which corresponds to a wavelength of 796 nm, and the respective zero points can be seen in the plots of the spectral phase and the group delay in Fig. 3.4.

Where the spectral amplitude is high the spectral phase is dominated by two oscillations. This is disadvantageous since it makes it necessary to use high order coefficients to expand the spectral phase in a Taylor series. Even with expansion coefficients up to the 8th order the double peak of the spectral phase cannot be resolved, and to achieve a good fit coefficients of up to the 18th order need to be included in the Taylor series. Because of that it is not feasible to quantify the change in dispersion caused by the prism compressor settings just in terms of group delay dispersion (GDD) and third order dispersion (TOD) in the measurement.

The prism compressor has been carefully readjusted to ascertain that no misalignment of the prisms is causing these oscillations in the spectral phase. It is possible that the oscillations are caused by self-phase modulation, for example either in the prism compressor of the amplifier or in the SHG crystal used for measurements of the spectral phase directly after the oscillator, but the matter has not been further investigated by us yet.

Reconstruction of the temporal pulse shapes yields that the pulse with the green plot has the shortest full width half maximum (FWHM) pulse duration τ. It is the black plot though which achieves the broadest supercontinuum after the hollow-core fiber in the experiment.

A possible explanation for this might be provided by the Wigner plots. Of all three plots the default setting (PrismComp0) has the smoothest distribution of the high intensity area in the Wigner distribution. Intensity in this case is meant as the value $\mathcal{W}(t, \omega)$ of the Wigner-Ville distribution, and not as the energy of the pulse. In the leftsided curvature of all three Wigner plots it is observable that the pulses have an imbalance towards negative TOD or higher odd coefficients of the spectral

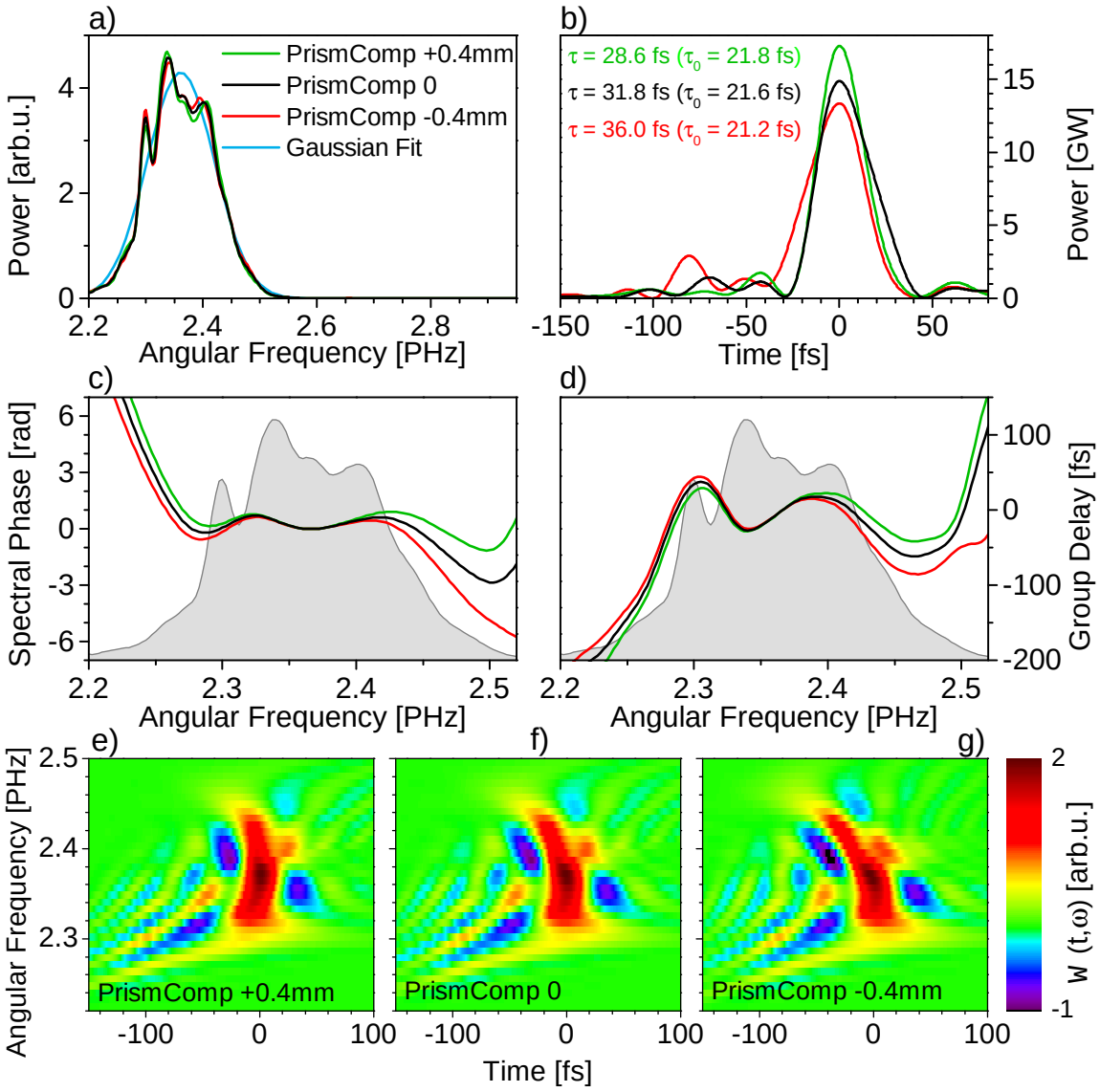

Figure 3.4.: Pulse properties measured before the HCF, a) spectral amplitude $P(\omega)$, b) temporal pulse shape $P(t)$, c) spectral phase $\phi(\omega)$, and d) group delay, where c) and d) are underlayed with the spectral amplitude of PrismComp 0 from a). Measurements for three different settings of the prism compressor are illustrated. In e) to g) the respective Wigner plots are shown. In b) a legend lists the respective pulse durations, where τ is the FWHM duration of $P(t)$ and τ_0 is the Fourier-transform limit.

phase's Taylor series expansion. The interference patterns visible on the left hand side of the Wigner plots are produced by cross-term interference, see section 1.5.2, caused by oscillations in the spectrum and the pulse shape which are a consequence of self-phase modulation.

These measurements were done with the *Venteon* SPIDER, which is usually positioned behind the hollow-core fiber for characterization of the ultra short pulses. Because of that it is not available for constant survey of the input pulses in front of the hollow-core fiber, and none of the measurements shown in this chapter come with a simultaneously done characterization of the input pulse. As such the measurements of Fig. 3.4 are only meant as a typical examples for the input pulses. Some variation of the spectral phase from day to day has to be expected, especially in consequence of readjustment of either the laser oscillator or the amplifier, but this has not been systematically investigated.

3.3. Pulse properties after the hollow-core fiber

In this section the properties of two exemplary laser pulses after the gas-filled hollow-core fiber, the chirped mirror compressor and the fused silica wedges are presented and briefly discussed. This serves as a reference for later sections, when pulse properties and their dependence on parameters like the gas pressure will be studied in more detail.

After propagation through the gas-filled hollow-core fiber the energy per pulse is down to about 66% of the original energy in front of the hollow-core fiber, if the fiber is well aligned. Or about 57% when the pair of fused silica wedges positioned shortly after the fiber is also accounted for. Measurements have shown that this is independent of the gas pressure, so neither absorption in gas nor the nonlinear process, which strongly depends on the gas pressure, are relevant factors for transmission.

Fig. 3.5 shows the properties of two different pulses after propagation through the hollow-core fiber, wedges and chirped mirror compressor.

The oscillations in the spectra seen in Fig. 3.5 a) are characteristic for pulses after frequency generation in a fiber, for hollow-core fibers [70] as well as for solid optical fibers [29]. They are caused by self-phase modulation, the fundamental process responsible for the generation of new frequencies in a fiber. It will be shown later in section 4.2 that the spectral phase of the input pulse is mainly responsible for the form of these oscillations. The spectra of the two different pulses are very similar to each other.

The SPIDER assigns different linear gradients to the two respective spectral phases, but these have no influence on the pulses' temporal shape or duration and simply shift the pulse as a whole in the time domain, as was discussed in section 1.1.2. The peaks of the spectral phase of both pulses do coincide, and as such the two spectral phases resemble each other.

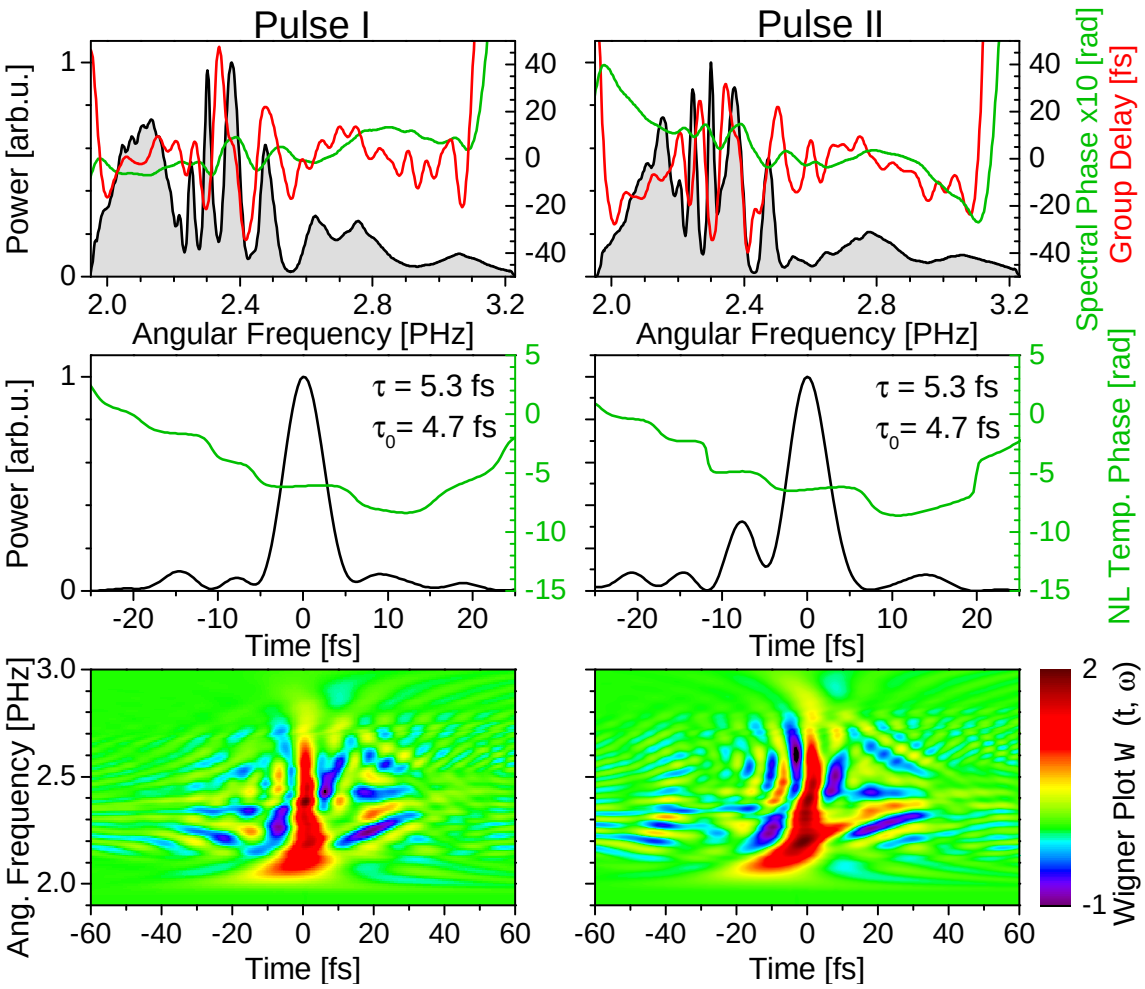

Figure 3.5.: Example of pulse properties measured behind the HCF, the chirped mirror compressor and the wedges. In a) spectrum $P(\omega)$, spectral phase $\phi(\omega)$ and group delay, in b) pulse shape $P(t)$ and nonlinear temporal phase $\phi_a(t)$, and in c) the respective Wigner plot. The y-axis on the right hand side of a) serves for both the spectral phase and the group delay, with different units respectively. For better resolution the spectral phase has been multiplied by 10. On the left hand side one pulse with a very smooth pulse shape is depicted, and on the right hand side a more typical pulse with TOD-induced prepulse. Both pulses have the same FWHM duration. One month passed between measurements.
Left hand side: $E = 845\,\mu\text{J}$ per pulse, $p = 3\,\text{bar}$
Right hand side: $E = 835\,\mu\text{J}$ per pulse, $p = 2.95\,\text{bar}$

They are not the same however, as is apparent in Fig. 3.5 b) in the plots of the temporal pulse shape. Pulse I on the left hand side has a central peak and only negligible side pulses, while pulse II on the right hand side has a prepulse of 30% intensity caused by negative TOD. Pulse I and II have both the same FWHM pulse duration and the same Fourier-transform limited pulse duration though.

The same observation is made in the respective Wigner plots of the two pulses. For pulse I all high intensity components of $\mathcal{W}(t,\omega)$ are gathered in a narrow band at time $t = 0$ and it is nearly ideally compressed, with the exception of the frequencies below 2.2 PHz. The Wigner plot of pulse II in comparison shows a curvature to the left, which is a sign of negative TOD (see Fig. 1.4). $\mathcal{W}(t,\omega)$ is also less concentrated and has components spread over a larger time t. The frequencies below 2.2 PHz show a notable amount of uncompensated dispersion, same as for pulse I. The latter feature has already been observed in the simulations of Fig. 2.10 on page 53.

It has to be mentioned that a pulse such as pulse II on the right hand side of Fig. 3.5 is more often observable in the experiment, and a pulse without side pulses in the temporal shape requires careful adjustment of the complete system. It stands to reason that an imbalance towards negative TOD is present in the laser pulses. It has been shown in section 2.2.3 that the nonlinear process in the hollow-core fiber is responsible for a small part of that negative TOD. In the next section the effects of the chirped mirror compressor are discussed, which is another source of negative TOD in the beamline.

3.4. The chirped mirror compressor

The chirped mirror compressor (CMC) is required to compress the laser pulses after propagation through the hollow-core fiber. It also pre-compensates the dispersion which is introduced by passing through objects like the wedges and the glass windows of the pressure and vacuum chambers and simple distance in air such that the laser pulses achieve their shortest duration not directly after the CMC, but at a critical point in the experiment which is a distance of several meters away.

We use an arrangement of six chirped mirrors from *FemtoLasers*, which are specified to compensate $-45 \pm 10\,\mathrm{fs}^2$ GDD per bounce for a wavelength range of 620 to 920 nm, corresponding to frequencies of 2.05 to 3.05 PHz. It is not specified how much TOD is compensated by the mirrors. To investigate the smoothness of the spectral phase applied by the CMC and to verify the amount of GDD and TOD it compensates, measurements with the SPIDER with and without the CMC have been performed. For this the CMC was bypassed with a pair of mirrors.

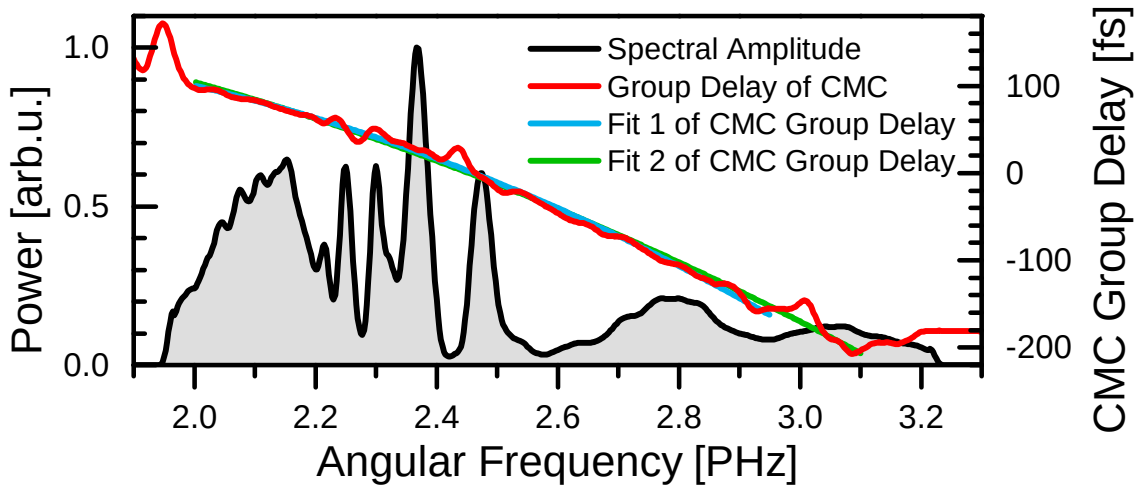

Figure 3.6.: Measurement of the group delay caused by the chirped mirror compressor. Dispersion caused by the propagation distance in air has been deducted. The blue plot is a 2nd order polynomial fit which results in GDD $-248\,\mathrm{fs}^2$ and TOD $-244\,\mathrm{fs}^3$. The green plot is a fit which results in GDD $-251\,\mathrm{fs}^2$ and TOD $-162\,\mathrm{fs}^3$.

	GDD [fs^2]	TOD [fs^3]
1 m Air	20	12
1 mm Fused Silica	36.1	27.4
Beamline (6.3 m air, 2.5 mm FS	216	143
Typical dispersion after HCF (simulation)	36	-32
Total	252	111
CMC (fit)	-250	-162 to -244
Difference	-2	-51 to -133

The dispersion coefficients of air at room temperature, $p = 1\,\mathrm{bar}$ and a wavelength of 800 nm are $+20\,\mathrm{fs}^2/\mathrm{m}$ GDD and $+12\,\mathrm{fs}^3/\mathrm{m}$ TOD [19], about an order of magnitude higher than for neon gas. If the dispersion caused by the propagation through air is accounted for in the calculations, the dispersion which is solely caused by the CMC mirrors can be retrieved. The result is illustrated in Fig. 3.6.

A second order polynomial is fitted to the measured group delay to estimate the dispersion caused by the chirped mirrors. Fit 1 extends over a frequency of 2 PHz to 2.95 PHz and delivers a dispersion of $-248\,\mathrm{fs}^2$ GDD and $-244\,\mathrm{fs}^3$ TOD. The limits of the supporting frequency are chosen such that it is possible to fit the polynomial close to the measured group delay and the mean square error is only $27.9\,\mathrm{fs}^2$. However, if the limit is extended to a frequency of 3.1 PHz for fit 2, the fit delivers a dispersion of $-251\,\mathrm{fs}^2$ GDD and $-162\,\mathrm{fs}^3$ TOD with a mean square error of $52.6\,\mathrm{fs}^2$, which is

nearly twice as much as for fit 1. The difference in estimation of GDD is negligible, but the result for TOD is very sensitive to the limits of the supporting frequency. Because of this the results of the fits have to be taken as a rough approximation for TOD.

The fits deliver a dispersion of $-41.3\,\mathrm{fs}^2$ GDD and $-40.7\,\mathrm{fs}^3$ TOD, or $-41.8\,\mathrm{fs}^2$ GDD and $-27\,\mathrm{fs}^3$ TOD, in average per bounce, which is in quantitative agreement with the mirror specification of $-45 \pm 10\,\mathrm{fs}^2$ GDD per bounce. A specification of dispersion per bounce is potentially misleading though. The dispersion introduced by a single chirped mirror has pronounced oscillations, which are compensated by using chirped mirrors in matched pairs to achieve a dispersion which is as smooth as possible in average [61, p. 553]. As such the small oscillations in the group delay observable in Fig. 3.6 are not surprising. It is also obvious that these small oscillations are mainly at frequencies where the spectral amplitude has low intensities and the SPIDER measurement is less reliable.

The beamline covers about 6.30 m distance in air and 2.5 mm in fused silica from leaving the pressure chamber of the hollow-core fiber to entering the vacuum chamber of the experiment. This amounts to a dispersion of $+216\,\mathrm{fs}^2$ GDD and $+143\,\mathrm{fs}^3$ TOD. Results of numerical simulations suggest that typical laser pulses in our setup have a dispersion of $+36\,\mathrm{fs}^2$ GDD and -32 fs^3 TOD upon exit from the hollow-core fiber. It follows that the compressor has to compensate for about $+252\,\mathrm{fs}^2$ GDD and $+111\,\mathrm{fs}^3$ TOD in total. The fit in Fig. 3.6 estimates the dispersion actually provided by the CMC to be about $-250\,\mathrm{fs}^2$ GDD and between $-244\,\mathrm{fs}^3$ and $-162\,\mathrm{fs}^3$ TOD. The GDD is in good agreement and the difference can easily be adjusted with the wedges. However, there is a big surplus of negative TOD, between -51 and $-133\,\mathrm{fs}^3$. It is this negative TOD, introduced by the CMC and the nonlinear process in the HCF, which is responsible for the prepulses in the temporal envelope of type II pulses depicted in Fig. 3.5.

3.5. Dependency on gas pressure and comparison with numerical simulation

The nonlinear process in the hollow-core fiber depends on many parameters, as the properties of the input laser pulse (power, spectral apmlitude and spectral phase) and the properties of the hollow fiber (diameter, length, gas type and gas pressure). In this section measurements of the supercontinuum's spectral amplitude and spectral phase in dependency on the gas pressure inside the hollow-core fiber are presented and compared to the results of numerical simulations, which have been calculated with the parameters used in the experiment.

The measurements were performed with the SPIDER placed after the hollow-core fiber, the wedges and the chirped mirror compressor.

The section starts with an investigation how accurately the input parameters for

the simulation are known from the experiment and what consequences fluctuations of those parameters have. Then the results of experiment and calculation are presented for three different gas pressures, 0.8 bar, 1.8 bar and 2.8 bar respectively. This is followed by a more complex pressure-dependent pseudocolor representation where the spectrum is illustrated in pressure steps of $\Delta p = 0.05$ bar from 0.05 to 3 bar.

The discussion of the results is mostly done in form of a description and comparison of the data. Explanations of some specific features are presented in chapter 4, where the properties of the supercontinuum are further explored with the help of numerical simulations.

The default parameters for the numerical simulations are those used in the experiment: input spectral amplitude and phase as in experiment (Fig. 3.4, PrismComp0), $\omega_0 = 2.365$ PHz, $E = 830$ µJ per pulse; hollow-core fiber length $z = 1$ m, bore radius $a = 125$ µm, neon gas at $p = 3$ bar.

3.5.1. Uncertainty of simulation parameters

The accuracy of a comparison between the results of a numerical calculation and an experiment naturally depends on the accuracy with which the various input parameters of the simulation are known in the experiment.

The parameters affiliated with the gas-filled hollow-core fiber are bore radius and length of the fiber, and gas pressure inside the fiber. Of these quantities the bore radius has not been verified and is specified as $a = 125$ µm. Simulations yield that an error of $\Delta a = \pm 5$ µm, or $\pm 4\%$, when otherwise typical parameters from the experiment are used, results in a Fourier-transform limited (FTL) pulse duration τ_0 after the hollow-core fiber of 4.4 ± 0.3 fs, or a difference of $\pm 6\%$. This is a possible source of systematic error.

The actual length of the fiber is 1.004 m instead of exactly 1 m. This additional bit of distance reduces the FTL duration τ_0 about 0.02 fs (at otherwise typical parameters) and can hence be safely ignored.

The gas pressure is measured with two different manometers, one at the reducing valve of the gas cylinder with an accuracy of reading of ± 50 mbar, and a second manometer at the pressure chamber of the hollow-core fiber with an accuracy of reading of ± 10 mbar. This keeps variations in the day-to-day gas pressure small, with an estimated influence on the FTL duration of $\Delta\tau_0 \simeq \pm 0.02$ fs, so that they can be neglected. However, the second manometer has been calibrated with the manometer of the reducing valve and its less fine reading accuracy, which is another possible source of systematic error. Hence the potential systematic error due to uncertainties of the pressure measurement is estimated to be $\Delta\tau_0 \simeq \pm 0.1$ fs.

The parameters affiliated with the input laser pulses in front of the hollow-core fiber are the power, spectral amplitude and spectral phase of the pulses.

Measurements with a *LeCroy WaveSurfer 104Xs* digital oscilloscope yield that the laser pulses have a shot-to-shot energy per pulse stability of about 1%. At typical parameters this results in $\Delta\tau_0 \simeq \pm 0.05\,\mathrm{fs}$. If the gas pressure varied at random, this energy fluctuation would correspond to a pressure uncertainty of $\pm 40\,\mathrm{mbar}$, which is of interest for the pressure pseudocolor plots of Fig. 3.10 later in this chapter.

The spectral amplitude is measured with an *Avantes Avaspec-2048* spectrometer which is part of the *Venteon* SPIDER. In section 4.2 it is shown though that small variations of the input spectral amplitude have no notable influence on the results of the numerical simulation. The uncertainty introduced by measurements of the spectral amplitude can hence be neglected.

The spectral phase of the input laser pulses is a very sensible parameter however. In section 4.2.1 it is shown that the settings of the prism compressor of the CPA amplifier in front of the fiber have a great impact on the supercontinuum after the fiber, and not only insofar that the spectral phase determines the duration and hence the peak power of the pulses in front of the fiber.

Also, the day-to-day stability of the spectral phase in front of the fiber has not been thouroughly investigated yet. The SPIDER is an expensive instrument and we only have one SPIDER at our disposal. For this reason none of the measurements after the fiber presented in this section come with a simultaneous measurement of the spectral phase in front of the fiber. It is not uncommon to have to adjust the prisms of the prism compressor for $\pm 0.2\,\mathrm{mm}$, and Fig. 4.3 illustrates the consequences for the supercontinuum with a change of $\pm 0.4\,\mathrm{mm}$ of the prisms. Because of that it is difficult to attach the correct input spectral phase to a measurement of the supercontinuum after the fiber and this remains a degree of freedom in the comparison of measurement and simulation.

3.5.2. Spectrum line scans dependent on pressure

In Fig. 3.7 to 3.9 the spectral amplitude $P(\omega)$, the spectral phase $\phi(\omega)$ and the group delay, the first derivative of the spectral phase with respect to ω, are illustrated for gas pressures of 0.8 bar, 1.8 bar and 2.8 bar in the hollow-core fiber. The pressure values have been chosen to represent low, middle and high gas pressures. Each plot depicts two different measurements, which have been performed at different days, and the numeric simulation. The results of the two different measurements generally agree with each other apart from minor deviations for all three exemplary pressures, which is evidence to the reproducibility of the experiment. Of greater interest is the comparison between the measurements and the numerical calculation.

Since the three depicted quantities, spectral amplitude, spectral phase and group delay, each have their own respective properties, the discussion of the figures is grouped according to those quantities for simplicity's sake.

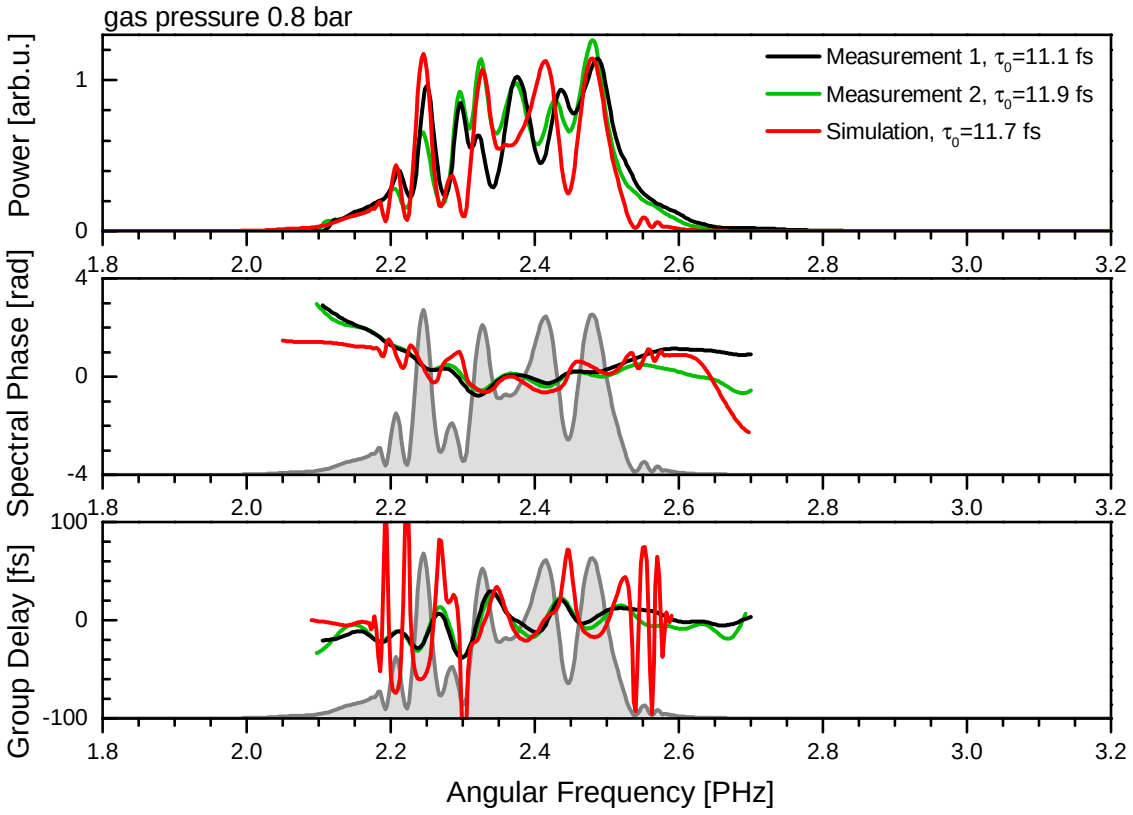

Figure 3.7.: Measurements and numerical calculation of the spectral amplitude $P(\omega)$, the spectral phase $\phi(\omega)$ and the group delay after HCF, CMC and wedges. HCF is filled with neon at 1.8 bar pressure. The graphs for spectral phase and group delay show the calculated spectrum as a reference.
(Parameters: input spectral amplitude and phase as in experiment (Fig. 3.4, PrismComp0), $E = 830\,\mu J$ per pulse, HCF length $z = 1\,m$, bore radius $a = 125\,\mu m$, neon gas)

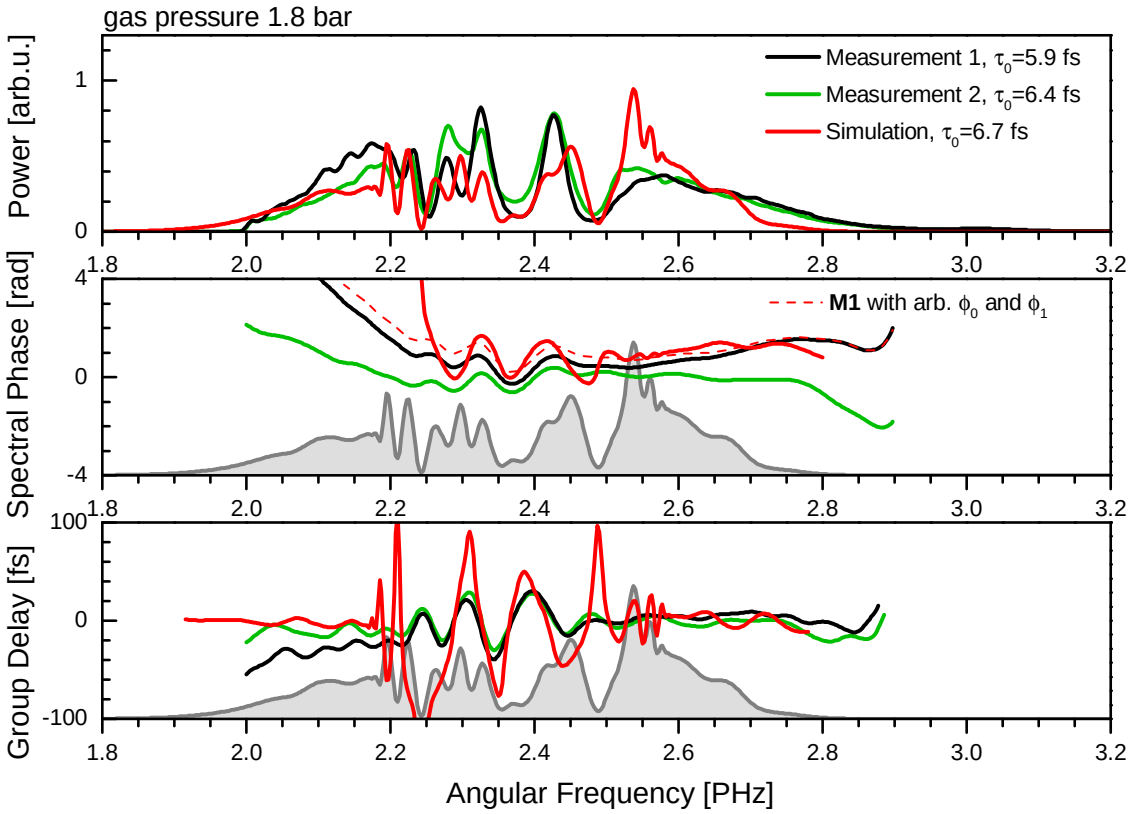

Figure 3.8.: Measurements and numerical calculation of the spectral amplitude $P(\omega)$, the spectral phase $\phi(\omega)$ and the group delay after HCF, CMC and wedges. HCF is filled with neon at 1.8 bar pressure. The graphs for spectral phase and group delay show the calculated spectrum as a reference. The graph for the spectral phase also shows a thin black line, which is the spectral phase of measurement 1 with arbitrary coefficients for ϕ_0 and ϕ_1 to match it to the calculated data.
(Parameters: input spectral amplitude and phase as in experiment (Fig. 3.4, PrismComp0), $E = 830\,\mu J$ per pulse, HCF length $z = 1\,m$, bore radius $a = 125\,\mu m$, neon gas)

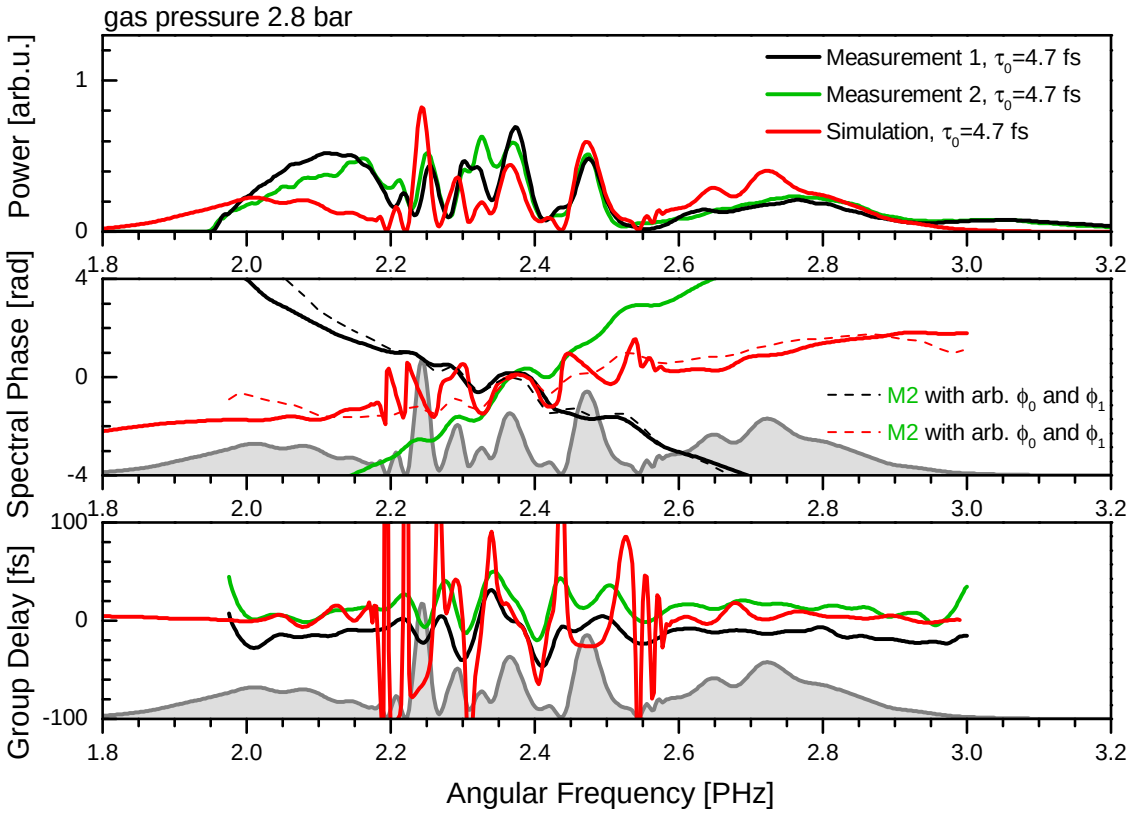

Figure 3.9.: Measurements and numerical calculation of the spectral amplitude $P(\omega)$, the spectral phase $\phi(\omega)$ and the group delay after HCF, CMC and wedges. HCF is filled with neon at 2.8 bar pressure. The graphs for spectral phase and group delay show the calculated spectrum as a reference. The graph for the spectral phase also shows two thin green lines, which are the spectral phase of measurement 2 with arbitrary coefficients for ϕ_0 and ϕ_1 to match it to the two other curves.
(Parameters: input spectral amplitude and phase as in experiment (Fig. 3.4, PrismComp0), $E = 830\,\mu\text{J}$ per pulse, HCF length $z = 1\,\text{m}$, bore radius $a = 125\,\mu\text{m}$, neon gas)

Spectral amplitude

The spectral amplitude is rather straightforward. At 0.8 bar the agreement of the calculated spectral amplitude with the measured data is good for the low and high frequency peaks and side wings, and hence produces a very similar bandwidth. The position of the central peaks does not coincide as well though and shows some small deviation in peak position and height.

At 1.8 bar the agreement between measured and calculated data is generally good for both the side wings and most peaks.

At 2.8 bar a discrepancy at the low frequency side wing, which begins to be observable at 1.8 bar, has become very distinct. In the measurements the left sidewing has the form of a large round bump with steep flanks, while in the simulation it is a low and nearly symmetric elevation which is shifted to lower frequencies.

At all pressures the simulation shows a series of fast oscillations between 2.52 and 2.58 PHz which is not evident in the measurements.

The Fourier-transform limited (FTL) pulse duration τ_0 of the respective spectral amplitudes is calculated as the FWHM duration of the Fourier-transform of the spectral amplitude without a spectral phase. It defines the shortest possible pulse duration for that spectral amplitude. At each gas pressure the values for τ_0 are only spread over a small range, and they are even identical at $p = 2.8$ bar. This is in indicator that the simulated spectral amplitude is in general good agreement with the measured spectral amplitude.

Spectral phase

Before comparing the spectral phase $\phi(\omega)$ one has to consider that the SPIDER does not measure the carrier-envelope phase (CEP), which is the zero order coefficient of the Taylor series expansion of the spectral phase, and simply sets $\phi(\omega_0)$ equal to zero. As such each measured spectral phase plot can have an arbitrary offset added to it. The same applies to the first order coefficient of the expansion and the SPIDER also sets $\phi_1(\omega_0)$ equal to zero. This means that each measured spectral phase plot can have an arbitrary linear gradient added to it. That are two important degrees of freedom in the comparison of the spectral phase which have no impact on the form of the temporal envelope of the pulse, but make interpretation of the spectral phase less intuitive. Often it is easier to compare the group delay instead, which has only one degree of freedom in form of an arbitrary offset for ϕ_1.

It is also important to keep in mind that the spectral phase and the group delay at a particular frequency are of no relevance when the corresponding spectral amplitude has no intensity at that frequency. As illustrated in Fig. 1.2 on page 23, the spectral phase of a pulse which has experienced self-phase modulation (SPM) can show strong shifts in frequency areas with low spectral intensity. Accordingly the group delay exhibits pronounced peaks when this happens. Such peaks immediatly catch the eye when looking at the grop delay, but when they take place in areas of low spectral

intensity they have only a small impact on pulse properties like the temporal pulse shape, for example.

That said, the spectral phase of the two different measurements is nearly identical at 0.8 bar even without any adjustment to ϕ_0 or ϕ_1. At 1.8 bar a slight offset would be necessary to superimpose the two measurements, and at 2.8 bar it is also necessary to change the gradient of one of the measured spectral phases to bring them in agreement. However, if this is done, as illustrated by one of the thin green plots in Fig. 3.9, the spectral phase of the two different measurements is in good agreement for each of the three exemplary gas pressures.

The calculated spectral phase agrees well with the measured data at 0.8 bar, and a bit less so at 1.8 bar. At a pressure of 2.8 bar only slight similarities exist between the calculated and the measured spectral phase.

Group delay

In the graphs of the group delay it is readily apparent that the peaks of the group delay, minima as maxima, coincide with the low intensity minima of the spectral amplitude. The higher the gas pressure the more efficient is the SPM process, and the sharper are the spectral amplitude minima and the higher are the group delay oscillations. It is also observable that the measured group delay only slowly follows the sharp and high oscillations of the calculated group delay. In fact the measured group delay looks like the calculated group delay smoothed with a FFT lowpass filter which eliminates oscillations with a high frequency. This suggests that the SPIDER might simply not be able to resolve the fast oscillations of the group delay. A possible explanation for this is that the high oscillations of the group delay occur at frequencies where the spectral amplitude is low. The SPIDER, which uses a nonlinear process for frequency shearing, is naturally less sensitive at frequencies with low spectral amplitude. However, this is not further investigated in this work and remains speculation.

At 0.8 bar the calculated group delay is in reasonable agreement with the measured data. As with the spectral phase, the similarities between the measured and calculated group delay decrease with an increase of the gas pressure.

However, while the line scans presented in this section are useful to compare the features of the spectrum at a particular gas pressure in detail, they are not well suited to illustrate the development of those features in dependence on the gas pressure. To help visualize this dependency, pseudocolor plots are used in the next section.

3.5.3. Pressure pseudocolor plots

In Fig. 3.10 the pressure-dependency of the spectral amplitude and phase, or rather the group delay, after the hollow-core fiber is illustrated in pseudocolor plots. The

group delay has been chosen instead of the spectral phase because it contains the same information, and to avoid having to adjust the gradient of the spectral phase for each step in gas pressure due to the indeterminacy of ϕ_1 in the SPIDER measurements. For the group delay this only results in an arbitrary offset, which has not been varied in Fig. 3.10. Like in the linescans before, the results of two measurements from different days and for the numerical simulation are depicted.

In section 3.5.1 it is ascertained that the shot-to-shot fluctuations of the laser power of about $\pm 1\%$ cause deviations in the spectrum which correspond to fluctuations of the gas pressure of $\pm 0.04\,\mathrm{bar}$. From this follows that the power fluctuations cause each line of the pressure-dependent pseudocolor plots to actually be an average of ± 1 line for measurement 1, which has a stepsize of $\Delta p = 0.05\,\mathrm{bar}$, and $\pm 1/2$ line for measurement 2, which has a stepsize of $\Delta p = 0.1\,\mathrm{bar}$.

Spectral amplitude

By looking at any of the presented pseudocolor plots for the spectral amplitude of Fig. 3.10, it is observable that the pressure dependency of the spectrum follows a specific pattern.

Each spectrum consists of several more or less sharp central peaks and a wing at each side. The central peaks keep their position in frequency and increase and decrease over a pressure range of about 1 bar into and out of existence. Eventually a new peak rises again at the same frequency. In pressure regions where old peaks vanish and new peaks rise the two sets of peaks reach into each other like the teeth of two combs.

The side wings shift their position in frequency, wandering outwards with increasing gas pressure. In the measurements the high frequency side wing has a lower amplitude than the low frequency side wing, while in the simulation it is the other way round. Both side wings exhibit peaks which remain at constant frequency, as the central peaks do, but they are less visible due to a lower contrast and are difficult to discern at all.

The simulation exhibit fast oscillations of the spectral amplitude at ca. 2.21 PHz and at ca. 2.55 PHz, which is symmetric around the central frequency ω_0. The pseudocolor plots, in contrast to the line scans, reveal that the measurements also show these oscillations, but at reduced resolution.

Overall the qualitative agreement of the simulated spectral amplitude with the measured spectral amplitude is very impressive, both in the general behavior of the side wings and the dynamic of the central peaks.

Group delay

The pseudocolor plots for the measured group delay in Fig. 3.10 show some blank areas in black or white where the measured values go beyond the range of the color

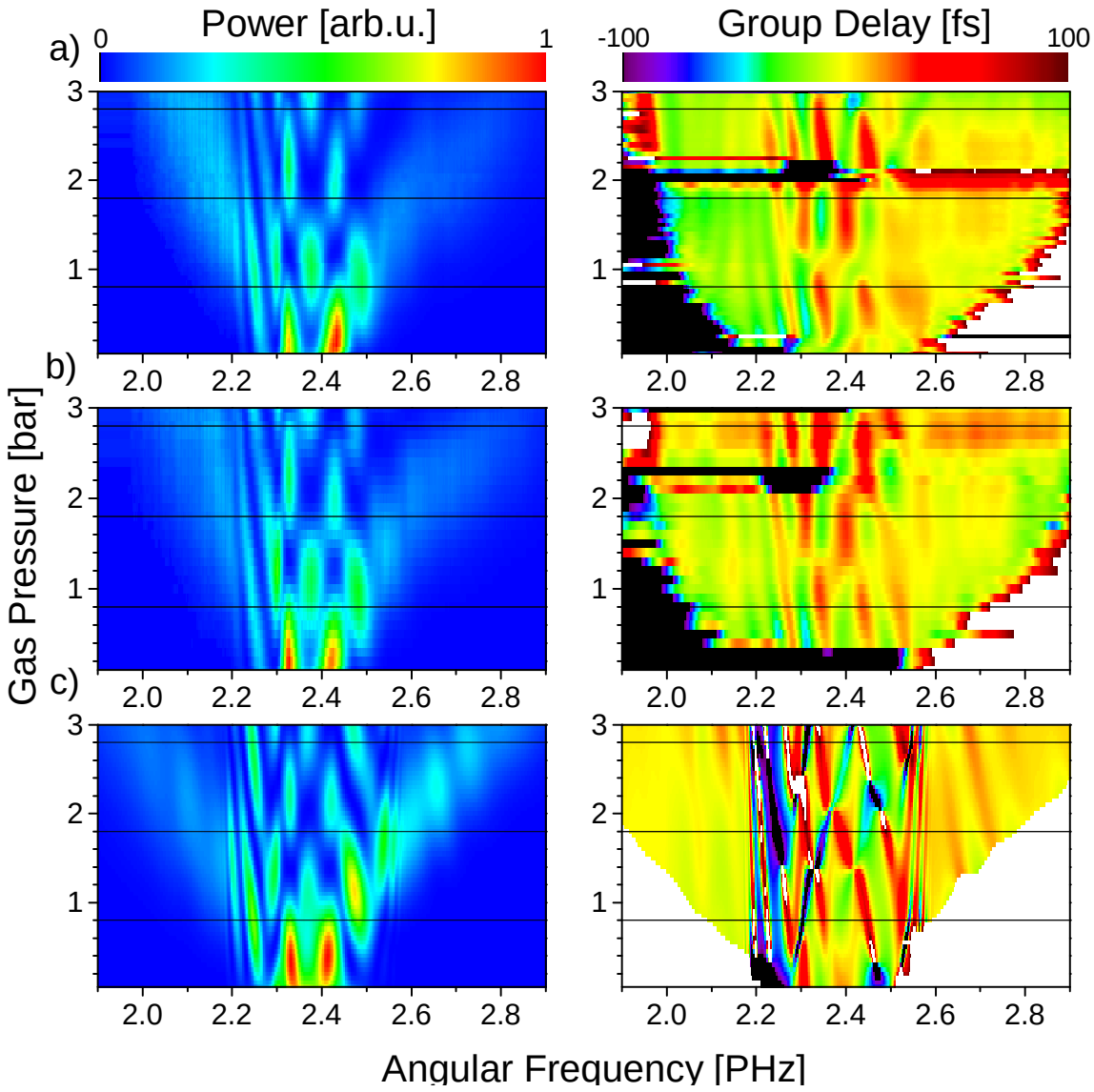

Figure 3.10.: Spectral amplitude $P(\omega)$ and group delay after HCF in dependence on gas pressure in HCF, in a) measurement 1, in b) measurement 2 and in c) numerical simulation. The black lines mark the positions of the line scans which are shown in Fig. 3.7 to 3.9. Note that the pressure axis starts with an offset since it is not possible to achieve pressures of less than $p = 50\,\mathrm{mbar}$ with the employed vacuum pump.
(Parameters: input spectral amplitude and phase as in experiment (Fig. 3.4, PrismComp0), $E = 830\,\mu\mathrm{J}$ per pulse; HCF length $z = 1\,\mathrm{m}$, bore radius $a = 125\,\mu\mathrm{m}$), neon gas

scale. This is to be expected for the lower left and right corners. These are areas where the spectral amplitude has no noteworthy intensity and where the spectral phase and hence the group delay has no physical meaning.

There are also blank spots in the middle of each of the measured plots, around ca. 2.2 bar. These are due to the limitation of the SPIDER, discussed in section 2.1.3, to reconstruct the spectral phase in regions where the spectral amplitude has an intensity near zero.

The spectral phase, or the group delay directly, suffers a discontinuity at those points and accordingly a noteworthy offset, which moves those data points beyond the limits of the color scale. It is possible to make an educated guess about the amount of this offset, especially under consideration of the measurements without discontinuity, and show result graphs with the blank areas filled in. However, for this work it has been preferred to show the unmodified data.

The blank areas in the simulated pseudocolor plot are simply regions where the value of the group delay lies outside the range of the color scale. This is unavoidable since the same color scale as for the measured group delay is being used, but as it is known from the line scans, the simulated group delay does oscillate with a much higher amplitude than the measured group delay.

The plots for the measured group delay in Fig. 3.10 show similar characteristics as the spectral amplitude. There are no side wings, but there are well defined peaks for the central frequencies which do not shift in frequency. As for the spectral amplitude, these peaks remain stable while they increase and decrease over a pressure range of about 1 bar or a bit less.

However, it is striking that the regions where these peaks are at their maximum and the regions where they are about to vanish, and in the process of being replaced by a new set of peaks at another frequency, are shifted for half a period in comparison to the peaks of the spectral amplitude. This is for example demonstrated at gas pressures of $p = 1$ bar and $p = 1.5$ bar in the plots of Fig. 3.10 a). At 1 bar the peaks of the spectral amplitude have reached their maximum while those of the group delay are about to change frequency, while at 1.5 bar the peaks of the spectral amplitude are about to change frequency while those of the group delay have reached their maximum. This behaviour is observable in each of the pseudocolor plot pairs.

The appearance of the simulated group delay is in some aspects different from that of the measured group delay. As already observed in the line scans, the oscillations of the group delay in the simulation are higher and narrower than in the measurements.

In the pressure-dependent pseudocolor plot it is also apparent that the group delay peaks do not remain stationary at the same frequency, like the peaks of the spectral amplitude, but shift continuously in frequency. In general the maxima shift to lower frequencies with increasing gas pressure, while the minima shift to higher frequencies. At the intersections where these lines cross the group delay often assumes extreme values. This happens because these intersections correspond to minima of the spectral

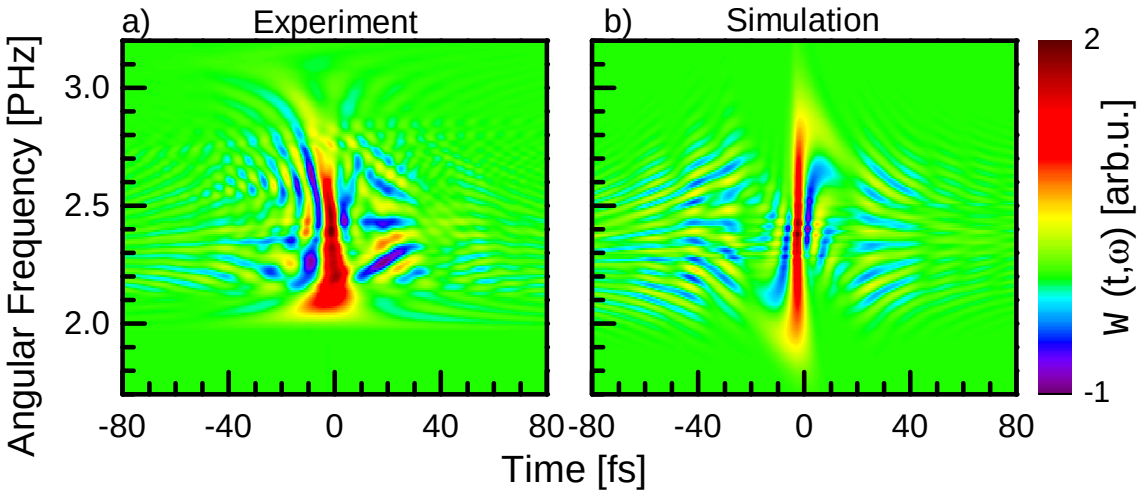

Figure 3.11.: Wigner plots after HCF with $p = 2.9\,\text{bar}$. In the experiment the spectral phase was optimized with application of a pair of wedges. In the simulation GDD and TOD were optimized independently of each other (with -30 fs^2 GDD and +20 fs^2 TOD).

amplitude in the pressure-dependent plot.

The measured plots for the group delay show in tendency the same behavior as the simulation, but with less contrast and detail, as if smoothed by some filter. Whether this is caused by a physical process which is not considered in the numerical simulation or simply by an inability of the SPIDER to resolve the fine details of the group delay can currently not be determined.

Wigner plots

In Fig. 3.11 Wigner plots for gas pressures of $p = 2.9\,\text{bar}$ for both experiment and simulation are illustrated. In the curved form of the high $\mathcal{W}(t, \omega)$ region in the measured data in a) it is apparent that pulse compression is not yet optimal in the experiment. See Fig. 3.4 on page 62 for an example where better compensation of the spectral phase is achieved. Both measured plots demonstrate a disadvantageous peak broadening for low frequencies though. A comparison with Fig. 3.6 shows that the chirped mirror compressor should work fine at the respective frequencies, so this effect might be caused by a process in the hollow-core fiber which is not covered by the numerical simulation.

For the simulated data in Fig. 3.11 b) compression is adjusted by optimizing GDD and TOD independent of each other, in this case with -30 fs^2 GDD and +20 fs^2 TOD, which is unfortunately not possible in the experiment since the only degree of freedom to change the dispersion is the wedge position. In the direct comparison between the measured and the calculated data it is obvious that the spectral phase

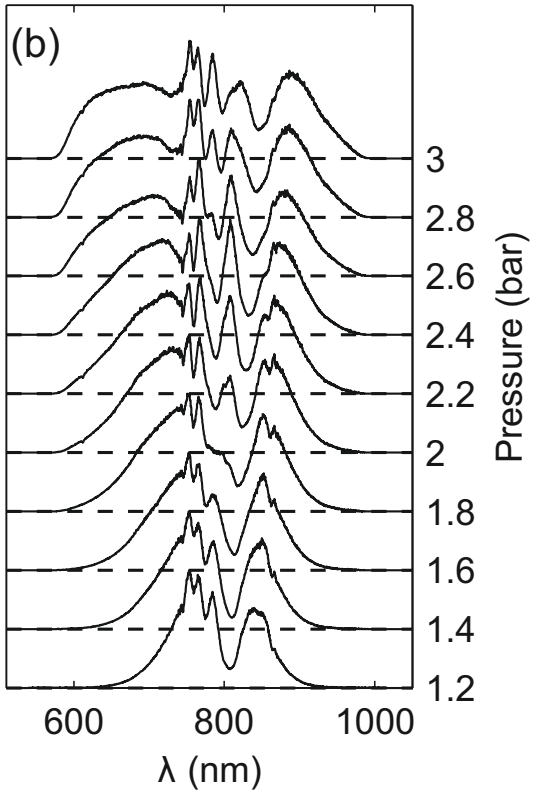

Figure 3.12: Measurements of the spectral amplitude behind HCF in dependence on the gas pressure published by Frank *et al.* [71]. The input laser pulses have a duration of $\tau = 30\,\text{fs}$ and $E = 900\,\mu\text{J}$ per pulse. HCF has a length of $z = 1\,\text{m}$, a bore diameter of $a = 250\,\mu\text{m}$ and is filled with neon gas.

measured in the experiment is not as detailed as the simulated phase and produces a time-frequency plot which is not as finely resolved as for the calculated data.

Comparison with literature

Measurements of the spectral amplitude of a supercontinuum generated by propagation through a hollow-core fiber in dependence on the gas pressure in the fiber have been published in previous works, especially as part of comparisons between the spectra generated by constant gas pressures and differential gas pressures [15, 44]. In Fig. 3.12 the results of Frank *et al.* [71] are shown. The experimental setup is very similar to the one used in our experiment and the parameters for the measurements are nearly the same, which makes these results convenient for a comparison.

Even with a wavelength axis it is observable that the behavior of the central peaks is the same. They remain at a fixed frequency and increase and decrease over a gas pressure range of ca. 1 bar. The side wings shift outwards in frequency with increasing pressure, but show a small region of fast oscillations at a constant frequency on each side of the central frequency.

Gallmann *et al.* report in 2007 in a comparison of pulse properties between few-cycle pulses generated in a hollow-core fiber and those generated by filamentation that

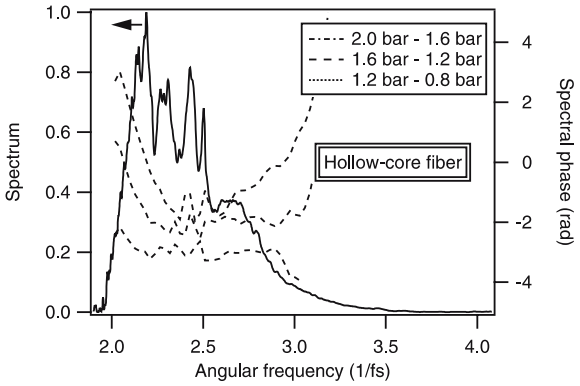

Figure 3.13: Measurements of the spectral phase $\phi(\omega)$ behind a HCF in dependence on the gas pressure published by Gallmann *et al.* [72]. The plotted $\phi(\omega)$ is actually the difference between $\phi(\omega)$ at the respective gas pressure and $\phi(\omega)$ at the next lower pressure. The input laser pulses have a duration of $\tau \simeq 25\,\text{fs}$ and $E = 800\,\mu\text{J}$ per pulse. HCF has a bore diameter of $a = 250\,\mu\text{m}$ and is filled with neon gas. The spectral amplitude is recorded at $p = 2\,\text{bar}$.

the positive GDD of the output spectral phase after the hollow-core fiber increases faster for gas pressures around 2 bar than for low gas pressures around 1 bar [72]. This in regard to gas pressure nonlinear increase of GDD is explained as a manifestation of the increasing self-phase modulation experienced by the intense pulse propagating through the hollow-core fiber. The reported results are illustrated in Fig. 3.13.

However, this effect is not reproduced in the measurements presented here, and neither does it occur in the numerical simulations.

General remarks

In conclusion of chapter 3 it can be stated that the results of the numerical calculation are in qualitative agreement with the results of the experiment. This is in particular true for the spectral amplitude. The agreement of the spectral phase leaves something to be desired yet, though currently it cannot be determined whether this is because of a physical effect and a real loss of detail, or due to a limitation of the SPIDER to resolve fast changes of the spectral phase coupled with a low intensity of the spectral amplitude.

This result justifies the application of the simple 1-dimensional approach and the various assumptions and approximations made both in obtaining the propagation equation (1.62) in chapter 1 and in implementing the nonlinear operator and dispersion operator in chapter 2. It proves that these lead to a model which is sufficiently exact to describe the nonlinear process in our setup, and that the numerical simulation can serve to make valid predictions about the experiment.

4. Results of the Numerical Simulation

In this chapter the numerical simulation is used to study the effects of the input spectral phase on the supercontinuum after the fiber. In the previous chapter this has been executed for gas pressure in the hollow-core fiber and the results of the numerical simulation have been found to be in qualitative agreement with the experiment. Because of that the simulation is able to make valid predictions about the behavior of the experiment and the resulting supercontinuum. It is found that the input spectral phase is a key parameter in formation of the supercontinuum, and that this parameter can be used to manipulate and optimize the properties of the pulses after the hollow-core fiber.

In section 4.1 the effect of the fiber length on the supercontinuum is briefly investigated. In section 4.2 the effect of the input pulses' properties and predominantly of the spectral phase $\phi(\omega)$ on the supercontinuum is studied. It turns out that the input spectral phase is a crucial parameter which determines many of the resulting supercontinuum's features, like its bandwidth or the oscillation of peaks in the spectrum. In section 4.3 this result is applied to optimize the Fourier-transform limited (FTL) pulse duration τ_0 after the hollow-core fiber, since this is the supercontinuum property with the highest importance to our experiment. In section 4.4 finally the predictions about the FTL duration τ_0 are transferred to simulations of the actual pulse duration τ. It is found that by adding a substantial amount of third order dispersion (TOD) to the input spectral phase the pulse duration can likely be decreased by at least 0.3 fs.

The parameters for the numerical simulations are listed in the figure captions. The default parameters are those used in the experiment: input spectral amplitude and phase as in experiment (Fig. 3.4, PrismComp0), $\omega_0 = 2.365\,\mathrm{PHz}$, $E = 830\,\mu\mathrm{J}$ per pulse; hollow-core fiber length $z = 1\,\mathrm{m}$, bore radius $a = 125\,\mu\mathrm{m}$, neon gas. Parameters which are consistently not changed, like central frequency ω_0, pulse energy E, gas type, fiber length z and fiber bore radius a, are usually omitted. While the gas pressure will change so often that no default value is listed here. The carrier or central frequency of the input pulses in the experiment is also used for pulses with a Gaussian spectrum and corresponds to a central wavelength of 797 nm.

4.1. Effects of the hollow-core fiber on the supercontinuum

The length and diameter of the gas-filled hollow-core fiber are important parameters for the setup, and their optimal values depend on the choosen gas, pressure, and input laser intensity [16]. The spectrum of the light pulse continues to broaden while propagating along the length z of the hollow-core fiber, and the numerical simulation makes it possible to examine the characteristics of the laser pulse at each increment of z during propagation. Actually the simulation shows the same change in pulse properties for percental variations of the length z as for variations of the gas pressure p as they are illustrated in Fig. 3.10. Meaning, for a given simulation at gas pressure $p = {}^{p_0}/_2$ and fiber length $z = z_0$, a simulation at $p = p_0$ and $z = {}^{z_0}/_2$ will deliver the same results.

This is to be expected, because it follows from the equations presented in section 2.2.1 that the operator $\hat{N} \propto \gamma_0 \propto n_2 \propto p$, and roughly $\hat{D} \propto \beta_i \propto p$. Only the absorption coefficient α, which is also a part of $\hat{D}$, is not proportional to the gas pressure p, since it is not derived from absorption in the gas, which is negligible, but from reflections inside the hollow-core fiber. From Eq. (2.4) follows that the operators $\hat{N}$ and $\hat{D}$ are incorporated in the numerical simulation as the product of the respective operator with h, which is a small increment of the length z. Hence $h\hat{N}$ and $h\hat{D}$ are directly proportional to both h and p, and it follows that a percentual change in z has the same consequences as a corresponding change in p. At least inside the limitations of this relative simple model for pulse propagation.

In Fig. 4.1 the change of the Fourier-transform limited (FTL) duration τ_0 of the pulse, which is directly retrieved from the spectral amplitude, is illustrated for three different input pulses during propagation through the hollow-core fiber. The three investigated pulses are an input pulse as measured in the experiment (black line), a pulse with the same spectral amplitude but with a spectral phase of $\phi(\omega) = 0$ (red line), and a Gaussian pulse with a narrower spectral amplitude and a spectral phase $\phi(\omega) = 0$, but with the same pulse duration as the pulse from the black line (green line). For curiosity's sake the change of the central frequency ω_0 is also plotted. It is evident that due to self-steepening, which favors the generation of new frequencies on the blue side of the spectrum, the central frequency ω_0 is subject to a steady increase during propagation through the fiber.

In the black curve kinks or abrupt steps of the gradient in the evolution of the FTL pulse duration τ_0 are observable, as for example at $z \simeq 47\,\text{cm}$. Since the step size h is 5 mm this is not due to a lack of data points. Rather these steps agree with a observation made in section 3.5.3, that the spectrum does not evolve continuously but in steps. While this observation has been made for the dependency of the spectrum on the gas pressure p, it follows from the discussion above that a dependency on the fiber length z has to show the same behavior. Indeed the sudden increases of the high frequency side wing of the spectrum in Fig. 3.10 roughly correspond with the

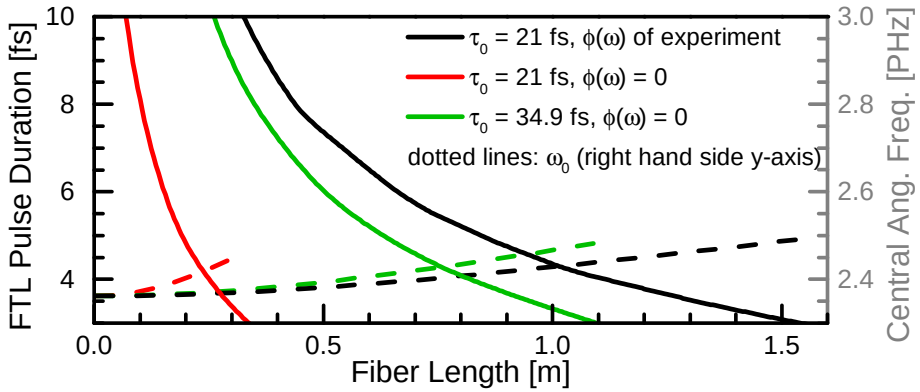

Figure 4.1.: Calculation of FTL pulse duration τ_0 during propagation inside HCF for three different input pulses. The first input pulse is a Gaussian with $\tau_0 = 21\,\text{fs}$ and a spectral phase equal to zero (red), the second is a Gaussian with $\tau_0 = 34.9\,\text{fs}$ and a spectral phase equal to zero (green), and the third a Gaussian with $\tau_0 = 21\,\text{fs}$ and a spectral phase as measured in the experiment. The dotted lines belong to the y-axis on the right hand side and are the respective values for the central frequency ω_0. (Parameters: $p = 3\,\text{bar}$)

gradient steps of the black curve in Fig. 4.1, which serves to explain the latter.

As can be gathered from the black curve, the pulse in the experiment is not achieving as broad a supercontinuum as it could after propagating 1 m in the gas-filled hollow-core fiber. However, the limitations of the pressure chamber make an increase of fiber length or a further increase of gas pressure difficult, and the input laser power is already at the maximum the laser system can provide. A more viable approach would be to fabricate a smoother spectral phase $\phi(\omega)$ for the input pulse and decrease pulse duration in this way.

The red curve illustrates the FTL pulse duration τ_0 for an input pulse with a spectral amplitude as in the experiment but with a spectral phase equal to zero. It is evident that in this case gas pressure would have to be decreased considerably to achieve an appropriate FTL duration after a propagation distance of 1 m.

The green curve illustrates an input pulse with a spectral phase equal to zero but with a decreased spectral bandwidth. It has the same pulse duration in front of the hollow-core fiber as the pulse of the black curve, and yet its FTL pulse duration τ_0 is notably shorter than it is for the black curve.

It follows that the spectral phase of the input pulse is an important parameter for the generation of a supercontinuum, and not only insofar that it determines the pulse duration of the input pulse. This is further investigated in the next section.

4.2. Effects of the input laser pulse on the supercontinuum

The output of the numerical calculation is determined by the input beam, its power, spectral amplitude and spectral phase. In Fig. 4.2 the simulation results for three different input pulses are shown. The first is the pulse as measured in the experiment, including spectral amplitude (black curve) and group delay (blue curve). The second is a Gaussian pulse with a bandwidth equivalent to a FTL pulse duration of $\tau_0 = 21\,\mathrm{fs}$ (green curve) with a spectral phase as measured in the experiment. The third illustrated input pulse is a Gaussian with reduced bandwidth and a Fourier-limited pulse duration $\tau_0 = 34.9\,\mathrm{fs}$ (red curve), with a spectral phase equal to zero. The frequency bandwidths of the respective Gaussian pulses are chosen such that all three input pulses have the same pulse duration $\tau = 34.9\,\mathrm{fs}$.

One of the objectives of the simulations presented in Fig. 4.2 is to determine and compare the roles of the input spectral amplitude and phase. The effect of the input spectral amplitude can be estimated by means of the first two curves, which have the same spectral phase but a different spectral amplitude. While the latter two curves both have a Gaussian spectral amplitude but different spectral phases, and hence are used to estimate the effect of the input spectral phase.

As is observable in Fig. 4.2 c) the differences in spectral amplitude between the black (spectral amplitude of experiment) and the green (Gaussian spectral amplitude) input pulse make nearly no difference for the result of the calculated hollow-core fiber output. In the calculated group delay the only notable difference is the behavior at the fringes on both sides. The group delay of the green curve shows strong oscillations in the fringes, despite the green curve having the same input spectral phase and a smoother input spectral amplitude than the black curve.

In comparison the bandwidth-limited curve (red), which has the same pulse duration at entry into the hollow-core fiber as the two other pulses but a very different spectral phase, shows a quite different behavior. The resulting spectrum is both broader and less perturbed by oscillations, and the latter effect is also very notable in the group delay. Due to the increase in bandwidth this pulse has a much shorter FTL pulse duration, and due to the overall smoother phase it is easier to compress.

In comparison of the Wigner plots in Fig. 4.2 e) and f) the consequences of the different input spectral phases $\phi(\omega)$ are demonstrated. For the input pulse with a spectral phase of the experiment (green curve) a considerable part of the pulse energy after the hollow-core fiber is bound in side pulses in front and after the main pulse, while the input bandwidth-limited pulse (red curve) shows no apparent side pulses at all. The difference in generated bandwidth is also apparent in the Wigner plots. From the gradient of the high $\mathcal{W}(t,\omega)$ band can be discerned that the pulse with the spectral phase of the experiment (green curve) has a greater amount of GDD than the bandwidth-limited pulse (red curve). Further simulations yield that the pulse with the spectral phase as measured (green curve) needs -36 fs^2 GDD and +32 fs^3 TOD for

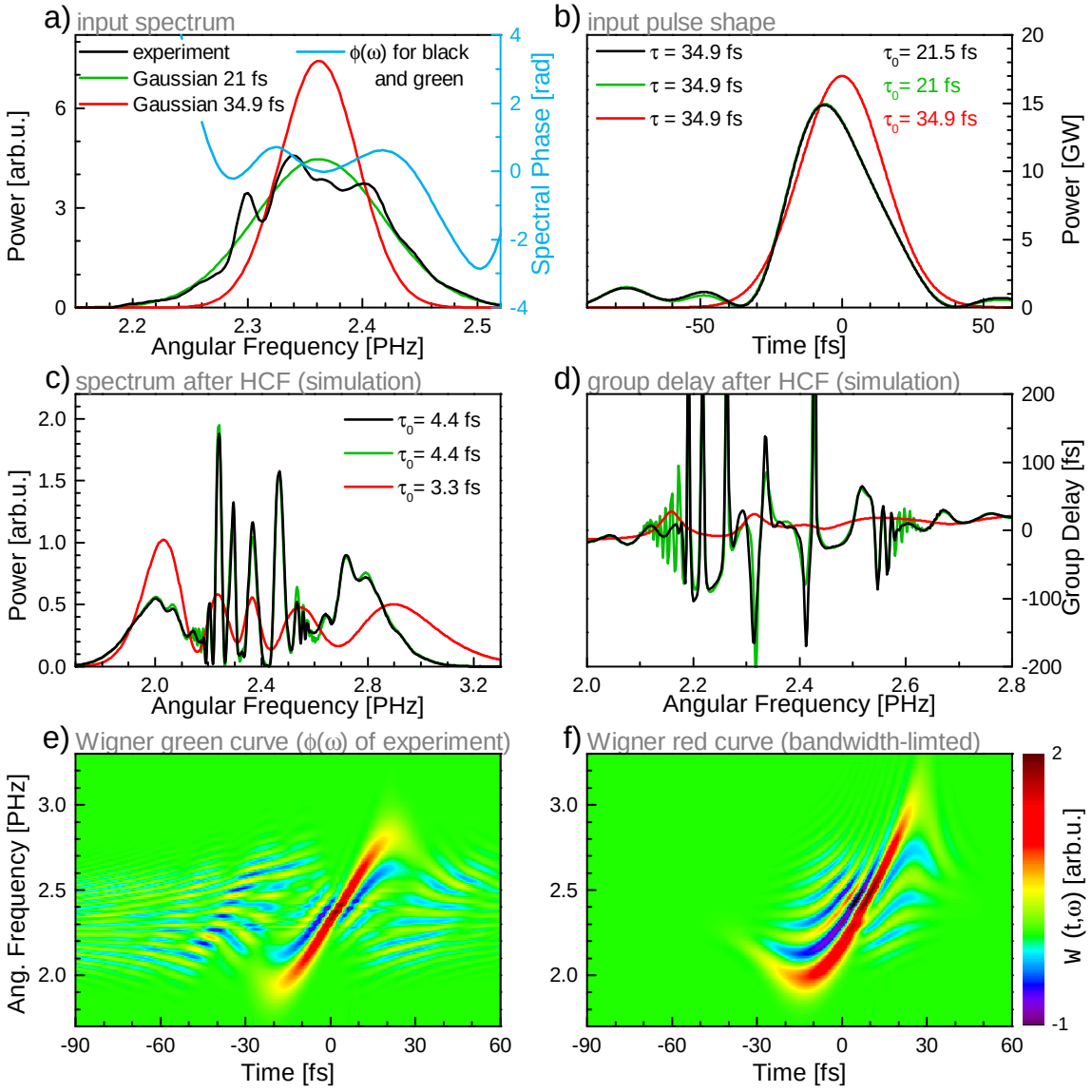

Figure 4.2.: Simulation results after HCF for three different input pulses. Parameters: spectral amplitude and phase as in experiment (black), Gaussian with $\tau_0 = 21\,\mathrm{fs}$ and spectral phase as measured in experiment (green), and Gaussian with $\tau_0 = 34.9\,\mathrm{fs}$ and spectral phase of zero (red). All three pulses have the same pulse duration $\tau = 34.9\,\mathrm{fs}$. In a) the spectral amplitude $P(\omega)$ (normed to energy per pulse) and spectral phase $\phi(\omega)$ of the input pulses are shown, in b) the temporal pulse shape $P(t)$, in c) the calculated spectrum after the HCF, in d) the calculated group delay after the HCF, and e) and f) show the Wigner plots of the pulses represented by the green and red curves respectively.
(Parameters: $p = 3\,\mathrm{bar}$)

optimal compression and the bandwidth-limited pulse (red curve) only -30 fs^2 GDD and +19 fs^3 TOD. With this dispersion values both pulses are compressed nearly down to their respective Fourier-transform limit.

For these comparisons the green and the red curve have been chosen because both have a Gaussian input spectral amplitude, if with different bandwidths, and the dominant difference between both pulses is the spectral phase $\phi(\omega)$. The conclusion is that the spectral phase of the input pulse is a critical parameter in the generation of new frequencies and not only insofar as it determines the duration of a pulse, which has been the same for all three exemplary pulses. The simulations of Fig. 4.2 show that an input laser pulse with a smooth spectral phase is advantageous for the generated supercontinuum even if the input pulse duration remains unchanged. This observation is investigated further in the next section.

4.2.1. Input pulse spectral phase

To further investigate the impact of the input pulse's spectral phase on the properties of the supercontinuum after the hollow-core fiber, simulations of the pressure-dependent spectral amplitude and group delay like they are presented in chapter 3 are studied. The three prism compressor settings illustrated in Fig. 3.4 on page 62 are chosen to set the input spectral phase for three simulations. In Fig. 4.3 the results are shown, which are quite different from each other despite only minor differences in the respective input spectral phase. As a reference the results for a Gaussian input pulse with a spectral phase equal to zero are also depicted.

In comparison to plot b), which shows the same data already presented in Fig. 3.10 c), plot a) has an increased bandwidth and slightly less pronounced oscillations in the spectral amplitude. It does not show the prevalence of negative odd order dispersion as plot b) does, expressed in the increased intensity of its high frequency sidewing and its rupture into different peaks, but rather a prevalence of even order dispersion. The effects of even and odd order dispersion on a pressure-dependent spectrum plot are further illustrated in Fig. 4.4.

Fig. 4.3 c) has a decreased bandwidth and shows pronounced oscillations in the spectral amplitude, especially in the side wings. The influence of even order dispersion is supressed in favor of the odd terms. The gas pressure range in which the peaks remain constant are longer and have an offset in pressure in comparison to a) and b). This is due to the increased input pulse duration and reduced instantaneous power, which makes the nonlinear process overall less efficient.

Fig. 4.3 d) shows the calculation for an input pulse with a spectral phase of zero. It is notable different from the other three calculations, with more intensity in the side wings of the spectrum and very minor oscillations in the center. Both the spectral amplitude and the spectral phase evolve smoothly in dependence on the gas pressure, without the stepwise evolution observable in the plots a) to c).

From this follows that the form of a supercontinuum spectrum after frequency

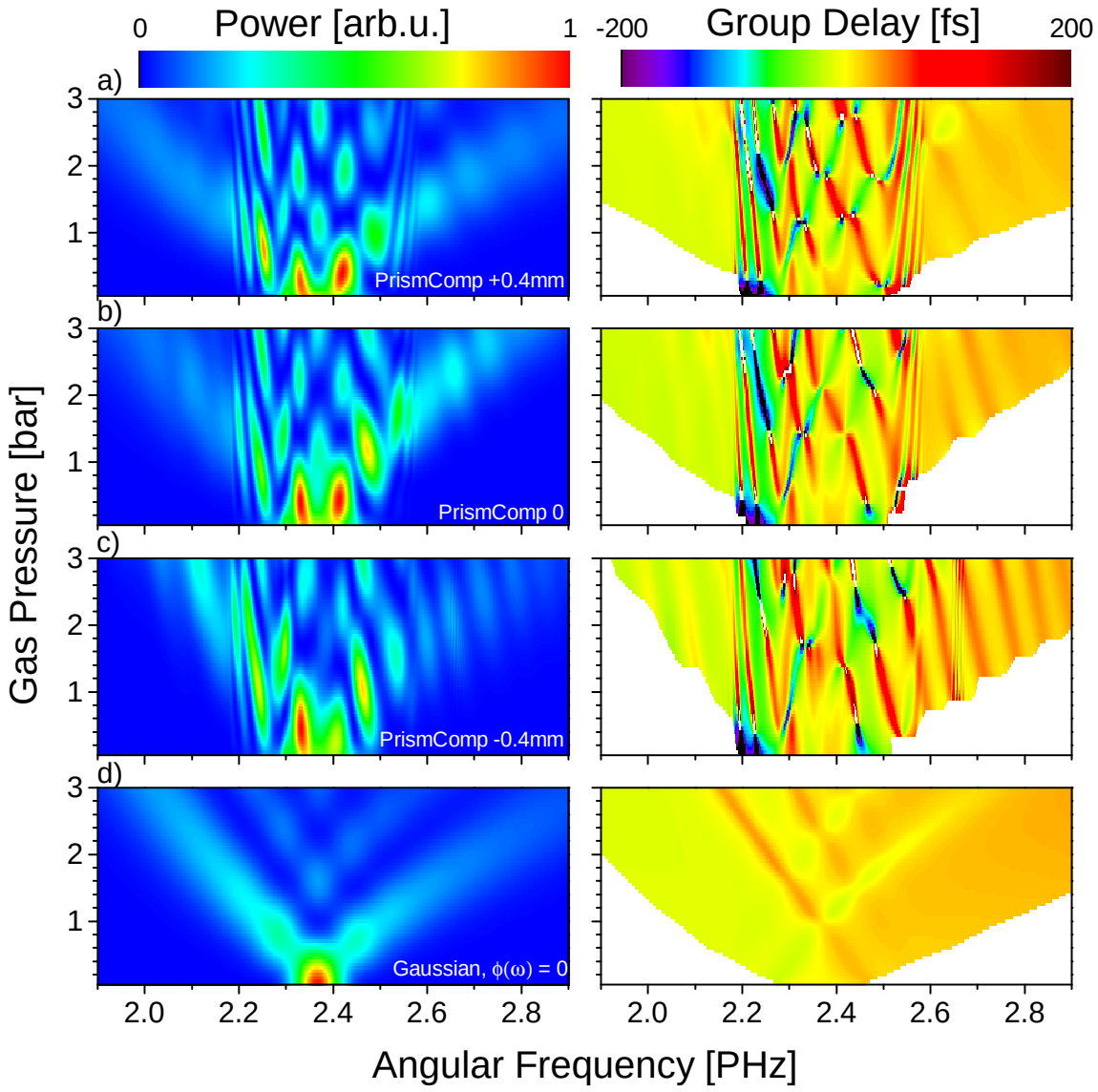

Figure 4.3.: Calculated spectral amplitude $P(\omega)$ and group delay for four different input pulses in dependency of the gas pressure in HCF. Input pulses of a) to c) are taken from measurements Fig. 3.4. The PrismComp value stands for three different settings of the prism compressor in front of the HCF. The data for b) are the same as in the bottom row of Fig 3.10. In d) the input pulse is a Gaussian with pulse duration $\tau_0 = 35\,\mathrm{fs}$ and a spectral phase $\phi(\omega) = 0$.

generation in a hollow-core fiber, with its well known oscillations, is predominantly determined by the spectral phase of the input pulse. This permits to assess the spectral phase of the input pulse by studying the spectrum of the pulse after the hollow-core fiber and especially its pressure-dependent evolution. Even more important, this opens the possibility to manipulate and optimize the spectrum of the supercontinuum by manipulating the input spectral phase of the laser pulse in front of the hollow-core fiber, for example with chirped mirrors.

Before the latter is discussed in section 4.3, the effects of the different Taylor series expansion coefficients of the spectral phase are briefly investigated.

Effects of different expansion coefficients of the spectral phase

In Fig. 4.4 the effects of coefficients of the spectral phase $\phi(\omega)$ up to the 5th order on a pressure-dependent pseudocolor spectrum plot are illustrated. As demonstrated in the discussion of Fig. 4.3 above this can be useful in comparisons of such plots. The exact value of the input spectral phase in Fig. 4.4 is chosen such in each case that the Fourier-transform limited (FTL) pulse duration after the hollow-core fiber is $\tau_0 = 4.5\,\mathrm{fs}$ at $p = 3\,\mathrm{bar}$, and the spectral amplitudes have a comparable bandwidth.

In the case of group delay dispersion (GDD) it is apparent that a FTL pulse duration of 4.5 fs can be achieved with a bit more positive GDD than negative GDD. This means that input negative GDD is more disadvantegous to the spectral bandwidth than positive GDD. This is an established phenomenon [73]. Negative GDD means that the pulse is down-chirped, or that the high frequencies are at the pulse front and the low frequencies at the pulse's trailing edge. However, SPM creates new frequencies with lower energy than the central frequency at the pulse front and with higher energy at the pulse's trailing edge. Hence the spectrum of a pulse with negative GDD does not gain new frequencies by SPM, and indeed the spectral bandwidth decreases at first as the frequencies in the pulse are averaged out. Only when SPM has cancelled the previous down-chirp of the pulse it begins to increase the spectral bandwidth of the pulse again.

In addition to that change in efficiency Fig. 4.4 demonstrates another significant difference on the consequences of positive and negative GDD. For a pulse with positive GDD the peaks of the spectral amplitude shift continuously apart with increasing gas pressure. Or during propagation in the hollow-core fiber, since it has been shown at the start of this chapter that the changes of the pulse spectrum in regard to gas pressure are the same as in regard to propagation distance. For an input pulse with negative GDD however the central peaks in the spectral amplitude remain at the same frequency while the gas pressure increases. New peaks come into existence, increase in amplitude and then decrease and vanish again, without a shift in frequency. Only the side wings of the spectrum show a continuous shift like it is the case for an input pulse with positive GDD.

The plots for third order dispersion (TOD) in Fig. 4.4 clearly demonstrate the

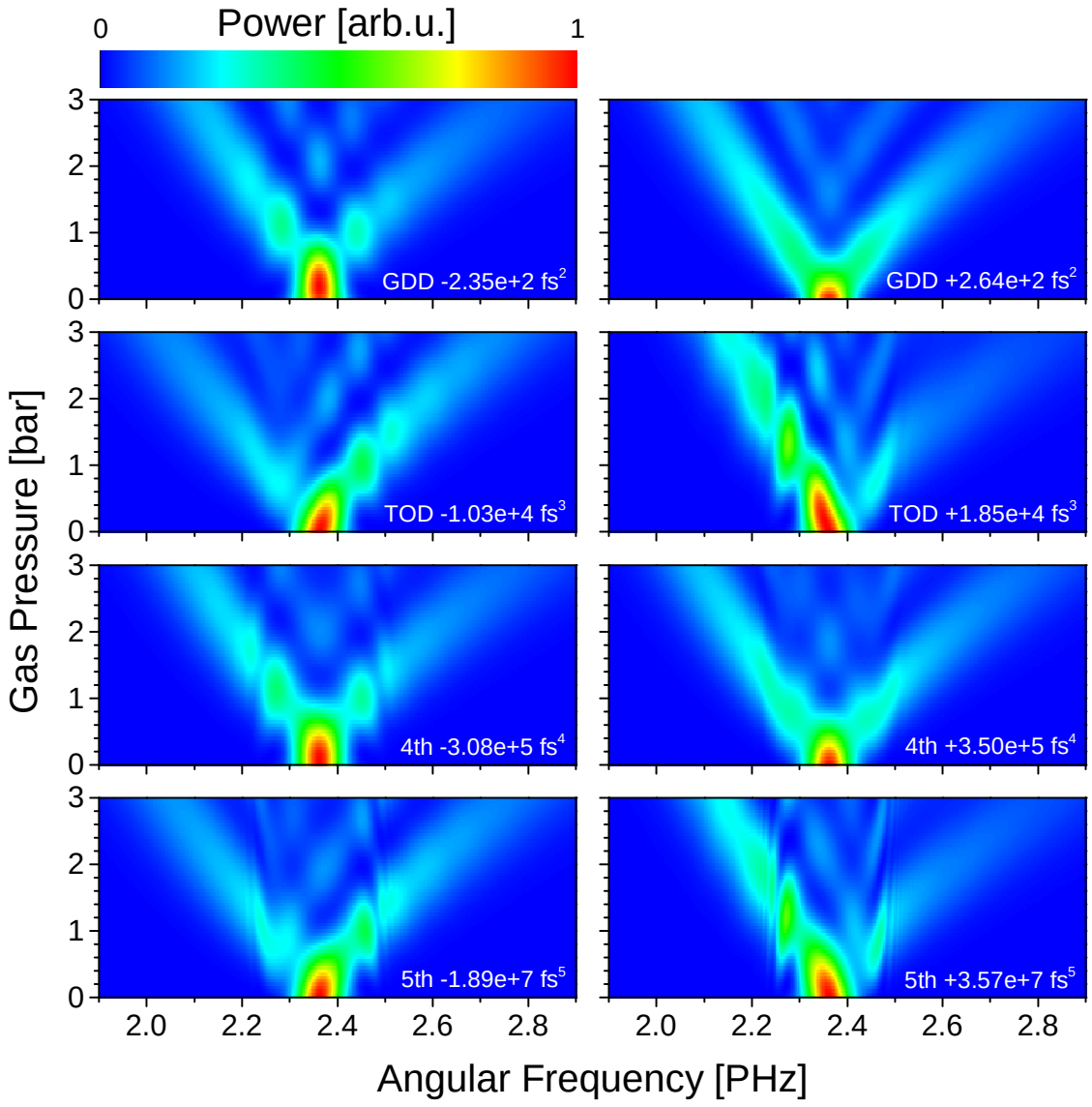

Figure 4.4.: Calculated pressure-dependent spectrum plots for negative and positive coefficients of the spectral phase $\phi(\omega)$ up to the 5th order. The respective values of $\phi(\omega)$ are chosen such that at 3 bar the spectral amplitude has a FTL pulse duration $\tau_0 = 4.5\,\mathrm{fs}$. A plot with $\phi(\omega) = 0$ is depicted in Fig. 4.3 d).
(Parameters: input Gaussian pulse $\tau_0 = 35\,\mathrm{fs}$)

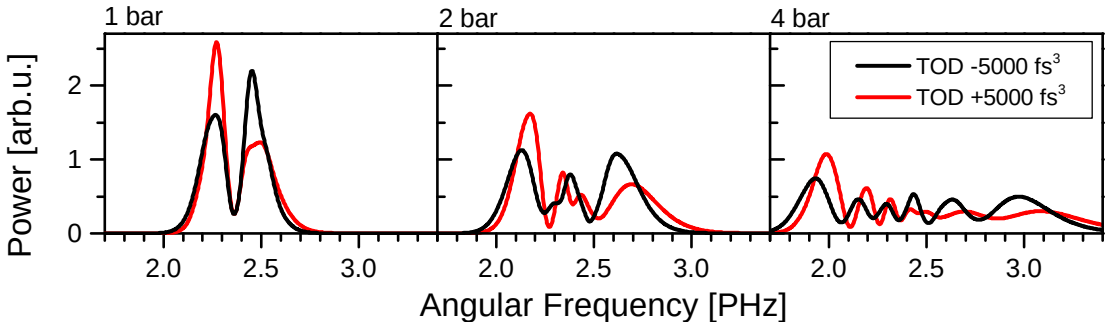

Figure 4.5.: Simulation of the spectral amplitude after the HCF for input pulses with $\phi(\omega) = \pm 5000\,\mathrm{fs}^3$ TOD, at three different gas pressures, for comparison of the peak ratios.
(Parameters: input Gaussian pulse $\tau_0 = 35\,\mathrm{fs}$)

asymmetric nature of the effects of TOD on the supercontinuum. An input pulse with negative TOD shows a significant increase in the spectral amplitude for high frequencies, while a pulse with positive TOD favors low frequencies. It has been shown in section 2.2.3 that self-steepening is responsible for a similar asymmetry by making the pulse trailing edge steeper, and hence causing SPM to work more efficiently for the pulse trailing edge and the high frequencies located there. This causes the high frequency peaks in the spectral amplitude to become broader and hence lower in amplitude, and the low frequency peaks to become narrower but higher in amplitude. TOD in the input pulse works in a similar way by changing the gradient of the pulse slopes and hence the efficiency at which SPM generates new frequencies. Positive TOD increases the gradient in the pulse trailing edge and works in the same direction as self-steepening, broadening the high frequency peaks and causing the low frequency peaks to be narrower and higher in amplitude. This is illustrated in Fig. 4.4. For negative TOD the opposite effect is observed at first and the high frequency peaks become narrow and show an increased amplitude. This effect is reduced by the onset of self-steepening however, and the peaks for high and low frequencies then show similar widths and amplitude heights. With increasing gas pressure self-steepening becomes dominant and the low frequency peaks are again narrower and have a higher amplitude than the high frequency peaks. This is illustrated in Fig. 4.5. For comparison the results for both positive and negative TOD are shown, and the supercontinuum for an input pulse with positive TOD does not display this reversal in peak ratio since its effect is already working in the same direction as the effect of self-steepening.

In the TOD plots of Fig. 4.4 it is also obvious that, same as for GDD, a FTL pulse duration of 4.5 fs can be achieved with a larger amount of positive TOD than negative TOD. This is only to be expected, since previous simulations have shown that self-steepening has an advantageous effect on the supercontinuum bandwidth.

Negative TOD in the input pulse counters this and is hence more disadvantageous to the bandwidth than positive TOD.

The 4th order dispersion plots of Fig. 4.4 show traits which resemble those the GDD plots, and the plots for 5th order dispersion resemble those for TOD. It is to be expected that the different even order coefficients in the Taylor expansion of the spectral phase $\phi(\omega)$ are similar in their effect on the supercontinuum, and so are the effects of the respective odd order coefficients. A notable difference is the appearance of very fast oscillations at roughly 2.25 and 2.5 PHz. These oscillations increase with the coefficient order, and they are also observable in the simulation of Fig. 3.10 c).

The unfortunate double peak form of the spectral phase in our experiment and the necessity to use high order coefficients in the Taylor expansion to reproduce this phase have already been demonstrated and discussed in section 3.2. However, simulations show that the result of a pressure pseudocolor plot like in Fig. 4.3 is very sensitive to the input spectral phase. If such a plot is measured in an experiment it is conceivably possible to reconstruct the input spectral phase from it with an appropriate algorithm, if it can be demonstrated that the correlation between input spectral phase and pressure pseudocolor plot is unambiguous. Of course this is only a useful option if a SPIDER or another phase measurement device is not readily available, or if the spectral amplitude of the supercontinuum has so extensive minima that the spectral phase cannot be retrieved by the SPIDER algorithm.

4.2.2. Input pulse spectral amplitude

In the previous section the effects of the input pulse's spectral phase on the properties of a supercontinuum after a hollow-core fiber have been discussed in detail. In Fig. 4.2 on page 85 it has already been demonstrated that small deviations from a Gaussian pulse in the spectral amplitude make no difference for the calculation and provide the same result as for a Gaussian spectral amplitude. In this section it is investigated whether big changes in the spectral amplitude of the input pulse can have effects on the supercontinuum similar to the effects of the spectral phase which have already been demonstrated.

It is observable in Fig. 3.10 that the single peak of the input spectral amplitude separates instantly into a double peak even at low preasures and very weak self-phase modulation. This is a consequence of the double peak in the input spectral phase $\phi(\omega)$. Simulations demonstrate that a very similar pressure-dependent spectrum plot can be achieved with an input spectral phase equal to zero, if the input spectral amplitude already consists of two peaks before entering the hollow-core fiber. This is illustrated for three different examples in Fig. 4.6.

The pressure-dependent pseudocolor spectrum plots for these input pulses with a double peak in the spectral amplitude show a similar behavior of the spectral amplitude after the hollow-core fiber as the pulses with a double peak in the input

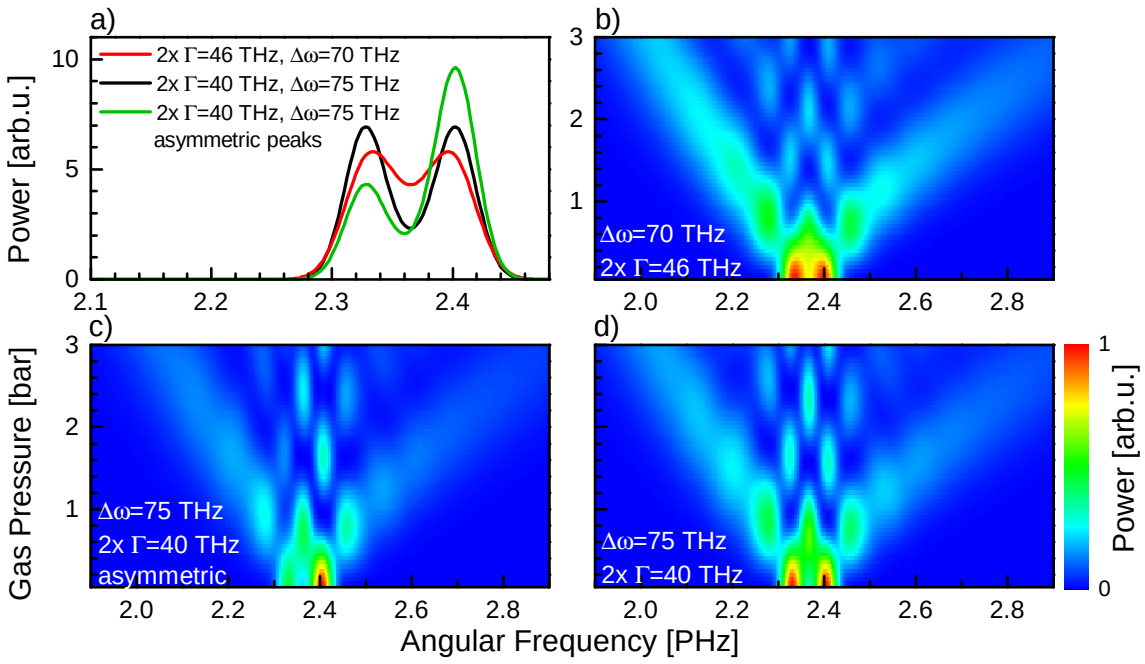

Figure 4.6.: Calculation of the pressure-dependent spectrum $P(\omega, p)$ after the HCF with an input spectrum of double Gaussian peaks. In a) three different input spectra are depicted. The two symmetric spectra have a different peak bandwidth and distance between peaks, which are chosen to result in the same Fourier-limited pulse duration for the double peak. In b) to d) $P(\omega, p)$ is shown. The peak ratio for the asymmetric spectrum is 1:1.5 for the field amplitude or 1:2.25 for the power.
(Parameters: input spectral phase $\phi(\omega) = 0$)

spectral amplitude in Fig 3.10, both for the central peaks as for the side wings. In comparison between Fig. 4.6 b) and d) it is apparent that an increase in modulation of the input spectral amplitude peaks results in sharper defined peaks in the spectral amplitude after the hollow-core fiber. Plot c) demonstrates the calculation results for a spectrum with asymmetric peaks, and on the side of the low input peak all peaks in the resulting spectral amplitude are reduced in intensity.

It follows that manipulation of the input spectral amplitude of the laser pulses in front of the hollow-core fiber can have a similar effect like manipulation of the spectral phase. The investigation in this section is only done in the form of a few examples though and is in no way meant as comprehensive.

4.3. Optimization of the supercontinuum with the input spectral phase

In a publication from 2008 Winterfeldt *et al.* investigate the application of temporal and spatial pulse shaping to ultra short laser pulses after a hollow-core fiber to control the characteristics of high harmonic radiation generated with these pulses [74]. For this they employ a pulse shaper realised with a deformable mirror to manipulate the spectral phase of the laser pulses between the exit of the hollow-core fiber and the gas target for high harmonic generation.

It has been demonstrated in section 4.2.1 that the input spectral phase $\phi(\omega)$ of the laser pulses in front of the hollow-core fiber can also be used to manipulate the properties of the pulses after the fiber. While this approach naturally cannot achieve the fine control provided by a pulse shaping device, it is implemented earlier in the beamline and is not accompanied by the inherent limitations of a pulse shaper in regard to pulse duration and power. The optimization of high harmonic generation (HHG) through control of the spectral phase in front of the hollow-core fiber is a potentially promising application.

The supercontinuum property which is of greatest importance for HHG and the isolation of attosecond pulses is the pulse duration. In this section it is investigated with numerical simulations to which extend the bandwidth of the supercontinuum can be optimized with the input spectral phase, first for a spectral phase near to zero and then for a spectral phase as used in the experiment.

The optimized quantity is the Fourier-transform limited (FTL) pulse duration τ_0 of the supercontinuum, which ought to be as short as possible. It is defined as the full width half maximum (FWHM) of the temporal pulse shape for a bandwidth-limited pulse, meaning for a spectral phase $\phi(\omega) = 0$.

The influence of an input spectral phase on an output supercontinuum has already been investigated for several applications. In a study of the shot-to-shot stability of several pulse parameters in front of and after a hollow-core fiber measurements of

the output pulse duration in dependence on a linear input chirp (GDD) have been reported [75].

Solitons are pulses which propagate through optical fibers with anomalous dispersion without changing their pulse shape, and they can be transmitted over long distances through optical fibers if they are amplified in periodic distances. It has been found that the distance at which amplification is necessary can be increased when the input pulses exhibit positive GDD [76].

Intense few-cycle pulses generated through self-filamentation in a noble gas atmosphere instead by propagation through a gas-filled hollow-core fiber are a broad field of study, and it has been found that for such pulses the shortest output pulse after compression is not achieved with the shortest input pulse, but with a positive input GDD [77]. It has recently been reported that it is even possible to achieve self-compression of few-cycle pulses generated by self-filamentation with the application of positive input GDD [78].

However, these studies concern themselves nearly exclusively with a quadratic input spectral phase, also referred to as a linear chirp, and with supercontinua which are not generated by propagation through a gas-filled hollow-core fiber.

4.3.1. Nearly bandwidth-limited pulse

Eq. (1.64) states that the generation of new frequencies scales with the derivative of the pulse intensity with respect to time. Since a bandwidth-limited pulse with a spectral phase equal to zero has the shortest duration which is attainable for a pulse with a given spectral amplitude, it is intuitive to assume that such an input pulse will result in the broadest possible supercontinuum after propagation through a hollow-core fiber.

However, the numerical calculations show that positive TOD in front of the hollow-core fiber can actually slightly reduce the Fourier-transform limited (FTL) pulse duration of the pulse after the hollow-core fiber. This effect is illustrated in Fig. 4.7. With a Gaussian input pulse which has a FTL pulse duration of $\tau_0 = 30\,\mathrm{fs}$ and $E = 830\,\mu\mathrm{J}$ per pulse at a central frequency $\omega_0 = 2.36\,\mathrm{PHz}$, and a hollow-core fiber of $z = 1\,\mathrm{m}$ length and $a = 125\,\mu\mathrm{m}$ radius filled with neon gas at $p = 2\,\mathrm{bar}$, the simulation predicts that the shortest pulse after the fiber is achieved with an input spectral phase of $+2000\,\mathrm{fs}^3$ third order dispersion (TOD). The difference in duration to an input bandwidth-limited pulse is only small though, with about $\Delta\tau_0 \simeq 0.1\,\mathrm{fs}$.

The TOD required to achieve the shortest possible FTL pulse duration after the hollow-core fiber depends on the characteristics of the input laser pulse and the settings of the hollow-core fiber. Fig. 4.8 demonstrates that in the case of an input Gaussian with a FTL pulse duration of $\tau_0 = 50\,\mathrm{fs}$ the optimal TOD scales nearly linear with the gas pressure p, for example.

The reason for this positive consequence of TOD in the spectral phase of the input pulse is the interplay between TOD, self-steepening and self-phase modulation (SPM) which has already been commented on in the discussion of Fig. 4.4. A correct amount

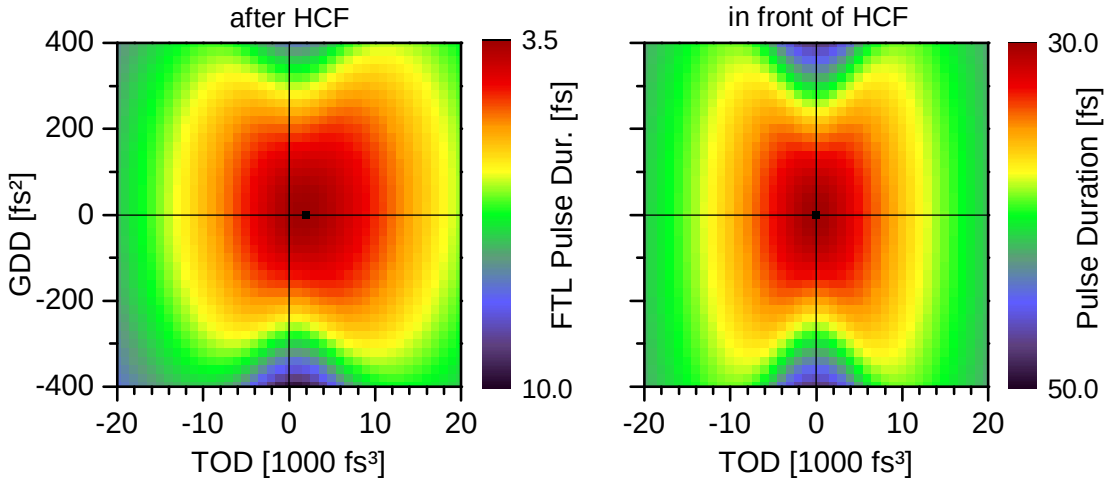

Figure 4.7.: Left-hand side: simulation of the FTL pulse duration τ_0 after propagation through HCF in dependence on GDD and TOD in front of HCF for a nearly bandwidth-limited pulse. Right-hand side: pulse duration τ of the input pulse in front of HCF. The black lines mark an input spectral phase with GDD or TOD equal to zero. The input spectral phase resulting in the shortest pulse duration is marked with a black dot.
(Parameters: input Gaussian pulse $\tau_0 = 30\,\mathrm{fs}$, $p = 2\,\mathrm{bar}$)

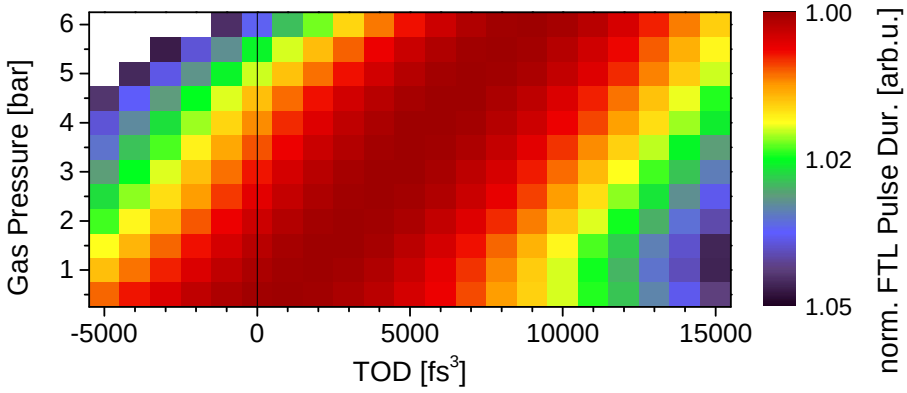

Figure 4.8.: Simulation of FTL pulse duration τ_0 after propagation through HCF in dependence on gas pressure and TOD in front of HCF. FTL pulse duration is normalized to the shortest duration in each row.
(Parameters: input Gaussian pulse $\tau_0 = 50\,\mathrm{fs}$)

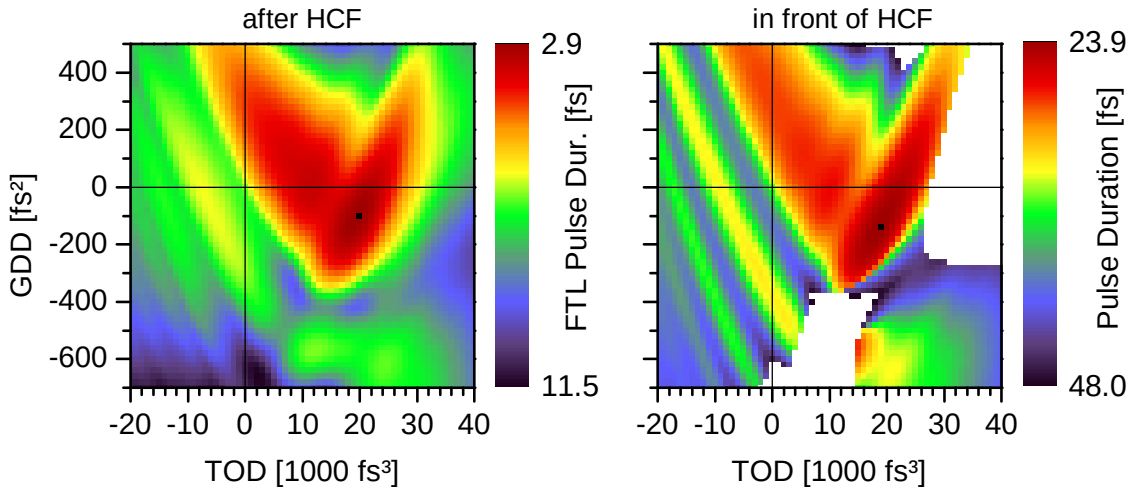

Figure 4.9.: Left-hand side: simulation of FTL pulse duration τ_0 after propagation through HCF in dependence on GDD and TOD in front of HCF for a pulse with a spectral phase as in experiment (PrismComp0, Fig. 3.4). Right-hand side: pulse duration τ of the input pulse in front of HCF. In white areas τ is beyond the scale because of double peaks making the FWHM method to determine pulse duration impractical. The black lines mark the original input spectral phase without additional GDD or TOD. The input spectral phase resulting in the shortest pulse duration is marked with a black dot.
(Parameters: input spectral amplitude and phase as in experiment (Fig. 3.4, PrismComp0), $E = 830\,\mu\text{J}$ per pulse, neon gas at $p = 1.8\,\text{bar}$)

of positive TOD increases the advantegous effect of self-steepening on the generation of new frequencies due to SPM. Simulations without the self-steepening term do not show this behavior and have a minimum FTL pulse duration after the hollow-core fiber for an input pulse with no TOD.

4.3.2. Pulse with a spectral phase of the experiment

The potential for optimizing a nearly bandwidth-limited pulse is certainly of academic value, but of immediate interest for any experiment is the optimization of the pulses available in that experiment. Fig. 4.9 shows the simulation results for the FTL pulse τ_0 duration after the hollow-core fiber if the input spectral phase $\phi(\omega)$ is varied around a phase as measured in our experiment instead of a nearly bandwidth-limited pulse. As starting spectral phase the measurement for the default prism compressor setting (PrismComp0) illustrated in Fig. 3.4 is chosen.

Due to the double peak form of the input spectral phase, variations of GDD and TOD of the input phase result in several local minima of the FTL pulse duration

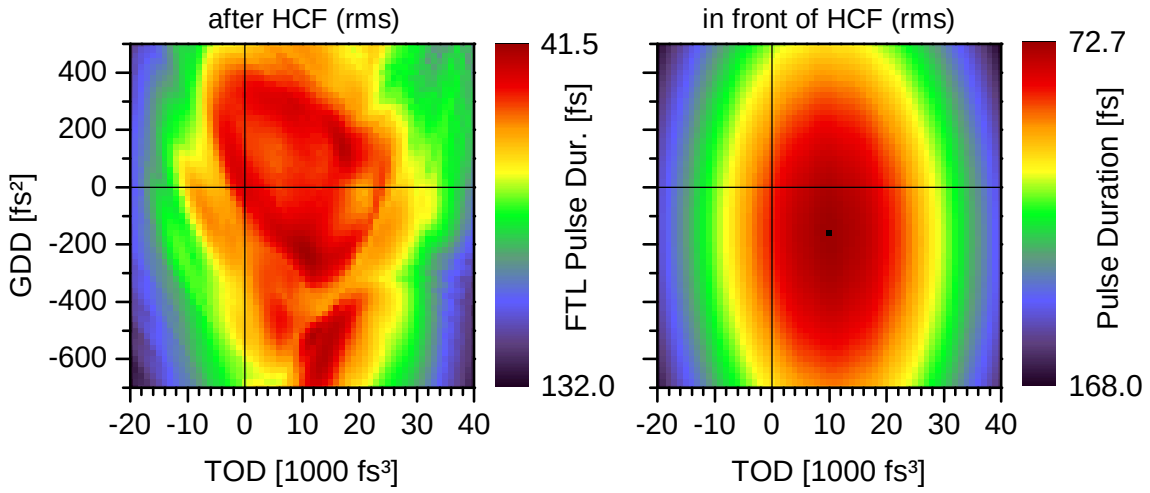

Figure 4.10.: Standard deviation pulse duration τ_σ in dependence on additional GDD and TOD in front of HCF for a pulse with input spectral phase as in the experiment. Left-hand side: simulation of FTL τ_σ after propagation through HCF. Right-hand side: τ_σ (not FTL) of the input pulse in front of HCF, and input spectral phase describing the shortest pulse is marked with a black dot. The black lines mark the original input spectral phase without additional GDD or TOD.
(Parameters: input spectral amplitude and phase as in experiment (Fig. 3.4, PrismComp0), $E = 830\,\mu\text{J}$ per pulse, neon gas at $p = 1.8\,\text{bar}$)

τ_0 after the hollow-core fiber which would be difficult to find experimentally. A comparison with the pulse duration τ in front of the hollow-core fiber reveals that short FTL pulse durations after the fiber tend to occur with short pulse durations in front of the fiber, even if the two plots are not in complete agreement and areas with notable differences exist. At conditions as in the experiment, with exception of the gas pressure which is reduced to $p = 1.8\,\text{bar}$ to prevent the onset of pulse collapse in the calculation, the shortest possible FTL pulse duration in the simulation is achieved with an additional $-100\,\text{fs}^2$ GDD and $+20\,000\,\text{fs}^3$ TOD in front of the hollow-core fiber. In comparison to the original spectral phase at the reduced gas pressure of 1.8 bar, this more than halves the FTL pulse duration τ_0 from 6.7 fs to 2.9 fs.

The standard deviation pulse duration τ_σ

The right-hand side of Fig. 4.9 illustrates that the FWHM method of determining pulse durations is at its limits for pulses with the depicted spectral phase. Fig. 4.10 demonstrates how the same plots look if instead of the FWHM pulse duration τ the standard deviation pulse duration τ_σ introduced in section 1.1.3 is used.

The left-hand side of Fig. 4.10 makes it clear that the standard deviation pulse

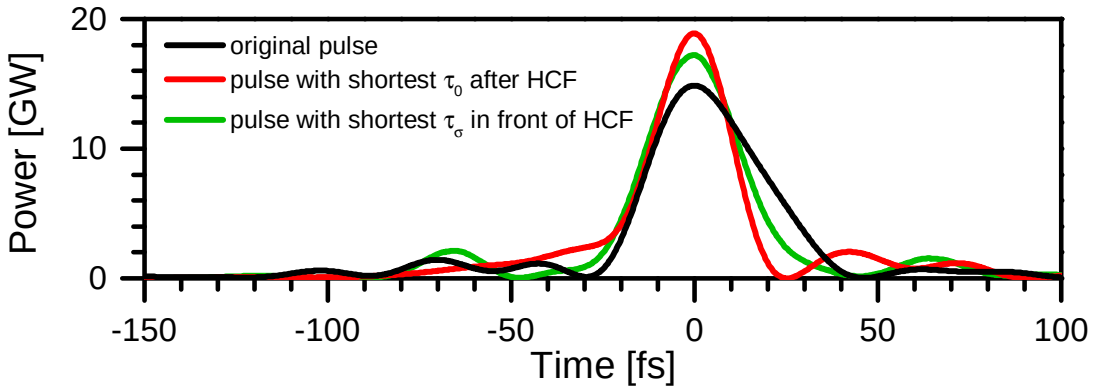

Figure 4.11.: Reconstructed pulse shapes in front of HCF. The original pulse as measured with the SPIDER (black), the original pulse with an additional $-100\,\mathrm{fs}^2$ GDD and $+20\,000\,\mathrm{fs}^3$ TOD to achieve the shortest possible FWHM FTL duration τ_0 after HCF (red), and the original pulse with an additional $-160\,\mathrm{fs}^2$ GDD and $+10\,000\,\mathrm{fs}^3$ TOD to achieve the shortest standard deviation duration τ_σ in front of HCF (green).

duration τ_σ produces durations which are very different from the FWHM pulse durations τ. It is not a quantity well suited to describe a pulse shape which is dominated by a single peak, since little side peaks which are distant from the central time $t = 0$ are considered in undue strength and increase the pulse duration immensely despite their low physical importance. However, the combination of τ and τ_σ allows to make interesting conclusions about the temporal pulse shape. If τ is low and τ_σ is high, there is a short single peak, but a notable part of the total pulse energy is lost in small side peaks. If τ is high and τ_σ is low, the pulse energy is concentrated around $t = 0$, but in a disadvantageous broad peak or maybe even a double peak. If both τ and τ_σ are low the pulse shape is ideal for a single short peak with maximum energy.

The right-hand side of Fig. 4.10 demonstrates that τ_σ provides a much more intuitive description of the pulse in front of the hollow-core fiber than the FWHM duration τ. The standard deviation pulse duration τ_σ is at its minimum when the pulse is as close to being bandwidth-limited as is possible with its spectral phase $\phi(\omega)$. Around this minimum τ_σ increases symmetrically and continuously with variation of the spectral phase. In Fig. 4.10 that minimum of τ_σ is achieved when the spectral phase is modified by an additional $-160\,\mathrm{fs}^2$ GDD and $+10\,000\,\mathrm{fs}^3$ TOD in front of the hollow-core fiber.

It is an interesting observation that in the simulation the shortest FWHM FTL duration τ_0 after the hollow-core fiber is achieved with an input spectral phase with another $+10\,000\,\mathrm{fs}^3$ TOD. Fig. 4.11 illustrates the temporal pulse shape of three different pulses in front of the hollow-core fiber. The original pulse with the spectral amplitude and phase of our experiment (black), the pulse which according to the

simulation provides the shortest possible FWHM FTL pulse duration τ_0 after the hollow-core fiber and which exhibits a steep trailing edge (red), and the pulse which has the shortest standard deviation duration τ_σ in front of the fiber and which has the most symmetrical of the three pulse forms (green). The starting slope of all three pulses is similar, while the trailing edge has different gradients for each pulse. This demonstrates once more that not a smooth input spectral phase results in the shortest pulse duration possible after the fiber, but a spectral phase with a surplus of TOD and hence a pulse with a steep trailing edge.

4.3.3. Consideration of the chirped mirror compressor

An optimization of the Fourier-transform limited pulse duration τ_0 provides important information about the supercontinuum after the hollow-core fiber, but neglects to consider the restrictions imposed by the compressor which has to compensate for the dispersion of the laser pulse. It is demonstrated in Fig. 3.6 on page 66 that the mirrors from *FemtoLasers*, which are employed in our chirped mirror compressor (CMC), only work for frequencies from 2 PHz to roughly 3.1 PHz. The FTL pulse duration τ_0 is not a good quantity for optimization of the pulse if this causes a considerable part of the optimized supercontinuum to be outside of the spectral amplitude supported by the CMC.

The left-hand side of Fig. 4.12 illustrates what pulse durations τ are to be expected in the experiment if CMC and wedges are included in the simulation. The dispersion of the CMC is illustrated in Fig. 3.6, and the dispersion caused by propagation through air and fused silica elements in the beamline is also added to the simulation. The wedge position is handled as a degree of freedom and is optimized for each calculation to provide a short pulse duration after the CMC.

Actually, what is optimized with the wedges in the simulation is not the pulse duration but the peak power. The right-hand side of Fig. 4.12 shows how a pulse optimized with the wedges for pulse duration τ would look like in comparison to a pulse optimized for peak power. It is the same pulse after the fiber, but with slightly different settings of the wedges. The pulse optimized for pulse duration τ is slightly shorter, but it exhibits strong side peaks. This happens because with the wedges GDD and TOD are not optimized separately from each other, and an increase of GDD is also coupled with an increase of TOD. The same effect is observed in the actual experiment. Hence the slightly increased pulse duration of a pulse optimized for peak power is considered a trade-off for a notable increase in peak power and contrast.

The shortest pulse duration under these conditions is achieved with a modification of $-20\,\mathrm{fs}^2$ GDD and $+20\,000\,\mathrm{fs}^3$ TOD of the input spectral phase in front of the hollow-core fiber in the simulation. In comparison to Fig. 4.9 it is apparent that the general behaviour of the pulse duration after the hollow-core fiber under consideration of the compressor is similar to the behaviour of the FTL pulse duration, though with a shift of the input spectral phase to slightly higher values of GDD. For the shortest

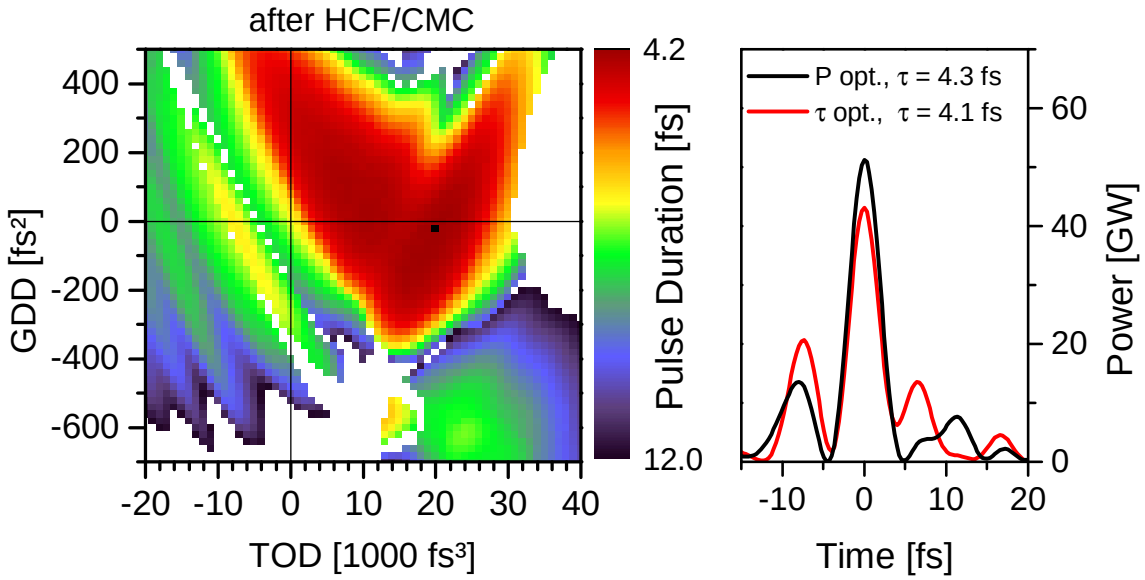

Figure 4.12.: Left-hand side: simulation of the pulse duration τ after propagation through HCF and CMC in dependence on GDD and TOD in front of HCF for a pulse with a spectral phase as in experiment (PrismComp0, Fig. 3.4). In white areas τ is beyond the scale. The input spectral phase resulting in the shortest pulse duration is marked with a black dot. The black lines mark the original input spectral phase without additional GDD or TOD. Right-hand side: simulated pulse with $-20\,\mathrm{fs}^2$ GDD and $+20\,000\,\mathrm{fs}^3$ TOD, with wedges optimized for peak power (in black) and for pulse duration τ (in red).
(Parameters: input spectral amplitude and phase as in experiment (Fig. 3.4, PrismComp0), $E = 830\,\mu\mathrm{J}$ per pulse, neon gas at $p = 1.8\,\mathrm{bar}$)

possible pulse duration this difference amounts to $+140\,\mathrm{fs}^2$ GDD.

4.4. Expectations for the experiment

It has been established in this chapter that it is possible to optimize the properties of the supercontinuum after a hollow-core fiber by manipulation of the input pulse's properties, and in particular its spectral phase $\phi(\omega)$. In the previous section it is demonstrated that for our experiment and its settings, including the typical input spectral phase provided by the laser system and the properties of the chirped mirror compressor, a modification of $-20\,\mathrm{fs}^2$ GDD and $+20\,000\,\mathrm{fs}^3$ TOD of the input spectral phase in front of the fiber would be beneficial for the generation of short pulses.

Fig. 4.13 illustrates the expected changes to the supercontinuum after the hollow-core fiber and the properties of the compressed laser pulses. The depicted simulations have been performed for three different input pulses, the original pulse (in black), the original pulse with an additional -20 fs^2 GDD and $+20\,000\,\mathrm{fs}^3$ TOD (in green) in accord with the results of Fig. 4.12, and a Gaussian pulse with a spectral phase equal to zero and a Fourier-transfrom limited (FTL) duration $\tau_0 = 27\,\mathrm{fs}$ (in blue). In comparison, the original input pulse has a FTL pulse duration $\tau_0 = 21.5\,\mathrm{fs}$ and a pulse duration $\tau = 34.9\,\mathrm{fs}$, with the latter decreasing to $\tau = 24.8\,\mathrm{fs}$ with the modification of -20 fs^2 GDD and $+20\,000\,\mathrm{fs}^3$ TOD.

To keep the simulation inside parameters where the calculation is valid the gas pressure has been reduced to $p = 1.8\,\mathrm{bar}$ for the simulations depicted in Fig. 4.13 e) and f). In c) $p = 3\,\mathrm{bar}$ is used, since this is a common setting in the experiment. In d) the results for the same input pulse as in c) are displayed for $p = 1.8\,\mathrm{bar}$ instead, and as expected the bandwidth of the supercontinuum decreases with the gas pressure.

In Fig. 4.13 e) it is demonstrated that the modification of the input spectral phase with -20 fs^2 GDD and $+20\,000\,\mathrm{fs}^3$ TOD results in a supercontinuum with a FTL pulse duration τ_0 which is more than 1 fs shorter than for the simulation with the original settings, depicted in c). If the same gas pressure p is used in the simulations, to allow for a more objective comparison of the effect of the input spectral phase, the difference in τ_0 is even 3.5 fs. This is mostly achieved by a broadening of the high frequency sidewing in the spectral amplitude. Furthermore the number of oscillations in the central part of the spectrum has been reduced and instead a single peak with more than twice the amplitude as before has evolved.

In Fig. 4.13 f) the results for a Gaussian input pulse with a flat or rather linear spectral phase are illustrated. The FTL pulse duration τ_0 is comparable with the results in e) for a Gaussian input pulse with the chosen bandwidth, but both the spectral amplitude and the group delay are much smoother than in c) or e). The smooth group delay means that this pulse is easier to compress, and a consequence of the smooth spectral amplitude is that the SPIDER will have less problems to retrieve the spectral phase.

In Fig. 4.13 g) the pulse shape after compression in the chirped mirror compressor

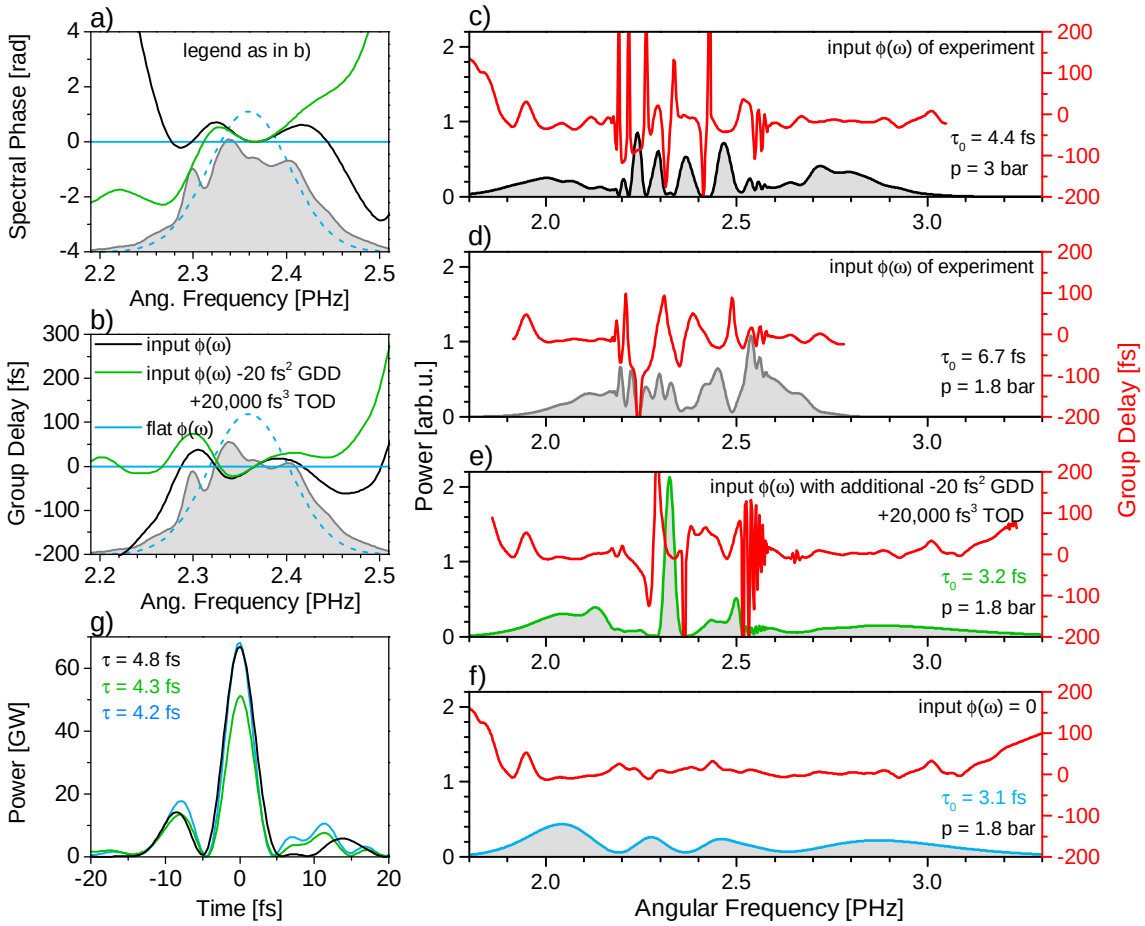

Figure 4.13.: Simulation results of the spectral amplitude, group delay and pulse duration τ after CMC for three different input pulses. In a) the spectral phase $\phi(\omega)$ and the spectral amplitude of the three input pulses are shown, with the original $\phi(\omega)$ of the experiment (see Fig. 3.4, PrismComp0) in black, the original $\phi(\omega)$ with an additional -20 fs^2 GDD and +20 000 fs^3 TOD in green, and a flat $\phi(\omega)$ in blue. The first two curves belong to the input spectral amplitude of the experiment, which is underlayed with grey, while the third curve has an input Gaussian pulse with $\tau_0 = 27$ fs, which is marked with a blue dashed line. In b) the respective group delay is shown. In c) to f) the resulting spectral amplitudes for these input pulses are shown at different gas pressures p. In g) the expected pulse shape and FWHM pulse duration τ after compression with the CMC and optimization with wedges are shown, belonging to the plots of c), e) and f) respectively.
(Parameters: $E = 830\,\mu$J per pulse, HCF length $z = 1$ m, bore radius $a = 125\,\mu$m, neon gas)

and optimized wedges is illustrated for the three chosen input pulses. It has to be pointed out though that the simulated pulse duration is about 0.5 fs shorter than the pulse duration measured with the SPIDER in the experiment, see Fig. 3.5 on page 64. Hence the pulse durations given by the simulation should rather be considered in comparison to each other than as absolute values. The pulse duration τ for the pulse with the modified input spectral phase at a gas pressure $p = 1.8$ bar is about 0.5 fs shorter than for the original pulse at $p = 3$ bar. However, the spectrum has become very broad, as is observable in plot e), and the chirped mirror compressor is not able to handle it as well as the spectrum in plot c). As a result laser power is transferred from the main peak to side peaks of the pulse and the peak power decreases about 23%, which is a disadvantage in nonlinear applications like high harmonic generation. This is an effect which is not included in the results of Fig. 4.12.

For example, a modification of the input spectral phase with $+10\,000\,\mathrm{fs}^3$ TOD instead of -20 fs^2 GDD and $+20\,000\,\mathrm{fs}^3$ TOD results in a pulse with a 0.1 fs longer duration τ, but only 7% loss of peak power instead of 23%.

An even better pulse after the hollow-core fiber is provided by an input pulse with a linear spectral phase, as is illustrated in Fig. 4.13 g). It has the shortest achievable pulse duration of the depicted pulses and even shows a slight increase of peak power. This would require the elimination of the double peak observed in the input spectral phase though.

At a wavelength of 800 nm a dispersion of $+10\,000\,\mathrm{fs}^3$ corresponds to the amount of TOD introduced by 36 cm fused silica or 10 cm SF10 Schott glass. Insertion of such a slab of material would increase the GDD for an even higher amount though and stretch the pulse to over 1 ps duration. Instead compressor schemes will have to be calculated to estimate how a high amount of TOD is introduced best to modify the input spectral phase.

Actually a pair of chirped mirrors with this purpose is already part of the stretcher in the CPA laser amplifier which is described in section 2.1.1. These chirped mirrors induce a not specified amount of negative GDD and positive TOD to compensate for negative TOD introduced in the amplifier, so that the pulses can be compressed as short as possible in the prism compressor which is part of the amplifier. Such a setup can be used to even further increase the amount of positive TOD, either by adding an additional pair of mirrors or by increasing the number of reflections on those present.

Chirped mirror compressors as these have been used in conjunction with the prism compressor of the CPA amplifier in successful beam lines. This hybrid compressor is meant to prevent the laser pulses from reaching their shortest duration inside one of the prisms of the prism compressor, which could otherwise cause self-phase modulation (SPM) in the prism [79, p. 36-37]. While SPM is utilized in the hollow-core fiber to increase the spectral bandwidth of the laser pulses, for pulses with negative GDD like in the prism compressor SPM has the opposite effect and decreases the pulses' bandwidth. This effect is explained in section 4.2.1. Because of that it

is desirable to prevent the onset of SPM in the prism compressor. Not to mention the possibility raised in section 3.2 that SPM in the prism compressor might be responsible for generating the disadvantageous double peak in the spectral phase in front of the hollow-core fiber. It has to be noted that the new generation of CPA amplifiers from *FemtoLasers* avoids the issues coming with a prism compressor by replacing it with a transmission grating compressor.

Barring a replacement of the prism compressor with an expensive grating compressor, a chirped mirror setup meant to introduce additional TOD for pulse optimization can also double as part of a hybrid compressor to prevent SPM in the amplifier and would hence be especially useful.

Even more attractive than a modification of the input spectral phase would be the achievement of a linear spectral phase. For this it is necessary to identify and if possible neutralize the cause of the double peak observable in the input spectral phase as illustrated in Fig. 3.4.

One possible source of this double peak is SPM occuring in the last prism of the prism compressor which is part of the CPA laser amplifier. While the beam has a large cross section in the last prism, the pulse duration is already so small that an onset of nonlinear processes in the glass is conceivable.

Another possible culprit is the SHG crystal which is part of the *FemtoSource Rainbow* oscillator from *FemtoLasers*. It is used to double the frequency of a part of the laser pulses to allow to monitor the spectral phase of each pulse with an f-to-2f interferometer. While the energy per pulse is low after the oscillator, the pulses have an ultrashort duration and are focused into the crystal, and hence the intensity might be sufficient to cause nonlinear effects beyond second harmonic generation.

It follows that it is necessary to measure the spectral phase at different locations in the system of laser oscillator and CPA amplifier to identify the source of the double peak in the spectral phase. Once it is found, it might be feasible to take steps to eliminate or decrease these double peaks and to provide a smooth spectral phase for the experiment.

This section demonstrates that the numerical simulation is a valuable tool to estimate how the laser pulse in front of the fiber can be modified to optimize the supercontinuum after the fiber, even if the proof for the validity of the results has to be provided by the experiment yet. However, it has been shown in chapter 3 that the results of the numerical simulations are in qualitative agreement with the results of the experiment. This opens the possibility to optimize the properties of the supercontinuum and to tailor it to specific applications by manipulation of the input pulse in front of the hollow-core fiber.

5. Conclusion and Outlook

In the late 1990's the principles of supercontinuum generation have been extended to gas-filled hollow-core fibers to create ultrashort high power laser pulses in the few-cycle regime for high harmonic generation. Since then the application of the generated high harmonic radiation has seen fast develoment and today the dynamics of solid state electron transitions are probed with attosecond resolution. There have been only few publications concerned with the complex process of supercontinuum generation inside the gas-filled hollow-core fiber though. This thesis contributes to the study of this field and opens possibilities for further optimization of the generated supercontinuum and ultrashort laser pulses.

At the attosecond beamline of University Bielefeld state-of-the-art experiments to resolve electron dynamics inside single crystal and layered crystal targets are performed, driven by single EUV light pulses of ca. 300 as duration. The generation of these isolated attosecond pulses is of crucial importance for the results of the experiment. To this end high harmonics are generated in a gas target with incident few-cycle infrared laser pulses of 5.3 fs duration and 50 GW peak power. Only with infrared laser pulses of this or shorter duration is it currently possible to isolate clean single attosecond pulses, and because of this the optimization of this pulse duration and the respective supercontinuum is an important procedure for a successful experiment.

The hollow-core fiber employed for the generation of the supercontinuum has a length of 1 m and an inner diameter of 250 µm, and is filled with neon gas at constant pressure up to 3 bar. The input laser pulses in front of the fiber are centered at a wavelength of 800 nm and have a pulse duration about 30 fs and an energy of ca. 830 µJ per pulse. To reproduce and explain the experimental results with numerical calculations a 1-dimensional model for pulse propagation in a fiber has been adapted to these parameters and is shown to provide correct results.

Building on that, the simulation is used to explain the experimental results and to make predictions about how to optimize the generated supercontinuum in this work. It is found that the spectral phase $\phi(\omega)$ of the input laser pulse in front of the fiber is a crucial parameter to control and optimize the properties of the supercontinuum after the fiber.

In experiments at the beamline the spectrum of the supercontinuum has been measured in dependence on the gas pressure in the hollow-core fiber and is found to be in qualitative agreement with the results of the numerical simulation. This is in particular true for the spectral amplitude. The agreement of the spectral phase

is less distinct, and currently it cannot be determined whether this is because of a physical effect or due to a limitation of the SPIDER to resolve fast changes of the spectral phase coupled with a low intensity of the spectral amplitude.

The pressure-dependent pseudocolor plots of the spectral amplitude after the hollow-core fiber are found to contain useful information about the input spectral phase of the laser pulses in front of the fiber. This allows to make educated guesses about the input spectral phase even without application of a phase-measuring instrument like a SPIDER.

The central result of the numerical calculations presented in this thesis is that characteristic features of the supercontinuum spectrum, like its bandwidth and the rapid oscillations of the central peaks, are identified as originating from properties of the input laser pulse in front of the hollow-core fiber, and in particular its spectral phase. This opens the possibility to control and optimize the supercontinuum by manipulation of the input spectral phase in front of the fiber.

Since the duration of the pulses after the hollow-core fiber is the most important characteristic of the supercontinuum for our experiment, simulations are used to optimize this quantity. It is found that even nearly bandwidth-limited input pulses provide shorter pulses after the fiber if the input spectral phase is modified with positive third order dispersion (TOD). The reason for this is the interplay between the pulse shape and self-steepening during propagation through the hollow-core fiber.

In a more practical application it is investigated whether a laser pulse as employed in the experiment, with a double peak in its spectral phase, can be optimized by simple manipulations of the spectral phase. It is found that a considerable amount of positive TOD in front of the fiber, in the form of $+20\,000\,\mathrm{fs}^3$, is likely to enhance the performance of the experiment and to significantly reduce the duration of the pulse after the hollow-core fiber. Considering the limitations of the chirped mirror compressor, the simulation estimates a reduction of the FHWM pulse duration about $0.5\,\mathrm{fs}$ for our experiment.

The simulation predicts that a similar reduction of the pulse duration would be achieved by a flat or linear input spectral phase, accompanied by other advantageous characteristics like an increased peak power and a smoother output spectral amplitude and phase. This would require to identify and eliminate the source of the double peak present in the spectral phase though, which might be caused by a flaw in the principle laser setup. This is a possibility meritting further investigation.

It might also be worthwhile to extend the simulation to a 3-dimensional model instead of the simpler 1-dimensional model employed in this thesis. The generated supercontinuum has proven to be highly sensible to changes of the alignment of the hollow-core fiber. It might be viable to investigate and illuminate this process with a simulation including all spatial directions.

The ability to optimize the properties of a supercontinuum by control of the spectral phase of the laser pulse in front of a hollow-core fiber, be it to increase the

bandwidth of the supercontinuum and decrease the pulse duration or to change the form of the oscillating peaks in the spectrum, is a powerful and important tool in any experiment concerning itself with ultrashort light pulses. It is demonstrated in this thesis that simple changes of the input spectral phase offer the possibility to optimize and improve the supercontinuum after the fiber and can be of great benefit for the experiment.

In the next step it has to be investigated experimentally whether the manipulation of the spectral phase in front of the fiber achieves the results in the supercontinuum predicted by the numerical calculations. Beyond that it is conceivable to expand the simulation with the employment of a genetic algorithm, to tailor the input spectral phase to specific desirable properties of the supercontinuum and utilize this optimization method for manifold purposes.

A. Data Archiving

The numerical simulation and other software tools written for this work have been programmed in LabVIEW 8.6. They can be found in the
nanooptik/DataArchive/Bartz_Peter_PhDThesis_2014
directory of the Faculty of Physics server of University Bielefeld.

The experimental and simulated data belonging to each figure of this thesis are also saved in that directory.

Bibliography

[1] Krausz, F. and M. Ivanov: *Attosecond physics.* Reviews of Modern Physics, 81:163, 2009.

[2] Dudley, J. M., G. Genty and S. Coen: *Supercontinuum generation in photonic crystal fiber.* Reviews of Modern Physics, 78:1135, 2006.

[3] Jones, D. J., S. A. Diddams, J. K. Ranka, A. Stentz, R. S. Windeler, J. L. Hall and S. T. Cundiff: *Carrier-Envelope Phase Control of Femtosecond Mode-Locked Lasers and Direct Optical Frequency Synthesis.* Science, 288:635, 2000.

[4] Alfano, R. R. and S. L. Shapiro: *Emission in the region 4000 to 7000 Å via four-photon coupling in glass.* Physical Review Letters, 24:584, 1970.

[5] Lin, C. and R. H. Stolen: *New nanosecond continuum for excited-state spectroscopy.* Applied Physics Letters, 28:216, 1976.

[6] Mollenauer, L. F., R. H. Stolen and J. P. Gordon: *Experimental Observation of Picosecond Pulse Narrowing and Solitons in Optical Fibers.* Physical Review Letters, 45:1095, 1980.

[7] Knight, J. C., T. A. Birks, P. St. J. Russel and D. M. Atkin: *All-silica single-mode optical fiber with photonic crystal cladding.* Optics Letters, 21:1547, 1996.

[8] Nisoli, M., S. De Silvestri and O. Svelto: *Generation of high energy 10 fs pulses by a new pulse compression technique.* Applied Physics Letters, 68:2793, 1996.

[9] Nisoli, M., S. De Silvestri, O. Svelto, R. Szipöcs, K. Ferencz, C. Spielmann, S. Sartania and F. Krausz: *Compression of high-energy laser pulses below 5 fs.* Optics Letters, 22:522, 1997.

[10] Hentschel, M., R. Kienberger, C Spielmann, G. A. Reider, N. Milosevic, T. Brabec, P. Corkum, U. Heinzmann, M. Drescher and F. Krausz: *Attosecond metrology.* Nature, 414:509, 2001.

[11] Kienberger, R., E. Goulielmakis, M. Uiberacker, A. Baltuska, V. Yakovlev, F. Bammer, A. Scrinzi, T. Westerwalbesloh,

U. Kleineberg, U. Heinzmann, M. Drescher and F. Krausz: *Atomic transient recorder.* Nature, 427:817, 2004.

[12] Cavalieri, A. L., N. Müller, T. Uphues, V. S. Yakovlev, A. Baltuska, B. Horvath, B. Schmidt, L. Blümel, R. Holzwarth, S. Hendel, M. Drescher, U. Kleineberg, P. M. Echenique, R. Kienberger, F. Krausz and U. Heinzmann: *Attosecond spectroscopy in condensed matter.* Nature, 449:1029, 2007.

[13] Neppl, S., R. Ernstorfer, E. M. Bothschafter, A. L. Cavalieri, D. Menzel, J. V. Barth, F. Krausz, R. Kienberger and P. Feulner: *Attosecond Time-Resolved Photoemission from Core and Valence States of Magnesium.* Physical Review Letters, 109:87401, 2012.

[14] Zheltikov, A. M.: *Ultrashort light pulses in hollow waveguides.* Physics Uspekhi, 45:687, 2002.

[15] Suda, A., Hatayama M., Nagasaka K. and K. Midorkawa: *Generation of sub-10-fs, 5-mJ-optical pulses using a hollow fiber with a pressure gradient.* Applied Physics Letters, 86:111116, 2005.

[16] Vozzi, C., M. Nisoli, G. Sansone, S. Stagira and S. De Silvestri: *Optimal spectral broadening in hollow-fiber compressor systems.* Applied Physics B, 80:285, 2005.

[17] Wollenhaupt, M., A. Assion and T. Baumert: *Springer Handbook of Lasers and Optics, Chapter 12: Short and Ultrashort Laser Pulses.* Springer, 2012.

[18] Diels, J.-C. and W. Rudolph: *Ultrashort Laser Pulse Phenomena.* Academic Press, 2006.

[19] Wrzesinski, P. J., D. Pestov, V. V. Lozovoy, J. R. Gord, M. Dantus and S. Roy: *Group-velocity-dispersion measurements of atmospheric and combustion-related gases using an ultrabroadband-laser source.* Optics Express, 19:5163, 2011.

[20] Malitson, I. H.: *Interspecimen Comparison of the Refractive Index of Fused Silica.* Journal of the Optical Society of America, 55:1205, 1965.

[21] Bideau-Mehu, A., Y. Guern, R. Abjean and A. Johannin-Gilles: *Measurement of refractive indices of neon, argon, krypton and xenon in the 253.7-140.4 nm wavelength range. Dispersion relations and estimated oscillator strengths of the resonance lines.* Journal of Quantitative Spectroscopy and Radiative Transfer, 25:395, 1981.

[22] Agrawal, G. P.: *Nonlinear Fiber Optics.* Academic Press, 2007.

[23] Kasparian, J., P. Béjot and J.-P. Wolf: *Arbitrary-order nonlinear contribution to self-steepening.* Optics Letters, 35:2795, 2010.

[24] Weiner, A. M.: *Ultrafast Optics.* Wiley, 2009.

[25] Buckingham, A. D. and J. A. Pople: *Theoretical Studies of the Kerr Effect I: Deviations from a Linear Polarization Law.* Proceedings of the Physical Society. Section A, 68:905, 1955.

[26] Brinkmann, M., J. Hayden, M. Letz, S. Reichel, C. Click, W. Mannstadt, B. Schreder, S. Wolff, S. Ritter, M. J. Davis, T. E. Bauer, H. Ren, Y.-H. Fan, Y. Menke, S.-T. Wu, K. Bonrad, E. Krätzig, K. Buse and R. A. Paquin: *Springer Handbook of Lasers and Optics, Chapter 5: Optical Materials and Their Properties.* Springer, 2012.

[27] Kibler, B., J. M. Dudley and S. Coen: *Supercontinuum generation and nonlinear pulse propagation in photonic crystal fiber: influence of the frequency-dependent effective mode area.* Applied Physics B, 81:337, 2005.

[28] Born, M. and E. Wolf: *Principles of Optics.* Pergamon Press, 1986.

[29] Karasawa, N., S. Nakamura, N. Nakagawa, M. Shibata, R. Morita, H. Shigekawa and M. Yamashita: *Comparison Between Theory and Experiment of Nonlinear Propagation for A-Few-Cycle and Ultrabroadband Optical Pulses in a Fused-Silica Fiber.* IEEE Journal of Quantum Electronics, 37:398, 2001.

[30] Nurhuda, M., A. Suda, K. Midorkawa, Hatayama M. and Nagasaka K.: *Propagation dynamics of femtosecond laser pulses in a hollow fiber filled with argon: constant gas pressure versus differential gas pressure.* Journal Optical Society of America B, 20:2002, 2003.

[31] Tempea, G. and T. Brabec: *Theory of self-focusing in a hollow waveguide.* Optics Letters, 23:762, 1998.

[32] Bree, C., A. Demircan and G. Steinmeyer: *Method for Computing the Nonlinear Refractive Index via Keldysh Theory.* IEEE Journal of Quantum Electronics, 46:433, 2010.

[33] Brabec, T. and F. Krausz: *Nonlinear Optical Pulse Propagation in the Single-Cycle Regime.* Physical Review Letters, 78:3282, 1997.

[34] Bradford, S. C.: *Time-Frequency Analysis of Systems with Changing Dynamic Properties.* PhD thesis, California Institute of Technology, 2006.

[35] Akturk, S., A. Couairon, M. Franco and A. Mysyrowicz: *Spectrogram representation of pulse self compression by filamentation.* Optics Express, 16:17626, 2008.

[36] Wigner, E.: *On the Quantum Correction For Thermodynamic Equilibrium.* Physical Review, 40:749, 1932.

[37] Ville, J.: *Théorie et Applications de la Notion de Signal Analytique.* Câbles et Transmission, 2:61, 1948.

[38] Boashash, B.: *Estimating and Interpreting The Instantaneous Frequency of a Signal-Part 1: Fundamentals.* Proceedings of the IEEE, 80:520, 1992.

[39] Azana, J.: *Time-Frequency (Wigner) Analysis of Linear and Nonlinear Pulse Propagation in Optical Fibers.* EURASIP Journal on Applied Signal Processing, 10:1554, 2005.

[40] Spielmann, C, N. H. Burnett, S. Sartania, R. Koppitsch, M. Schnürer, C. Kan, M. Lenzner, P. Wobrauscheck and F. Krausz: *Generation of Coherent X-rays in the Water Window Using 5-Femtosecond Laser Pulses.* Science, 278:661, 1997.

[41] Sansone, G., L. Poletto and M. Nisoli: *High-energy attosecond light sources.* Nature Photonics, 5:655, 2011.

[42] Neb, S.: *Attosekunden-Streaking-Experimente an Neon.* Master's thesis, Universität Bielefeld, 2013.

[43] Sander, C.: *Untersuchung von Phaseneffekten von höherer harmonischer Strahlung zur Erzeugung von Attosekundenpulsen für Streakingexperimente.* Master's thesis, Universität Bielefeld, 2012.

[44] Robinson, J. S., C. A. Haworth, H. Teng, R. A. Smith, J. P. Marangos and J. W. G. Tisch: *The generation of intense, transform-limited laser pulses with tunable duration from 6 to 30 fs in a differentially pumped hollow fibre.* Applied Physics B, 85:525, 2006.

[45] Cao, S., W. Kong, Z. Song, Y. Qin, R. Li, Q. Wang and Z. Zhang: *Temperature Controlled Filamentation in Argon Gas.* Chinese Physical Letters, 25:3689, 2008.

[46] Béjot, P., B. E. Schmidt, J. Kasparian, J.-P. Wolf and F. Legaré: *Mechanism of hollow-core-fiber infrared-supercontinuum compression with bulk material.* Physical Review A, 81:63828, 2010.

[47] Marschewski, E.: *Weißlichterzeugung in einer gasgefüllten Hohlfaser.* Master's thesis, Universität Bielefeld, 2012.

[48] Iaconis, C. and I. A. Walmsley: *Spectral phase interferometry for direct electric-field reconstruction of ultrashort optical pulses.* Optics Letters, 23:792, 1998.

[49] Takeda, M., H. Ina and S. Kobayashi: *Fourier-transform method of fringe-pattern analysis for computer-based topography and interferometry.* Journal of the Optical Society of America, 72:156, 1982.

[50] Iaconis, C. and I. A. Walmsley: *Self-Referencing Spectral Interferometry for Measuring Ultrashort Optical Pulses.* IEEE Journal of Quantum Electronics, 35:501, 1999.

[51] Gilles, L., S. C. Hagness and L. Vazquez: *Comparison between Staggered and Unstaggered Finite-Difference Time-Domain Grids for Few-Cycle Temporal Optical Soliton Propagation.* Journal of Computational Physics, 161:379, 2000.

[52] Kinsler, P.: *Pulse propagation methods in nonlinear optics (2013).* arXiv:0707.0982, http://arxiv.org/abs/0707.0982v4.

[53] Kodama, Y. and A. Hasegawa: *Nonlinear Pulse Propagation in a Monomode Dielectric Guide.* IEEE Journal of Quantum Electronics, QE-23:510, 1987.

[54] Blow, K. J. and D. Wood: *Theoretical Description of Transient Stimulated Raman Scattering in Optical Fibers.* IEEE Journal of Quantum Electronics, 25:2665, 1989.

[55] Boyer, G.: *High-power femtosecond-pulse reshaping near the zero-dispersion wavelength of an optical fiber.* Optics Letters, 24:945, 1999.

[56] Homoelle, D. and L. Gaeta: *Nonlinear propagation dynamics of an ultrashort pulse in a hollow waveguide.* Optics Letters, 25:761, 2000.

[57] Genty, G., P. Kinsler, B. Kibler and J. M. Dudley: *Nonlinear envelope equation modeling of sub-cycle dynamics and harmonic generation in nonlinear waveguides.* Optics Express, 15:5382, 2007.

[58] Song, Z., G. Zhang, S. Cao, D. Pang, L. Chai, Q. Wang and Z. Zhang: *Simulation of Femtosecond Pulse Propagation through Hollow Fibre Filled with Noble Gases of Gradient Temperature.* Chinese Physical Letters, 25:129, 2008.

[59] Marcatili, E. A. J. and R. A. Schmeltzer: *Hollow Metallic and Dielectric Waveguides for Long Distance Optical Transmissions and Lasers.* Bell System Technical Journal, 43:1783, 1964.

[60] Nubling, R. K. and J. A. Harrington: *Launch conditions and mode coupling in hollowglass waveguides.* Optical Engineering, 37:2454, 1998.

[61] Brabec, T. and F. Krausz: *Intense few-cycle laser fields: Frontiers of nonlinear optics.* Review of Modern Physics, 72:545, 2000.

[62] Loriot, V., E. Hertz, O. Faucher and B. Lavorel: *Measurement of high order Kerr refractive index of major air components.* Optics Express, 17:13429, 2009.

[63] Whalen, P., J. V. Moloney, A. C. Newell, K. Newell and M. Kolesik: *Optical shock and blow-up of ultrashort pulses in transparent media.* Physical Review A, 86:33806, 2012.

[64] Mlejnek, M., E. M. Wright and J. V. Moloney: *Femtosecond pulse propagation in argon: A pressure dependence study.* Physical Review E, 58:4903, 1998.

[65] Anderson, D. and M. Lisak: *Nonlinear asymmetric self-phase modulation and self-steepening of pulses in long optical waveguides.* Physical Review A, 27:1393, 1983.

[66] Aközbek, N., C. M. Bowden, A. Talebpour and S. L. Chin: *Femtosecond pulse propagation in air: Variational analysis.* Physical Review E, 61:4540, 2000.

[67] Merschjohann, Fabian: *intended and not yet existing.* PhD thesis, Universität Bielefeld.

[68] Wonisch, A., U. Neuhäusler, N. M. Kabachnik, T. Uphues, M. Uiberacker, V. Yakovlev, F. Krausz, M. Drescher, U. Kleineberg and U. Heinzmann: *Design, fabrication, and analysis of chirped multilayer mirrors for reflection of extreme-ultraviolet attosecond pulses.* Applied Optics, 45:4147, 2006.

[69] Thompson, A. C. (editor): *X-Ray Data Booklet.* Lawrence Berkeley National Laboratory, 2009.

[70] Nisoli, M., S. Stagira, S. De Silvestri, O. Svelto, S. Sartania, Z. Cheng, M. Lenzner, C Spielmann and F. Krausz: *A novel high energy pulse compression system: generation of multigigawatt sub-5-fs pulses.* Applied Physics B, 65:189, 1997.

[71] Frank, F., C. Arrell, C. Witting, W. A. Okell, J. McKenn, J. S. Robinson, C. A. Haworth, D. Austin, H. Teng, I. A. Walmsley, J. P. Marangos and J. W. G. Tisch: *Invited Review Article: Technology for Attosecond Science.* Review of Scientific Instruments, 83:71101, 2012.

[72] Gallmann, L., T. Pfeifer, P. M. Nagel, M. J. Abel, D. M. Neumark and S. R. Leone: *Comparison of the filamentation and the hollow-core fiber*

characteristics for pulse compression into the few-cycle regime. Applied Physics B, 86:561, 2007.

[73] Planas, S. A., N. L. Pires Mansur, C. H. Brito Cruz and H. L. Fragnito: *Spectral narrowing in the propagation of chirped pulses in single-mode fibers.* Optics Letters, 18:699, 1993.

[74] Winterfeldt, C., C Spielmann and G. Gerber: *Colloquium: Optimal control of high-harmonic generation.* Reviews of Modern Physics, 80:117, 2008.

[75] Kornelis, W., M. Bruck, F. W. Helbing, C. P. Hauri, A. Heinrich, J. Biegert and U. Keller: *Single-shot dynamics of pulses from a gas-filled hollow fiber.* Applied Physics B, 79:1033, 2004.

[76] Liao, Z. M., C. J. McKinstrie and G. P. Agrawal: *Importance of prechirping in constant-dispersion fiber links with a large amplifier spacing.* Journal Optical Society of America B, 17:514, 2000.

[77] Hauri, C. P., A. Guandalini, P. Eckle, W. Kornelis, J. Biegert and U. Keller: *Generation of intense few-cycle laser pulses through filamentation - parameter dependence.* Optics Express, 19:7541, 2005.

[78] Varela, O., B. Alonso, I. J. Sola, J. San Roman, A. Zair, C. Mendez and L. Roso: *Self-compression controlled by the chirp of the input pulse.* Optics Letters, 35:3649, 2010.

[79] Horvath, B.: *Generation, characterization and sub-cycle shaping of intense, few-cycle light waveforms for attosecond spectroscopy.* PhD thesis, Ludwig-Maximilians-Universität München, 2009.

Acknowledgements

After my intermediate exams I was recruited as an assistant for laboratory work by Dr. Markus Drescher. Little did I know at the time that this friendly and likeable man is a pioneer in ultrashort pulse physics and that his field of study would become my own. He introduced me to his own chef, Prof. Dr. Ulrich Heinzmann, and I completed my diploma thesis in Prof. Dr. Heinzmann's group and took part in some very interesting femtosecond-resolved pump-probe studies of core-level reaction dynamics.

However, the best time in my career as a physicist yet started when I was assigned to help bring the attosecond beamline of University Bielefeld to operation. This was a joint venture of the groups of Prof. Dr. Heinzmann and Prof. Dr. Pfeiffer, and instead of charging a postdoc with experience in the field with the task, they trusted a small group of PhD and master students to manage it. And we did. Attosecond-resolved photoelectron spectroscopy is a very complex experiment and it feels like bugs have riddled every single aspect they could on the way. But we found them all and removed every source of error, misalignment and instability, and today the beamline and experiment are operating at peak level and provide state-of-the-art measurements.

The amount and breadth of things I learned about physics during this time is invaluable, and while at times frustrating, most often it was fun.

I owe Prof. Dr. DrSc. h.c. Ulrich Heinzmann an immense debt of gratitude to make this doctoral thesis at all possible. I thank Prof. Dr. Walter Pfeiffer for bringing his vast knowledge about ultrafast optics to bear in this project and for innumerable discussions and suggestions.

The PhD students Fabian Merschjohann and Sergej Neb have been my coworkers all this time and they made the long hours in the laboratory fun. We have been an excellent team!

Christian Strueber and Matthias Hensen, beside being always available for advice, tirelessly attended to the laser system. And cared for the laser system. And nursed the laser system. They worked wonders!

Finally I want to thank Christian Meier for kind help in all things computer-related, Dr. Norbert Mueller for sage advice, and Kay Lofthouse for ceaselessly caring for the whole work group.

Most of all and above everything I have to thank my wife Heike though. She kept our family afloat when I was buried in work, and it has not been easy.

Thank you.